Gold-coated silver nanowire-based Tip-Enhanced Raman Spectroscopy probe for long life and high enhancement

金コート銀ナノワイヤを用いた探針増強ラマン散乱プローブの開発

Han Wen

Graduate School of Information Science and Technology,

Hokkaido University

Supervisor: Hiroshi Uji-i

Table of Contents

Acknowledgments

This doctoral research was carried out under the guidance of professor Hiroshi Uji-i at Hokkaido University.

Firstly, I would like to express my greatest gratitude to my supervisor, professor Hiroshi Uji-i, for guiding me into the world of Nanomaterials and Nanoscopy and supporting me in academics. There is one saying from professor Hiroshi Uji-i which impressed me deeply: “Ph.D. changes life.” During the four-year Ph.D. period, professor Uji-i's rigorous attitude and meticulously logical thinking toward science has benefited me a lot. Besides, as to life attitudes, I tended to be negative when facing difficulties, falling into the whirlpool of depression, while Professor Uji-i taught me to think positively not only in academics but also in daily life. “Always thinking negatively doesn't solve anything”, says Professor Uji-i. In a word, thanks to professor Uji-i, I obtained not only innumerable academical skills but also a positive future.

Secondly, I would like to show my gratitude to associate professor Kenji Hirai and assistant professor Tomoko Inose for supporting me in my research and daily life. Thanks to their help, I improved many skills, such as academic writing and operating experimental instruments. Moreover, they helped me in my daily life, such as handling miscellaneous paperwork.

Also, I would like to show my gratitude to Yasuhiko Fujita-san for helping me with some measurements in my research and supporting me in handling technical hitches and manuscript writing. Besides, Thanks to Beatrice Fortuni-san and Shuichi Toyouchi-san for helping me to improve my manuscripts.

Moreover, I would like to thank my fellow labmates for supporting me during these tough years, amongst whom I would like to express special gratitude to Qiang Zhang, who gave me the biggest help both experimentally and mentally. To be honest, I may not be able to cross the tough period without his help.

Also, I would like to give my sincere gratitude to my best friends: Dr. Mudi Ma, Dr. Hanjun Zhao, Jiaxing Yu, Xiaohan Wang, Dr. Li Hao, Huang Chen, et al. We tided over the darkest hours, shared the high-light moments; we climbed over mountains, dived into the sea; we enjoyed delicacy and also tasted unpalatable meals; we went through howling wind and showering rain, also enjoyed the sea of flowers ebb and flow. Thanks to my friends, only with

them behind and supporting me can I persist on the way to the Ph.D. degree. People always say the deepest and purest friendship bonds in schooldays. I believe these precious friendships will last lifelong.

Furthermore, I would like to show my biggest gratitude to my family. I was born in a normal middle-class family, which was only sufficiently fed and clothed. Nevertheless, my mother, father, and grandparents supported me materially and mentally. They are my financial backing and the harbor of my soul. I know my family is not rich, but they never hesitate to send money when I need it. When I fell into depression, they comforted me just as they always did, giving me power. As ancient Chinese poetry says, where my heart gets peace, where my self gets home. To me, where my families are, is where my home is, and is where I can get peace. Thanks again to my family, not only for what they did during my Ph.D. but also for what they extended to my whole life, which I will also spend my whole life reciprocating.

Finally, I would like to express my gratitude to Hokkaido University for giving me the opportunity to study here. I also would like to express my gratitude to the Hokkaido University DX Doctoral Fellowship (2021) and HIECC scholarship (2020).

I would like to express my gratitude to all of the people who have ever helped me during these four years. Giving my sincere thanks again to everyone.

Abstract

Optical spectroscopic techniques are key analytical tools in a wide range of fields, shaping our essential understanding of many fundamental phenomena. Among these, Raman spectroscopy is one important technique. In Raman scattering, the change of the frequency of light is only related to the vibrational modes of the molecular electronic ground state. Thus, each molecule has a unique Raman spectrum, which makes the Raman spectrum the "molecular fingerprint", enabling Raman scattering to precisely analyze the structure of a molecule and interaction between them. Besides the specificity, the Raman scattering technique possesses the following advantages: non-invasive measurement, simple preparation of the sample (i.e., label free), the ability to simultaneously detect different analytes, and the applicability to biological samples and so on. However, the intensity of Raman scattering is inherently weak, and the spatial resolution is restricted by the diffraction limit, hindering its further applications.

To overcome these drawbacks, Surface-Enhanced Raman Scattering (SERS) technique has been developed, which dramatically enhances the intensity of Raman signal. However, the SERS technique requires nanoparticle aggregations or substrate surface to be roughened or deposited with nanostructures made of noble metals, such as Ag, Au, or Cu. SERS is enhanced at positions that randomly located on these substrates, which makes it difficult to locate the SERS active position (hotspot) relative to the sample of interest. The resulting relatively poor spatial resolution achieved with these substrates often becomes a limiting factor in practical applications. To overcome this limitation, an innovative technique called tip-enhanced Raman spectroscopy (TERS) emerged as the times require.

Tip-enhanced Raman spectroscopy (TERS) is the combination of Raman spectroscopy with scanning probe microscopy (SPM). By using the electromagnetic field enhancement resulting from the localized surface plasmon resonances (LSPRs) of silver or gold SPM tips, the Raman signal can be enhanced and localized to the area beneath the tip, which allows TERS to give correlated Raman and topographic images at a nanoscale resolution. In a TERS system, the SPM part could be the scanning tunneling microscope (STM), shear force microscopy (SFM), and atomic force microscope (AFM), among which the AFM-based TERS is more widely used as being more stable, faster, and having no intrinsic substrate limitations. However, the widely used AFM-TERS probes fabricated with metal deposition suffer from relatively low

reproductivity as well as their limited mapping and storage lifetime, which requires precise control over surface structure on the nanoscale.

Our research group previously developed the chemically synthesized silver nanowires (AgNW)-based AFM-TERS probe, which, thanks to the high homogeneity of the liquid-phase synthesis of AgNW, can achieve high TERS performance with excellent probe reproductivity, but still presenting short lifetime due to probe oxidation. Besides, this fabrication method still suffers from the low control of the protruded length of AgNW. This thesis thus focused on solving the durability, length control and enhancement.

On the first section, a simple Au coating method is proposed to overcome the limited lifetime and improve the performance of the AgNW-based TERS probe. For the Au-coating, different [Au]/[Ag] molar ratios were investigated. The TERS performance was evaluated in terms of change in enhancement factor (EF) and signal-to-noise ratio through multiple mappings and the storage lifetime in air. The Au-coated AgNWs exhibited higher EF than pristine AgNW and galvanic-replaced AgNW with no remarkable difference between the two molar ratios tested. However, for longer scanning time and multiple mappings, the probes obtained with low Au concentration showed much longer-term stability with keeping high EF. Furthermore, the Au-coated AgNW probes were found to possess a longer storage lifetime in air, allowing for long and multiple TERS mappings with one single probe.

On the second section, a simple water-air interface electro-cutting method is proposed to achieve wide controllability of the length. This water-cut method was combined with the succedent Au coating on AgNW surface after cutting, which enabled to obtain high durability, impressive enhancement factor (EF) and excellent spatial resolution. The TERS performance was evaluated in terms of change in EF through multiple mappings and spatial resolution. The water-cut Au-coated AgNWs, with appropriated Au concentration and pH, achieved up to 100 times higher EF and two times smaller spatial resolution than pristine AgNW. Thanks to this excellent EF, the water-cut Au-coated AgNW probes were found to possess high TERS activity even in non-gap mode, allowing for broader applications.

In summary, this work offers solution to the issues of the durability, length control of the AgNW-based AFM-TERS probe, and achieved high Raman enhancement even can conduct non-gap mode TERS measurement, which significantly broadens the application of TERS and provides some promising development directions of TERS technique.

Chapter 1 General Introduction

1.1 Introduction of the nanotechnology and nanomaterials

1.1.1 History of nanotechnology

Nanotechnology is the science and technology that studies the interaction and characteristics of materials in the nanoscale dimension (1 nm ~ 100 nm), which achieves the manipulation and manufacturing of products with specific functions at the atomic level.[1] After its theoretical foundation in the 1980s and rapid development in the 1990s, nanotechnology has become one of the major technologies promoting the development of human science and technology in the 21st century.[2]

In ancient times, people already started using nanotechnology without recognizing the concept. The Lycurgus cup, created by the Romans in the fourth century AD, is demonstrated to be one of the oldest synthetic nanomaterials in the ancient world.[3] It is the oldest famous example of dichroic glass, which changes color in certain lighting conditions: in direct light, the glass appears green while appears red-purple when light shines through the glass, shown in Fig. 1-1. In 1990, scientists analyzed the cup using transmission electron microscopy (TEM)[4] and X-ray. The observed dichroism is due to the presence of silver-gold (Ag: Au ~ 7:3, with ~10% Cu) alloy nanoparticles with 50–100 nm in diameter dispersed in a glass matrix.[5, 6] The green color is attributed to the light scattering by colloidal dispersions of Ag nanoparticles with a size smaller than 40 nm while the red-purple color is due to the absorption by the bigger (~50 nm) Au nanoparticles (~520 nm).

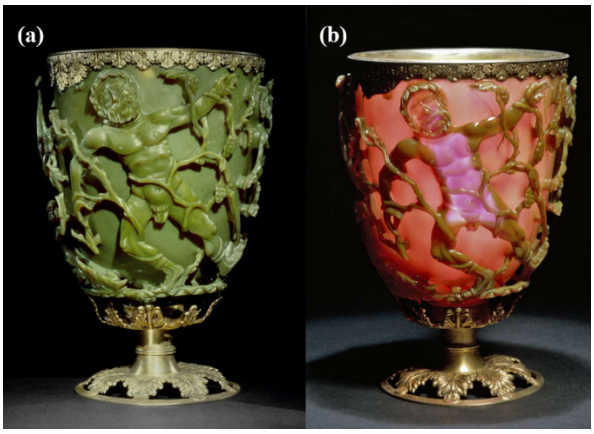

Figure 1-1. The Lycurgus cup in direct light (a) and in transmitted light (b). [adapted from[7]]

Back to the modern time, Michael Faraday describes the observation of nanoparticles through the wavelength-dependent scattering of light (later called Tyndall scattering) by chemically-produced gold colloids suspended in water in 1856.[8] In December 1959, renowned theoretical physicist and Nobel Laureate in Physics Richard Feynman proposed the concept of nanotechnology in his famous lecture "There's Plenty of Room at the Bottom": "At the atomic level, we have new kinds of forces and new kinds of possibilities, new kinds of effects. The problems of manufacture and reproduction of materials will be quite different." [9] In 1974, Japanese scientist Norio Taniguchi first began to use the term "Nanotechnology" to describe precision mechanical material processing.[10] In 1987, Kim Eric Drexler, a famous American scientist, predicted in his book that the future nanotechnology would use machines at the molecular scale to construct substances from the bottom up.[11] In July 1990, the first International Nanotechnology Conference was successfully held in the United States, which discussed and prospected the frontier fields and development trends of nanotechnology, following which three journals, namely Nanotechnology, Nanostructured Materials, and Nanobiology, were published. Since then, nanotechnology has entered a period of rapid development and has gradually become one of the critical technologies affecting the development of human science and technology.

Nanotechnology booms on the development of tools for observation, experimentation, and manipulation. In 1931, Ernst Ruska and Max Knoll demonstrated the first electron microscopy, shown in Fig. 1-2a.[12] In 1982, Gerd Binnig and Heinrich Rohrer et al. obtained the first single-atom step image by scanning the atomic structure of a sample surface with a metal tip, which heralded the birth of Scanning Tunneling Microscopy (STM) with atomic resolution.[13] In 1986, Gerd Binnig, Calvin F. Quate, and Ch. Gerber developed Atomic Force Microscopy (AFM).[14] Subsequently, Scanning Probe Microscopy (SPM), represented by AFM, developed progressively. SPM enables not only the study of the surface structural characteristics and mechanical properties, such as hardness and elasticity of various materials but also achieves selective surface modification of precise positioning definition patterns under specific conditions.[15] A famous example is the atom-by-atom manipulation implemented by Don Eigler and Erhard Schweizer using an STM to manipulate individual xenon atoms on a nickel surface to form the letters' IBM',[16] shown in Fig. 1-2b. Some scientific milestones of the tools for nanotechnology are introduced in Fig. 1-2c. Until now, these tools are still under continuous development and are widely applied, making nanotechnology increasingly important in fields

such as physics, chemistry, biology, medicine, materials, energy, environment, and microelectronics et al.

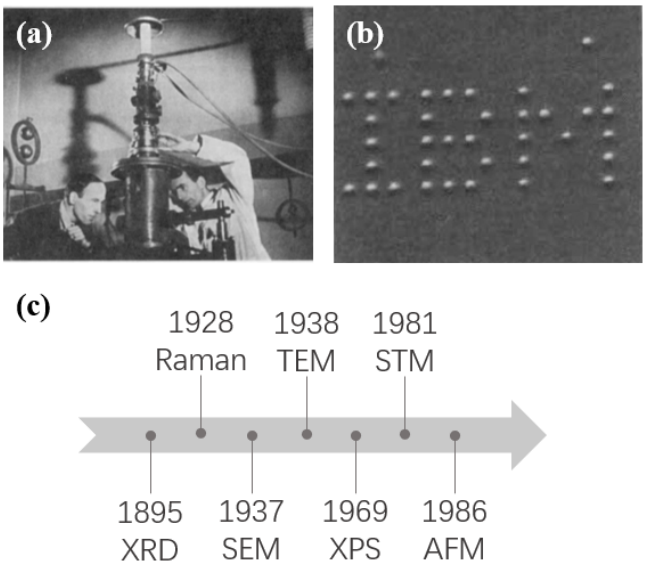

Figure 1-2. (a) The first electron microscope was carefully checked by Ernst Ruska (right), as Max Knoll (left) keenly observed in 1931 [adapted from[12]]; (b) Xenon atoms positioned on a nickel (110) substrate using a STM to form IBM logo [adapted from[16]]; (c) Some scientific milestones of the tools for nanotechnology [adapted from[17]].

1.1.2 Application of nanotechnology

Nanotechnology is a multidisciplinary system that is based on the scientific disciplines of mechanics, physics, chemistry, and biology and the engineering disciplines of medicine, materials, manufacturing, information, environment, energy, and microelectronics at the nanoscale. The nanotechnology system includes not only fundamental research aiming to observe phenomena and explore the mechanism but also technical research aiming to achieve nanostructure controlling, functional material processing, and related device creation. Therefore, nanotechnology is a comprehensive system integrating frontier science and high technology, which provides an excellent platform for interdisciplinary research.

Specifically, the applications of nanotechnology in some fields are introduced below.

Electronic information: The microelectronics industry has always had a strong need for nanotechnology. Moore's Law, introduced by Moore in 1965: states that the number of

transistors incorporated in a chip will approximately double every 24 months,[18] has continued to stimulate the development of the manufacturing process from 10 μm at the early stage to 7 nm by 2020, and 3 nm by 2022, shown as Fig. 1-3.[19] In addition, in the information storage field, nanotechnology can reduce the size of components, which allows the storage media to be arranged more densely, achieving higher storage efficiency.

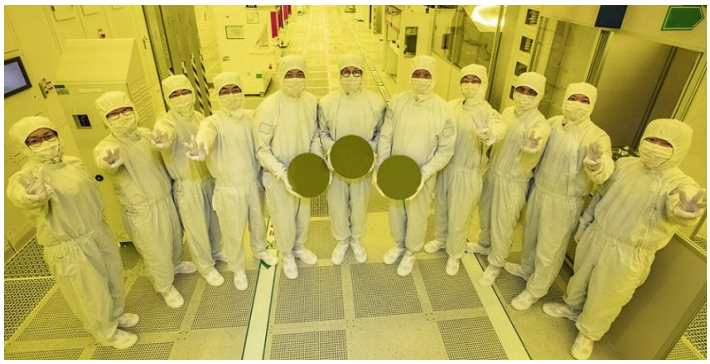

Figure 1-3. The leaders of Samsung Foundry Business and Semiconductor R&D Center celebrate the company's first-ever production of the 3 nm process with Gate-All-Around (GAA) architecture. [adapted from[19]]

Chemical Engineering: More efficient industrial catalysts have always been desired in the chemical industry. The size and morphology of catalysts significantly influence the catalytic performance. Nanomaterials possess a high specific surface area, leading to strong landing properties. Besides, some nanomaterials show porous structure, resulting in high absorption nature. Thus, nanomaterials act as good catalysts, active ingredients, and carriers.[20]

Medical drugs: nanomaterials have good permeability, so the active ingredients of some drugs can be loaded into nanomaterials through nanotechnology, and they can be accurately delivered to the nidus, which has a good therapeutic effect for some specific diseases. The DNA and protein of the human body are all nanoscales. Thus, understanding the pathogenic mechanism of diseases from the nanoscale is inseparable from the development of nanotechnology. For example, from current research, nanotherapy is a promising approach to cancer treatment.[21] Also, during the COVID-19 outbreak in early 2020, Chinese researchers resolved the 3D structure of the complex of S protein receptor binding domain on the surface of the virus and ACE2 protein, showing a receptor on the surface of human cells at the fastest speed, so that everyone could "see" the moment when the novel coronavirus infected the human body, shown

in Fig. 1-4.[22, 23] It provides great help for the follow-up research and development of effective drugs and the research of transmission mechanism.

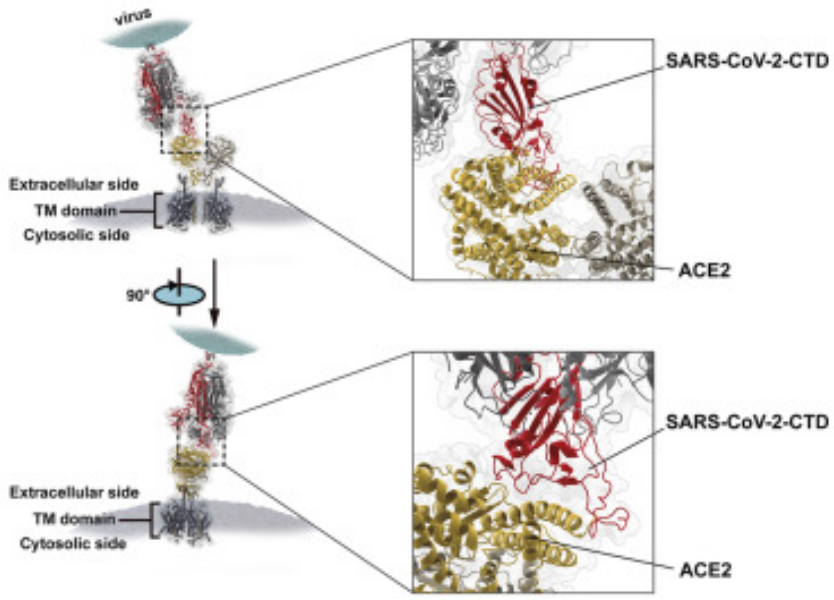

Figure 1-4. The crystal structure of the C-terminal domain of SARS-CoV-2 (SARS-CoV-2-CTD) spike (S) protein in complex with human ACE2 (hACE2) receptor. [adapted from[23]]

Energy and environment: The application of nano-engineering in the photovoltaic material study can improve the power generation performance of photovoltaic equipment and reduce the cost of solar power generation.[24] For waste heat conversion, nanomaterials can convert the energy contained in the exhaust into useful energy.[25] Nanostructured electrode materials improve the capacity and performance of rechargeable batteries.[26] Some of the electrode materials are shown in Fig. 1-5. Based on the unique physical and chemical properties of nanomaterials, nanotechnology can be applied to identify toxic levels and pollution treatment in the environment.[27] Generally, the applications of nanotechnology in water and air pollution treatment are summarized in Fig. 1-6 and Fig. 1-7, respectively.

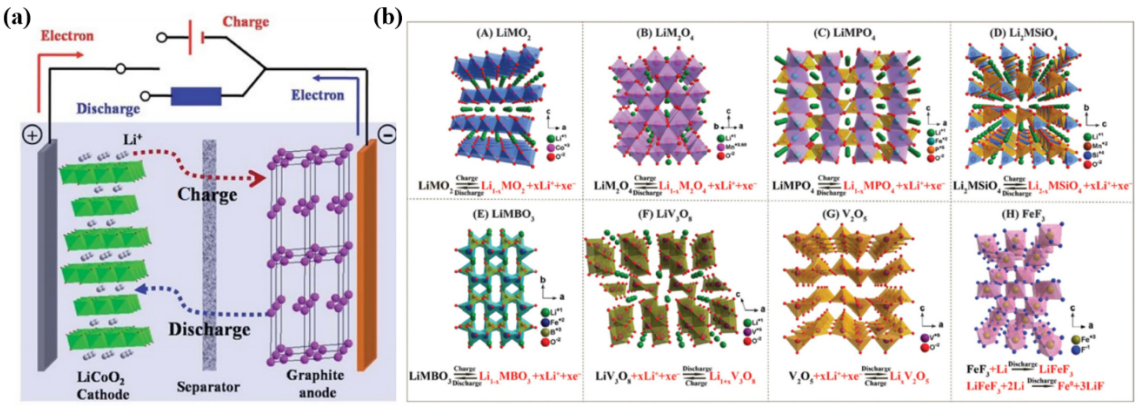

Figure 1-5. (a) Schematic of the operating mechanism of lithium-ion batteries; (b) Crystalline configurations and electrochemical reactions of some types of typical cathodes: (A) layered $LiMO_2$, (B) spinel LiM_2O_4, (C) olivine $LiMPO_4$, (D) Li_2MSiO_4, (E) $LiMBO_3$, (F) LiV_3O_8, (G) V_2O_5, (H) FeF_3. [adapted from[26]]

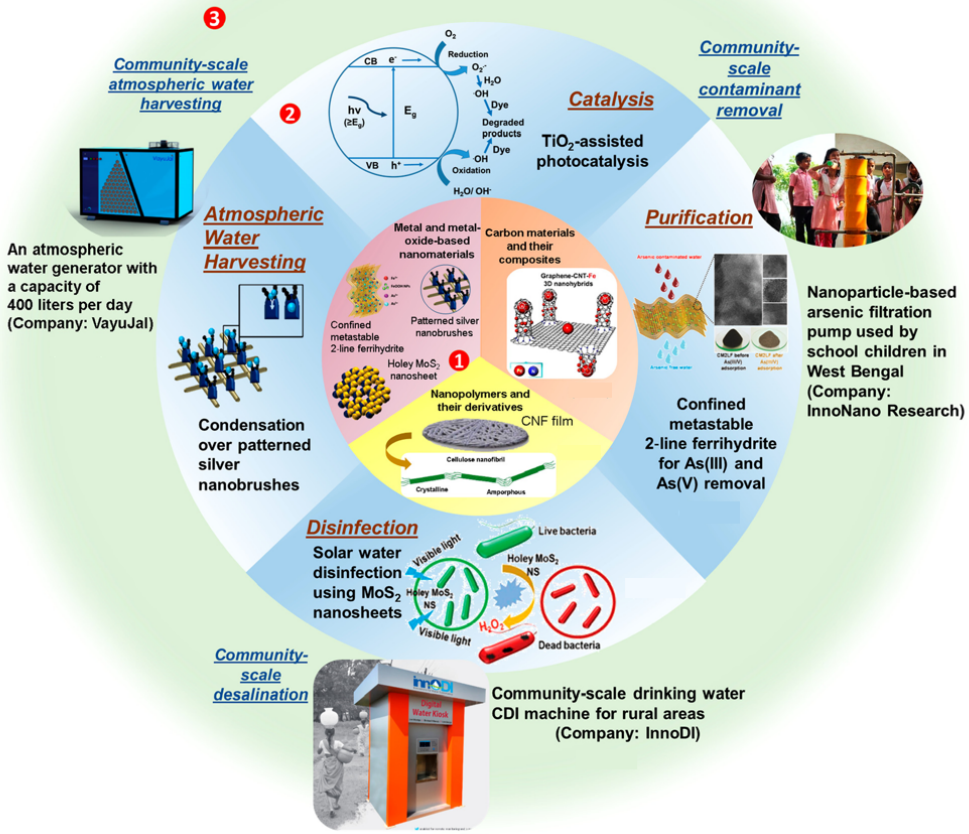

Figure 1-6. Schematic illustration of nanotechnologies applied in water treatment from lab-scale to market. Innermost circle 1 indicates materials as building blocks; middle circle 2

indicates reported phenomena using such materials, and outermost circle 3 shows products built out of research and their commercialization to create a societal impact. [adapted from[28]]

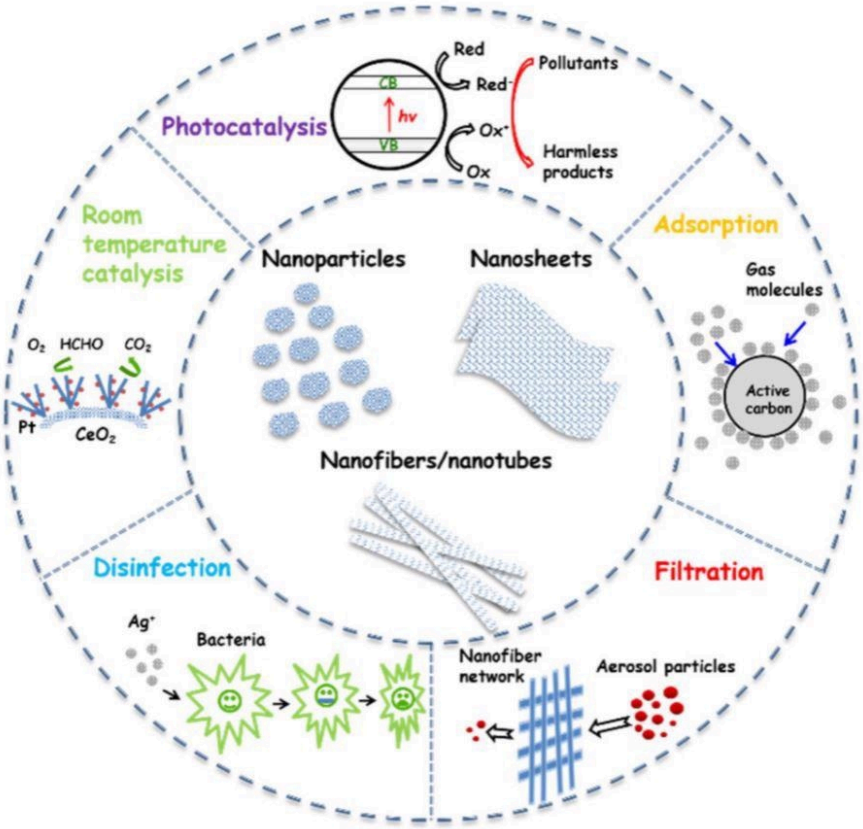

Figure 1-7. Schematic illustration of nanotechnologies applied in ambient air treatment. [adapted from[29]]

Aeronautics and astronautics industry: The application of nanodevices in the aerospace field can increase the payload and reduce energy consumption exponentially. Research in this area also includes the development of low energy consumption, radiation resistance, high-performance computers, nano integrated testing, controlling instruments and electronic equipment for micro spacecraft;[30] thermal barriers, wear-resistance nanostructured coating materials.[31]

Material processing: The nanomaterials have high surface energy, which enables them to be used as a good metallurgical sintering additive. In the process of metal processing, the sintering additives made of nanomaterials can reduce the sintering temperature of metal powder, which can simplify the process of metallurgy and get metal products with high purity.[32, 33]

1.1.3 Categorization of nanomaterials

A nanometer is a unit of length, with one nanometer equals to 10^{-9} meters. Nanomaterials refer to materials with a size between 1 nm and 100 nm in at least one dimension, or materials consist of units within the nanoscale dimension and can generally be defined as materials with nanostructures. The scale of various materials is shown in Fig. 1-8. When materials themselves or their basic units reach the nanoscale, some special phenomena appear, enduing their unique properties and giving birth to novel applications. Therefore, nanomaterials have been one of the hotspots in recent years.

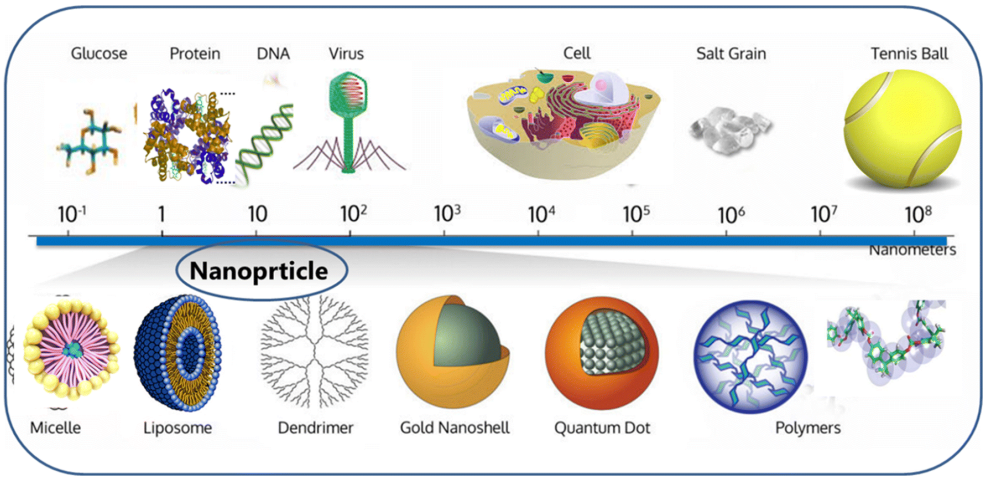

Figure 1-8. The scale size of nanoparticles (NPs) compared with some biological materials: glucose, protein, DNA, virus, bacterium, and cells of nano and micro size. In the bottom panel, a few types of NPs have represented: micelle, liposome, dendrimer, gold nanoshell, quantum dot, and polymer NPs. [adapted from[34]]

Nanomaterials can be classified differently from different perspectives. From the perspective of geometric structure, nanomaterials can be divided into zero-dimensional (0D) nanomaterials, one-dimensional (1D) nanomaterials, two-dimensional (2D) nanomaterials and three-dimensional (3D) nanomaterials, shown in Fig. 1-9.[35] 0D nanomaterials include atomic clusters, nanoparticles, et al.; 1D nanomaterials include nanowires, nanotubes, nanofibers, et al.; 2D nanomaterials include nanofilms, nanoribbons, et al.; 3D nanomaterials are bulk materials consist of nanometer basic units. Generally, 0D, 1D, and 2D nanomaterials are collectively referred to as low-dimensional nanomaterials. From the perspective of materials, nanomaterials can be divided into metal nanomaterials, inorganic non-metallic nanomaterials, and organic

nanomaterials. In terms of material properties, nanomaterials include magnetic nanomaterials, semiconductor nanomaterials, nonlinear optical nanomaterials, superconducting nanomaterials, and thermoelectric nanomaterials. From the perspective of specific applications, nanomaterials include nano-photoelectric materials, nano-biomedical materials, nano-sensitive materials, and nano-energy storage materials.

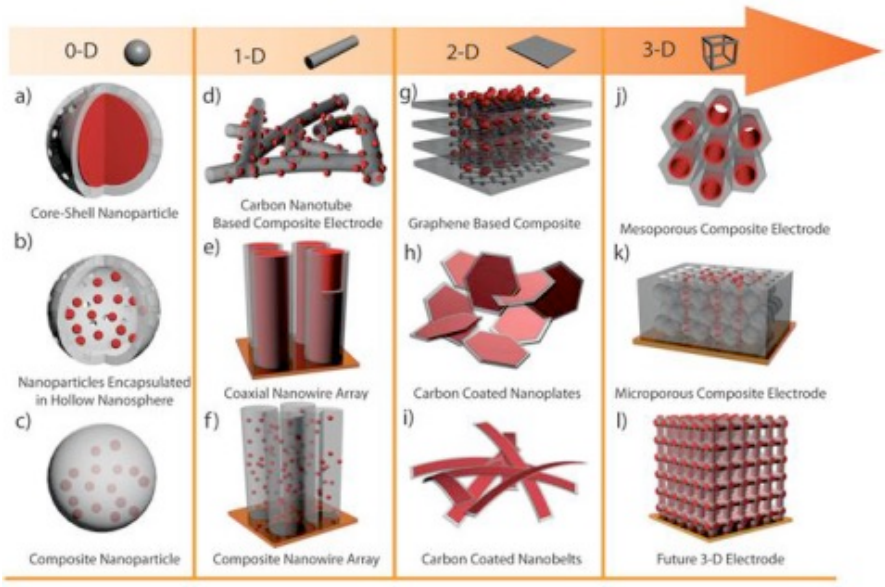

Figure 1-9. Nanomaterials categorized according to their dimension. [adapted from[35]]

1.1.4 Properties of nanomaterials

On the nanometer scale, the physical and chemical properties of materials are obviously different from those on the macroscopic scale, which makes the nanomaterials possess novel phenomena in optics, thermal, electricity, magnetism, and mechanics. In the nanoscale dimension, some traditional theories and laws are no longer applicable. For example, the concepts of elastic modulus and friction in nanomechanics have changed qualitatively and need to be redefined. In nano-electricity, Ohm's Law is no longer applicable, and a new law needs to be established. In nanobiology, new theories and laws are required to study the microcosmic mechanism of DNA and protein and artificial gene tailoring. These problems stimulate people to re-understand, define and modify the existing theory, and establish the concept and theory applicable in the world of the nanoscale. Currently, the main findings of nanomaterials have the following five effects:

Surface effect: As the size decreases, the ratio of the number of atoms on the surface to the total number of atoms (i.e., the specific surface area) of nanomaterials increases dramatically. When the size reaches the nanometer level, the sharp increase of the specific surface area (as shown in Fig. 1-10) causes a change in the properties of the nanomaterials, which is called the surface effect. Due to a large number of atoms on the relative surface, and the lack of coordination of the surface atoms, which engenders a large number of unsaturated bonds, the materials possess very high surface energy and surface activity, which also sometimes leads to structural changes.

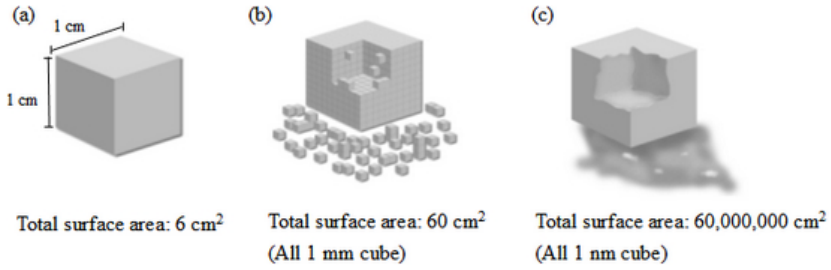

Figure 1-10. Illustration of the increase in specific surface area with smaller particle size: (a) A solid cube with 1 cm on each side; (b) Volume of 1 cm^3 filled with cubes with 1 mm on each side has 10 times larger specific surface area than that of the cube in (a); (c) Volume of 1 cm^3 filled with cubes with 1 nm on each side has 10^7 times larger specific surface area than that of the cube in (a). [adapted from[36]]

Small size effect: When the size of the nanomaterials approaches the light wavelength, electronic DE Broglie wavelength, coherence length, or the transmission depth of the superconducting state and et al., physical characteristics, such as boundary conditions for periodicity of nanomaterials will be destroyed, resulting in the change of characteristics in acoustic, optical, thermal, mechanical and electrical and magnetic aspect, which is so called the small size effect.

Quantum size effect: Band theory shows that the electron level near the Fermi level is continuous at the macroscopic size. When the size is down to the nanometer level, the electron level near the Fermi level changes from a quasi-continuous level to a discrete level, which is the quantum size effect; the effects of the quantum size effect include the transformation of the conductor to an insulator, the blue shift of the boundary of the absorption spectrum, and the luminescence nature of nanoparticles.

Macroscopic quantum tunneling effect: In classical mechanics, when the potential barrier is higher than the energy of the particle, the particle cannot cross the potential barrier. While in quantum mechanics, the probability of a particle crossing a potential barrier is not zero. The phenomenon that the particle energy less than the potential barrier can still pass through the potential barrier is called the tunneling effect. In recent years, it has been found that some macroscopic quantities, such as magnetization intensity in micro-particles and magnetic flux in quantum-related devices, also exhibit the tunneling effect, which is called the macroscopic quantum tunneling effect. The macroscopic quantum tunneling effect limits the information storage time of devices such as tape and disk. Prospectively, the macroscopic quantum tunneling effect and the quantum size effect could lay the foundation for future microelectronic devices.

Dielectric confinement effect: The dielectric enhancement of the system caused by the interface of nanoparticles dispersed in heterogeneous media is called the dielectric limited domain effect. Generally speaking, both transitional metal oxides and semiconductor particles may produce dielectric domain limiting effects, which will have important effects on the properties of optical absorption, photochemistry, nonlinear optics, and others.

1.1.5 Carbon nanomaterials

Carbon is one of the most widely distributed elements in nature and is also the most important elements constituting the organisms on the earth. Carbon atom possesses four valence electrons, and the energy levels between electron orbits are close, which makes it prone to arise orbit transition to form different hybrid structures: sp^1, sp^2, and sp^3. Thus, carbon can not only form simple carbon substances with diverse structures and nature, such as diamond, graphite, and amorphous carbon, et al. but also can form countless covalent compounds with other elements, such as various non-metallic inorganic and organic compounds, et al. Just as the importance of carbon in the macroscopic world, carbon nanomaterials also plays an important role in the microcosmic world. In recent years, as the allotropes of carbon with unique natures have been gradually discovered, such as fullerenes, carbon nanotubes, and graphene, carbon nanomaterials have attracted great attention from the world.

In 1985, Kroto and others evaporated solid graphite by laser irradiation, whereafter the generated carbon atom clusters gathered together to form a kind of novel 0D spherical structure

consisting of 60 carbon atoms, which was called C60 or fullerenes,[37] shown in Fig. 1-11-Fullerene. Structurally, the hollow 32-surface structure is similar to the modern football; thus, it is also known as the "Footballene". The discovery of fullerene is regarded to be the beginning of the carbon nanomaterials revolution and is the milestone of the rise of nanotechnology.[38] The three major contributors to the fullerene were awarded the Nobel Prize in chemistry in 1996. Afterward, researchers observed many new types of hollow carbon molecular, such as elliptic spherical, cylindrical and tubular, which have greatly enriched the fullerenes family.

In 1991, when Iijima was synthesizing fullerene by graphite through arc-discharge evaporation, some 1D coaxial tubular structures of graphene were accidentally discovered in cathode products, which were later known as carbon nanotubes (CNTs), shown in Fig. 1-11-CNTs.[39] CNTs attract researchers attention because of its excellent natures in mechanics,[40, 41] thermology,[42-44] and electricity,[45-47] which make it possessing great potential in many fields.[48, 49] The discovery of CNTs is a symbolic event indicating that nanotechnology research, especially carbon nanostructure research, stepped into a new stage.

In the 1930s, Landau and Peierls proposed that 2D single-atom-layer (SAL) materials lack thermal stability.[50, 51] Based on this opinion, the 2D SAL structure was only considered to be an indispensable part of 3D structures, which normally forms by epitaxial growth in accordance with the lattice structure on the surface of the 3D structure. Consequently, there would be no 2D SAL structure without a 3D substrate, and the graphene, as a SAL structure of graphite, was considered not able to exist independently. However, as fullerenes, carbon nanotubes have been discovered successively, and with the development of nanotechnology, researchers started looking again into graphene. In 2004, Novoselov et al. successfully isolated graphene (shown in Fig. 1-11-Graphene) by mechanical peeling,[52] which broke people's false cognition on 2D materials and opened up a new field of research. As a result, two major contributors of graphene were awarded the 2010 Nobel prize in physics. From the first isolation of graphene in 2004, countless important discoveries have been proposed.[53] It was indicated that graphene is a transparent and soft "super material" with the highest mechanical strength, the highest thermal conductivity, and the lowest electrical resistivity in the world.[54] Because of the mentioned natures, graphene is promising to be applied in many fields, such as sensors, machinery, flexible electronics, optoelectronic devices, energy storage, composite material, and biomedical, et al.[55]

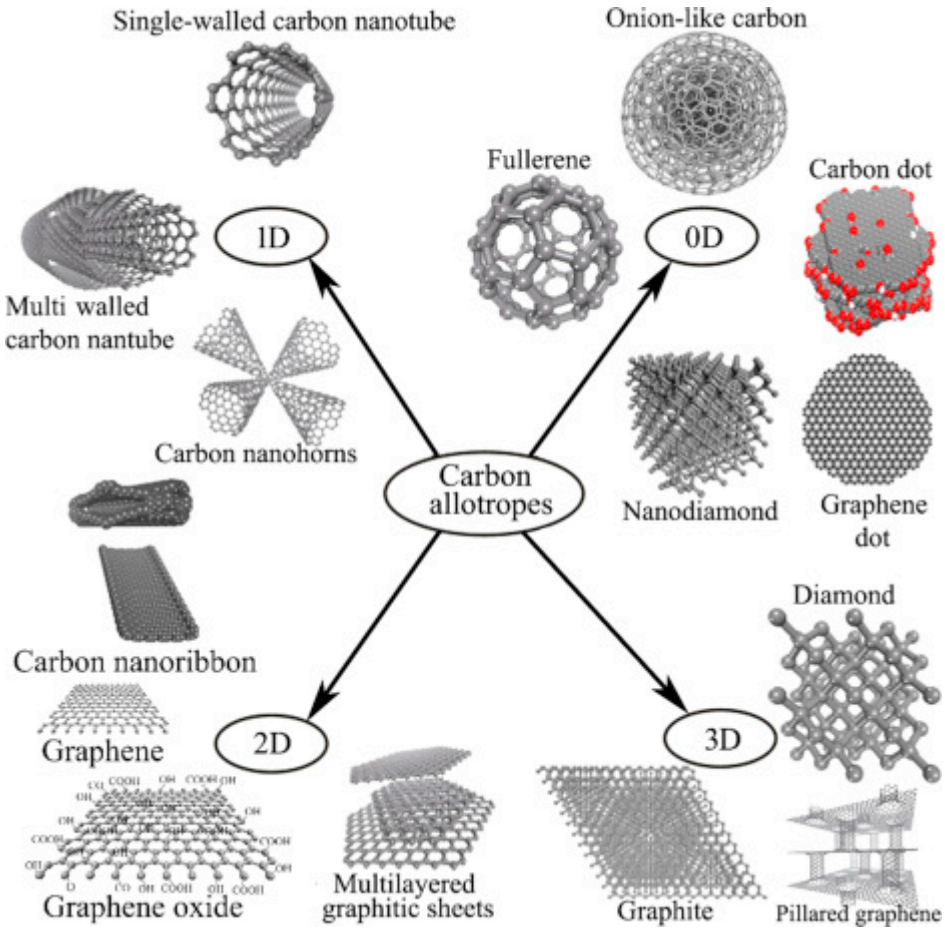

Figure 1-11. Illustration of various carbon allotropes with different structures from 0D to 3D. [adapted from[56]]

A typical Raman spectrum of a defect-containing graphene is shown Fig. 1-12a, in which two characteristic peaks called the D band (~1345 cm-1) and the G band (~1585 cm-1) appear. The D band is corresponding to the second-order scattering process involving a defect and a phonon, while the G band is corresponding to a first-order resonance Raman scattering process. In a CNT, the graphite-like G band originates from the stretching mode in the graphite plane, as shown in Fig. 1-12b, which is relatively stable. Thus, in view of the chemical stability of CNT and the stability of G band, the CNT is selected as a standard regarding the TERS performance evaluation in the following chapters.

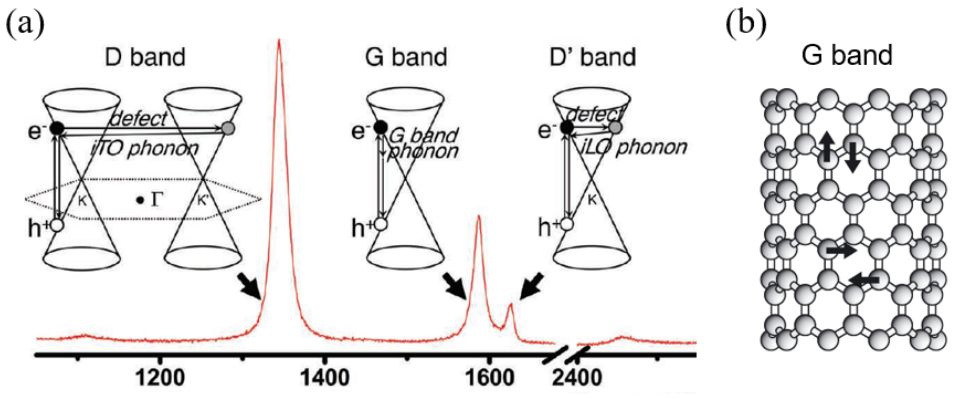

Figure 1-12. (a) Typical Raman spectrum of defect-containing graphene; [adapted from[57]] schematic illustration of the atomic vibrations of the G band. [adapted from[58]]

1.2 Introduction of Tip-Enhanced Raman Spectroscopy (TERS)

1.2.1 Introduction of Raman Spectroscopy

The Raman scattering theory was first proposed by Smekal in 1923 and was the first experimental demonstrated by Raman and Krishnan in 1928.[59, 60] When parallel light illuminates gas, liquid, or transparent crystal samples, most of the light propagates along the original direction while a small part of light scatters at a different angle, which is called light scattering. Scattering occurs when photons collide with molecules. If the collision accompanies no energy exchange, the frequency of the scattered light is the same as that of the incident light, which is called elastic scattering or Rayleigh scattering.[61] On the other hand, if the collision accompanies by an energy exchange, the frequency of scattered light changes, which is called inelastic scattering or Raman scattering.[62] The Raman scattering consists of two situations:

Stokes scattering: when the frequency of the scattered light is lower than that of the incident light, the scattering phenomenon is called Stokes scattering. In the Stokes scattering, the molecule obtains energy from the photon. Consequently, the molecule ends up being in a higher vibrational energy state.

Anti-Stokes scattering: when the scattered light possesses a higher frequency than that of the incident light, the scattering phenomenon is called anti-Stokes scattering. In the anti-Stokes scattering, the energy of the molecule is transferred to the photon. Consequently, in the anti-Stokes scattering, the molecule should be in an excited vibrational state at the beginning and end up in a lower vibrational energy state (the ground state).

Theoretically, Raman scattering can be explained by the classical theory of molecular polarizability.[63, 64] When a molecule interacts with light (electromagnetic wave), its electron cloud is disturbed by the electric field (E), resulting in the separation of electrons and nuclei. Consequently, an electric dipole moment (μ) is generated by the molecule, which characterizes the Raman scattering. The induced dipole moment μ could be expressed as the equation 1-1:

$$\mu = \alpha \cdot E \qquad 1-1$$

where α refers to the polarizability of the molecule, which is the tendency of the molecule to distort its charge distribution by an external electric field E. The molecular polarizability α is

a function of the instantaneous position of the constituent atoms, and it could be expressed by equation 1-2:

$$\alpha = \alpha_0 + (q - q_e) \cdot \frac{\partial_\alpha}{\partial_q} \qquad 1-2$$

Where α_0 refers to the polarizability of the molecule at the equilibrium position; q refers to the bond lengths at any instant position; q_e refers to the bond lengths at the equilibrium position. Assuming the molecule is in simple harmonic motion, the $q - q_e$ could be expressed as equation 1-3:

$$q - q_e = q_{max} \cdot \cos 2\pi\nu_{vib}t \qquad 1-3$$

Where q_{max} refers to the maximum separation distance between atoms relative to their equilibrium position; ν_{vib} refers to the vibrational frequency of a molecule. Consequently, by substituting equation 1-3 into equation 1-2, equation 1-4 is deduced:

$$\alpha = \alpha_0 + q_{max} \cdot \cos 2\pi\nu_{vib}t \cdot \frac{\partial_\alpha}{\partial_q} \qquad 1-4$$

Accordingly, by substituting equation 1-4 into equation 1-2, equation 1-5 is deduced:

$$\mu = E \cdot \left(\alpha_0 + q_{max} \cdot \cos 2\pi\nu_{vib}t \cdot \frac{\partial_\alpha}{\partial_q}\right) \qquad 1-5$$

Notating the frequency of the electromagnetic wave as ν, the electric field could be expressed as equation 1-6:

$$E = E_0 \cdot \cos 2\pi\nu t \qquad 1-6$$

Where E_0 refers to the amplitude of the electromagnetic wave. Then, substituting into equation 1-5, equation 1-7 is deduced:

$$\mu = E_0 \cdot \cos 2\pi\nu t \cdot \left(\alpha_0 + q_{max} \cdot \cos 2\pi\nu_{vib}t \cdot \frac{\partial_\alpha}{\partial_q}\right) \qquad 1-7$$

Then, the equation 1-7 could be further deduced as equation 1-8:

$$\mu = \alpha_0 \cdot E_0 \cdot \cos 2\pi\nu t + q_{max} \cdot \cos 2\pi\nu_{vib} t \cdot \frac{\partial_\alpha}{\partial_q} \cdot E_0 \cdot \cos 2\pi\nu t \qquad 1-8$$

Finally, the equation could be presented as equation 1-9:

$$\mu = \alpha_0 \cdot E_0 \cdot \cos 2\pi\nu t + q_{max} \cdot \frac{E_0}{2} \cdot \cos[2\pi(\nu - \nu_{vib})t] \frac{\partial_\alpha}{\partial_q} + q_{max} \cdot \frac{E_0}{2} \cdot \cos[2\pi(\nu + \nu_{vib})t] \frac{\partial_\alpha}{\partial_q} \qquad 1-9$$

Equation 1-9 consists of three terms, which correspond to Rayleigh scattering with the frequency ν, the Stokes scattering with the frequency $(\nu - \nu_{vib})$, and the anti-Stokes scattering with the frequency $(\nu + \nu_{vib})$. Raman scattering is a complex interaction. As a concise summary, possessing variational polarizability is necessary for a molecule to be Raman-active, while the procedure of Raman scattering is affected by polarizability.

From the microcosmic perspective, Raman scattering also can be explained by quantum mechanics.[63, 65] The scattering process can be understood as follows. The illustration of light scattering and the corresponding Jablonski diagram are shown in Fig. 1-13a and b, respectively. The electron with its vibrational level at the electronic ground state V_0 in the molecule absorbs the energy and is excited to a virtual energy state, followed by falling back to the same vibrational level (ground state); simultaneously, a photon with the energy equals to that of the incident photon is emitted, which is called Rayleigh scattering. If the electron falls back to the excited vibrational level of the electronic ground state V_1, a photon of less energy than that of the incident photon is emitted, which is called Stokes scattering. If the molecule is in an excited vibrational level of the electronic ground state V_1, the electron of the excited vibrational level of the electronic ground state in the molecule absorbs the photon and excites to a virtual energy state, followed by falling back to the vibrational level of the electronic ground state V_0, simultaneously, a photon with higher energy to that of the incident photon is emitted, which is called anti-Stokes scattering. Since most molecules are in the ground state at room temperature,[66] the probability of occurrence of anti-Stokes scattering is much lower than that of Stokes scattering. Thus, in terms of Raman measurement, it generally refers to Stokes scattering.

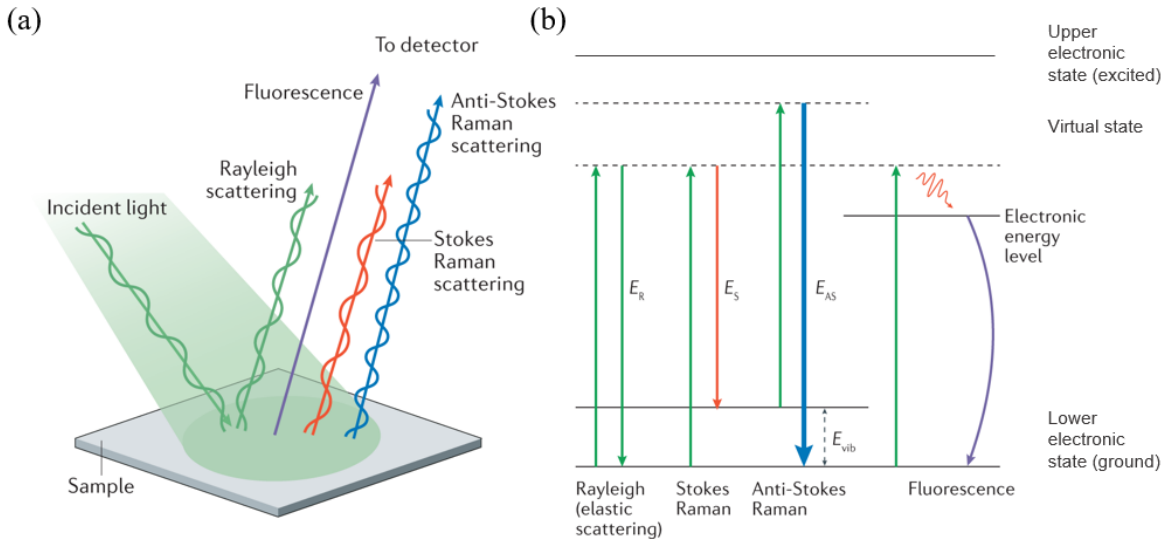

Figure 1-13. (a) The illustration of scattering; (b) the corresponding Jablonski diagram to (a). [adapted from[67]]

In Raman scattering, the change in the frequency of light is only related to the vibrational modes of the molecular electronic ground state. Thus, each molecule has a unique Raman spectrum, which makes the Raman spectrum the "molecular fingerprint" of a molecule. Therefore, Raman spectroscopy could be used as a spectroscopic method to precisely analyze the structure of a molecule. Besides the specificity, the Raman scattering technique possesses the following advantages: high sensitivity, non-invasive measurement, simple preparation of the sample, the ability to measure biological samples, and the ability to simultaneously detect different analytes, et al.[68, 69] Although possessing the aforementioned advantages, the intensity of Raman scattering is inherently weak, limiting its further applications.

To overcome this issue, the surface-enhanced Raman spectroscopy (SERS) technique has been developed. Besides the aforementioned advantages of Raman scattering, SERS achieves dramatic enhancement of the intensity of the Raman signal. In 1974, SERS was first discovered from a pyridine-modified rough silver electrode by Fleischmann et al.[70] Afterwards, the enhancement was confirmed independently by Jeanmaire et al. and by Albrechtand et al. in 1977.[71, 72] By far, SERS has been extensively studied and has become sensitive enough to observe a monolayer species on the metal surface, and even single molecule.[73]

Although SERS dramatically broadened the application of Raman, it still possesses some limitations. Two of the most severe limitations in the application of SERS are: the requirement that the surface is roughened or nanostructured Ag, Au, or Cu, which results in the inapplicability of SERS in fields such as ultrahigh vacuum single-crystal surface science, electrochemistry, heterogeneous catalysis, microelectronics, tribology, and et al.;[74, 75] and the relatively poor spatial resolution which determined by the SERS-active hotspot.[76] To increase the universality of the SERS technique, on the one hand, many efforts have been put into the development of SERS substrates, shown in Fig. 1-14;[77] and on the other hand, an innovatory technique called tip-enhanced Raman spectroscopy (TERS) emerged as the times require.[78-80]

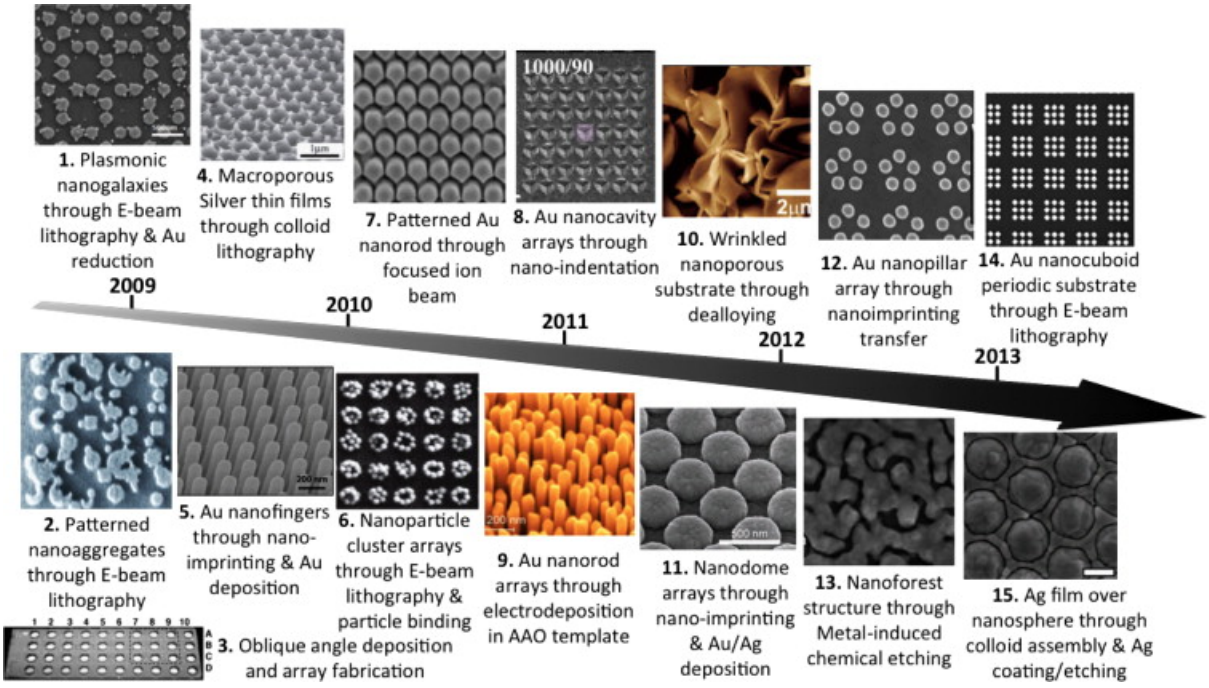

Figure 1-14. Advanced SERS-active substrates. [adapted from[77]]

1.2.2 Introduction of TERS

Generally, TERS was recognized to be born around 2000.[78, 81, 82] However, since TERS is a technique combining Raman spectroscopy and scanning probe microscopy (SPM), there is a prehistory of TERS in the 1980s and 1990s. In 1982, Binnig et al. introduced scanning tunneling microscopy (STM), which enabled the atomic-scale resolution imaging of surface morphology.[13] In 1985, Wessel developed surface-enhanced optical microscopy by illuminating a laser onto a single metal nanoparticle,[83] which is regarded as the prototype of aperture-less scanning near-field optical microscopy (SNOM). In 1994, Inouye and Kawata

reported the detection of scattered light from the near field of a stainless-steel tip, indicating a combination of surface-enhanced spectroscopy in their system.[84] In 2000, Kawata,[81] Zenobi,[78] and Anderson[82] groups independently proposed the TERS technique by different methods, which is a milestone in the field of plasmon-supported Raman spectroscopy. Specifically, Kawata's group used Ag-coated AFM tips and rough Ag film substrates; Zenobi's group and Anderson's group used dielectric substrates with the tip working as a nanoantenna supporting the surface plasmon. In the last two decades, the TERS technique has developed dramatically and demonstrated its experimental value in many frontier fields.

1.2.3 Mechanisms of TERS

1.2.3.1 Electromagnetic mechanism

The enhancement mechanisms of TERS insist on electromagnetic (EM) and photo-driven charge transfer (CT) mechanisms, amongst which the EM mechanism contributes dominantly.[85] More specifically, the EM contains three different mechanisms: (i) surface plasmon resonances, (ii) lightning rod effect, and (iii) antenna resonances.[86] Fig. 1-15 shows the simulation of the electric field amplitude map of the apex of an Ag TERS probe irradiated by a laser of 532 nm wavelength.

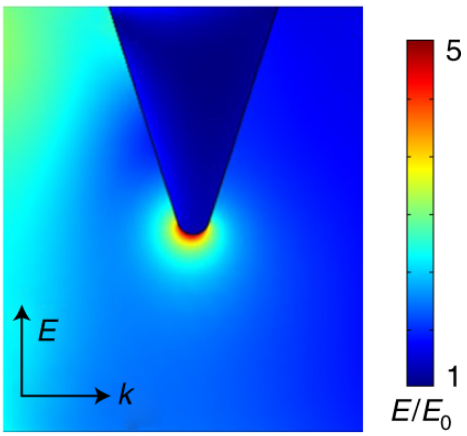

Figure 1-15. Simulation of the electric field amplitude map of the apex of an Ag TERS probe irradiated by a laser of 532 nm wavelength. [adapted from[87]]

The excitation of surface plasmon resonance (SPR)[88] amplifies the electromagnetic field in the vicinity of the surface of the metallic nanostructure, resulting in electromagnetic enhancement. The SPR refers to the collective oscillations of the conduction electrons at the surface of the

metallic nanostructure, including propagating surface plasmon polaritons (SPPs) and localized SPR (LSPR),[89, 90] which are schematically illustrated in Fig. 1-16.[91] SPPs are the propagating wave for the order of micrometers, emerging when light is trapped at the interface between a metal and a dielectric.[90, 92] When the incident light satisfies the following conditions: (i) the size of the interacted nanostructures is much smaller than the incident wavelength, and (ii) the frequency of the excitation light matches the frequency of the localized surface plasmon, the LSPR occurs, which could be well modulated by the size, shape, and composition of nanostructure and the surrounding dielectric medium.[89, 93] The LSPR contributes to a great enhancement of the localized electromagnetic field, underlying enhancement of the TERS/SERS effect.[94] The enhancement is approximatively proportional to the fourth power of the strength of the local electromagnetic field.

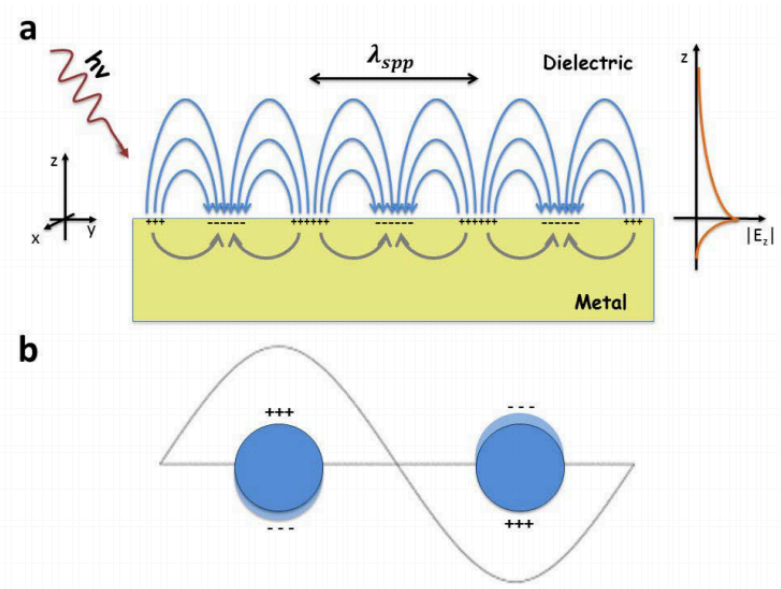

Figure 1-16. Schematic diagrams illustrating a surface plasmon polariton (a) and a localized surface plasmon (b). [adapted from[91]]

For a plasmonically active, conductive, and sharp nanotip under laser irradiation, the apex allows significant concentrating of the surface charges, during which procedure the nanotip serves as a lightning rod, leading to strong optical resonances and highly confined local electromagnetic fields. This phenomenon is called the lightning rod effect,[95, 96] which depends on the geometry and conductivity of the tip material while it is independent of the frequency of the incident light.[97] The strong electromagnetic field could cause enhanced Raman scattering,

resulting in highly intensified and localized Raman signals of target molecules under the nanotip with the confined field far below the diffraction limit.

As with conventional antennas in the radio or microwave regimes, if the dimension of the tip is scaled characteristically to an effective incident wavelength, antenna resonances occur, which is similar to the excitation of surface plasmon.[98, 99] Among these mentioned three mechanisms, the antenna resonance is the least important field enhancement mechanism in TERS.

As for the procedure of electromagnetic enhancement, it could be viewed as two distinct processes:[100]

The local field enhancement. The excitation of SPR generates a large amplification of the electromagnetic field in small spatial regions. Accordingly, the molecules in such regions are exposed to the greatly enhanced electromagnetic field.

The radiation enhancement. Since the power radiated by the Raman-active molecule relies on the surrounding environment, the presence of the metallic nanostructure greatly enhances the process.

1.2.3.2 Photo-driven charge transfer

The transfer of the electrons occurs from the substrate/probe to the molecule or vice versa under photonic excitation, requiring the Fermi level of the metal structure to be located between the ground state of the molecule and the excited state of the molecule.[101] Two models of charge transfer processes are illustrated in Figure 1-17.[102] Specifically,[102, 103] Fig. 1-17a refers to the charge transfer from the ground state I of the molecule to the Fermi state F of the metal structure. The vibronic coupling h_{FK} of F and the excited molecular states K allows the charge transfer intensity μ_{IF} to borrow intensity from the transition intensity μ_{IK}. Fig. 1-17b refers to the charge transfer from F to K. The vibronic coupling h_{IF} of I and F allows the charge transfer intensity μ_{FK} to borrow intensity from the transition intensity μ_{IK}. Notably, although this chemical mechanism has been wildly exploited in the studies of nonmetal-based enhanced Raman scatting, such as semiconductor, graphene, and metal-organic framework, it contributes very little enhancement in TERS.

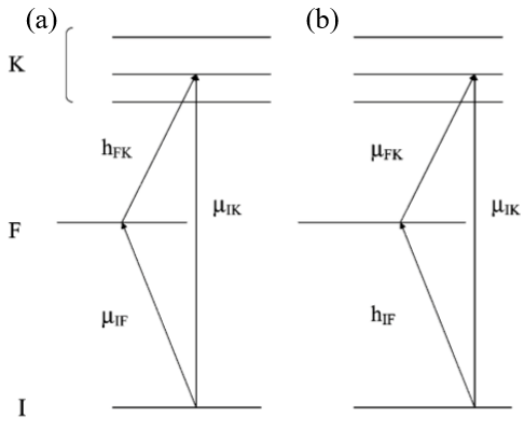

Figure 1-17. Schematic energy level diagram of the two models (a and b) of the charge-transfer processes in a metal-molecule system, where I refers to the ground state of the molecule; K refers to the excited state of the molecule; M refers to the Fermi state of the metal substrate. [adapted from[102]]

1.2.3.3 TERS enhancement mode

Strong field intensity and confinement occur when approaching the TERS-active tip to a plasmonic substrate (Au, Ag, and Cu) to 1~2 nm due to the electromagnetic coupling between the apex of the tip and the substrate, which is called the "gap mode" effect,[104] as shown in Fig. 1-18a.[105] On the contrary, if there is no coupling between the tip and the substrate, the procedure is called the "non-gap mode" effect, as shown in Fig. 1-18b,[105] in which the TERS enhancement could be weaker by 2~3 orders than that of the coupled case.[106] The finite difference time domain (FDTD) simulations of the electric field distribution in the gap and non-gap mode are shown respectively in Fig. 1-18c and d.[107] Besides the enhancement mode, there are many other factors also affect the enhancement of the confined field, such as the tip material and geometry, incident laser wavelength, focus, polarization, incident angle, et al.[108]

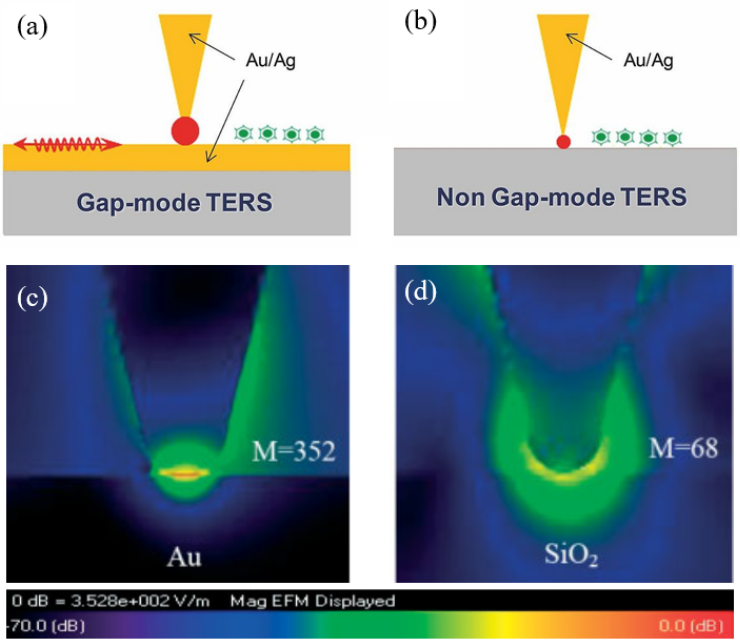

Figure 1-18. Schematic illustration of gap mode TERS (a) and non-gap mode TERS (b); [adapted from[105]] and the FDTD simulations of the electric field distribution in the gap (c) and non-gap (d) mode with the distance between the Au tip and the substrate equals 1 nm, where M refers to the maximum field enhancement. [adapted from[107]]

1.2.4 Experimental system of TERS

As mentioned in section 1.2.2, the TERS system consists of two main techniques: Raman spectroscopy and SPM, in which the incoming laser beam needs to be focused onto the plasmonically active tip, the tip has to be in close proximity to the surface of the target sample under stable feedback, and the scattered Raman signal needs to be efficiently detected. Thus, in section 1.2.4, the experimental system of TERS is discussed in 3 aspects: instrumental configurations based on optical geometries, feedback modes, and the plasmonically active tip.

1.2.4.1 TERS instrumental configurations

Normally, based on the optical geometries, the configurations of the TERS setup are classified by the direction of excitation illumination, including top illumination, bottom illumination, and side illumination, shown in Fig. 1-19a, b, and c, respectively.[109] Specifically, top illumination mode, also called reflection mode, conducts illumination and signal collection both from the topside of the sample, possessing the advantage of working on both transparent and opaque

samples, while the shadowing of the TERS tip becomes the main challenge in this mode, which blocks a certain amount of the excitation light and the signal.[110] The bottom illumination mode, also called transmission mode, conducts illumination and signal collection both from the downside of the sample through an inverted optical microscope, which limits this mode to only transparent samples and substrates. It is worth noticing that this mode was chosen for the first TERS experiments.[78, 81, 82] The side illumination mode conducts illumination and signal collection both from the side of the tip apex of the SPM at an angle of 45°~ 80° through a long-working distance objective. This mode is commonly used for opaque samples and can avoid the shadowing issue suffered in top illumination mode. However, the existence of the angle between incident light and tip also results in the elliptical and relatively large focal spot, which leads to a stronger far-field background and requires higher laser power in the practical experiment to obtain comparable results.

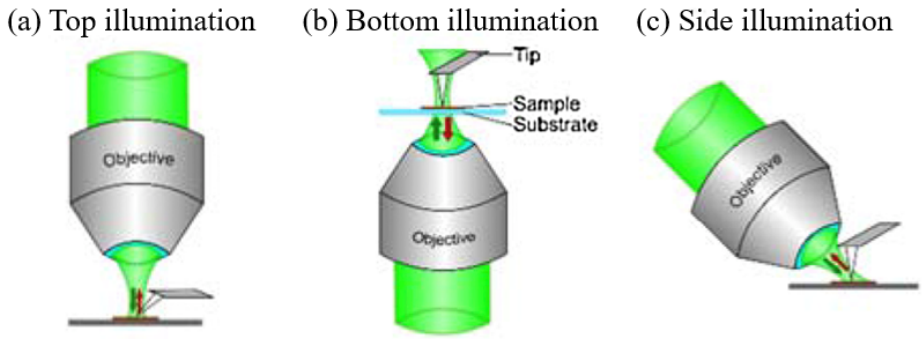

Figure 1-19. Schematic illustration of the configurations of TERS setup based on optical geometries: (a) top illumination, (b) bottom illumination, (c) side illumination. [adapted from[109]]

1.2.4.2 Feedback control

TERS measurements require the plasmonically active tip to be in close proximity to the surface of the target sample, which distance needs to be precisely controlled since the detected signal decays dramatically as the tip-sample distance increases.[107] Here, the feedback control in AFM, STM, and shear force microscopy (SFM) is discussed separately.

The feedback control in the AFM system basically depends on measuring the atomic or molecular interactions between tip and sample,[14] which specifically includes the Van der Waals forces, capillary forces, chemical bonding, or repulsive electrostatic forces. AFM can be

realized under contact mode and intermittent contact mode, which is also called tapping mode or semi-contact mode. Specifically, under the contact mode, atomic force is induced at the tip-sample junction, resulting in the nanoscale position change of the cantilever and consequently leading to the reflection position change of a feedback laser cast on the cantilever, through which the surface information of the sample is detected by a position-sensitive photodiode, shown in Fig. 1-20a.[111] While under the intermittent contact mode, the tip is continuously oscillating at its mechanical resonance frequency, gathering the surface information through the frequency change induced by the interaction between the tip and the sample, shown in Fig. 1-20b.[112] For AFM-TERS in contact mode, the tip direct contact with the sample, providing a high signal enhancement, while in intermittent contact mode, the interaction time depends on the oscillation amplitude of the tip, which should be small enough (<5-10 nm) to maintain the oscillation within the evanescent field,[107] which can be achieved by two approaches. Firstly, through the time-gated illumination technique, the excitation laser is modulated to be synchronized with the tip oscillation, obtaining the enhanced signal only under the near-field region (when the tip is down).[113] Secondly, by synchronizing a detector with the tip oscillation or coupling the Lock-In amplifier to a fast detector with its detection window fixed to the "tip down" signals, the near-field contribution can be automatically distinguished from the far-field background.[114]

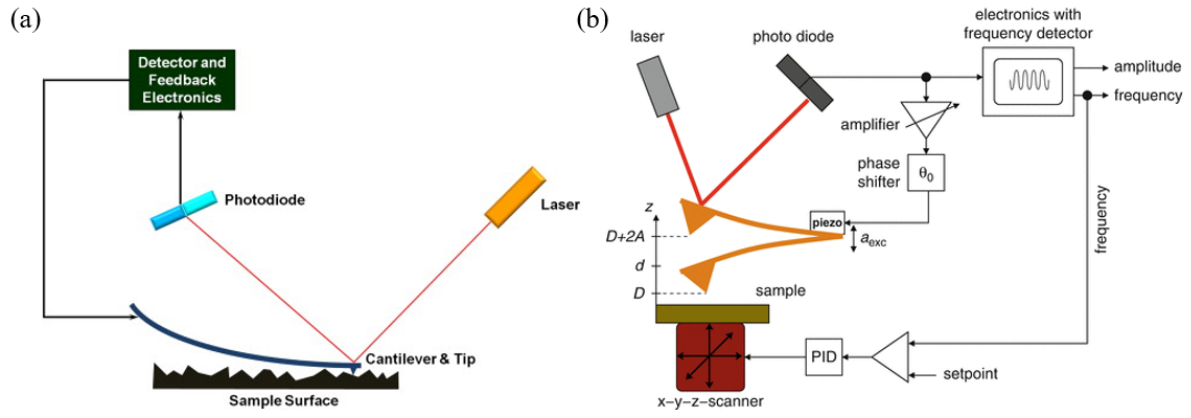

Figure 1-20. Schematic illustration of the AFM feedback loop: (a) contact mode; [adapted from[111]] (b) intermittent contact mode. [adapted from[112]]

The STM principle is based on electron tunneling, requiring the tip and substrate to be conductive. The voltage difference (bias, Eb) is applied between the tip and substrate as the tip approaches very close to the surface, enabling electron tunneling, which relates to the tip-

sample distance. Through a feedback loop, the constant tunneling distance or constant tunneling current (It) could be maintained, as shown in Fig. 1-21,[115] from which the surface information of the sample could be obtained. For STM-TERS, excellent small tip-sample distance control is advantageous for signal enhancement and high spatial resolution. Besides, the fast, economic tip preparation also benefits its application. However, the principle of STM requires the sample to be either very thin or conductive, which restricts the applicative sample range and possible optical geometries.

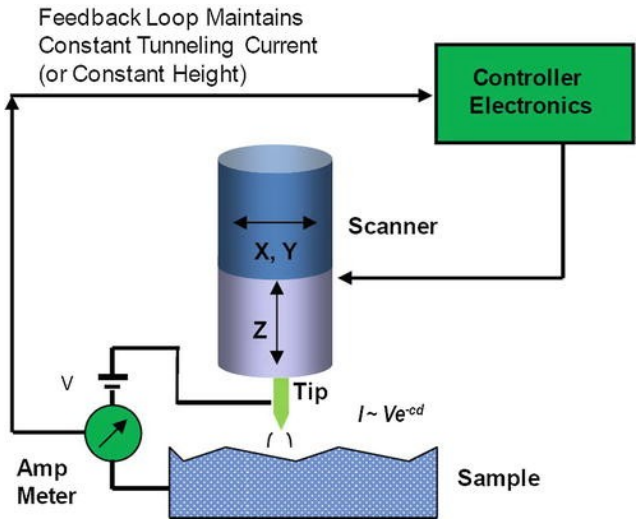

Figure 1-21. Schematic illustration of the STM with the feedback loop maintaining either constant-height or constant-current mode [adapted from[115]]

The feedback method of SFM is similar to that of the AFM. The difference is that in SFM, the shear forces are used to control the tip-sample distance, in which the tip oscillates horizontally with respect to the surface of the sample. Based on the damping of the free oscillation amplitude or the resonance frequency shift of the tip as it approaches the sample surface, feedback control could be achieved. Owing to its principle, the SFM possesses no sample restriction, which is the same as the AFM systems. SFM-TERS, in which the tip-sample distance is kept constant (2-5 nm) by the feedback loop, possesses the main advantages of easy tip preparation and high adaptability to various optical geometries.[109]

1.2.4.3 Plasmonically active tip

As discussed in section 1.2.3, the great enhancement of the Raman signals is mainly contributed by the electromagnetic enhancement of the plasmonically active hotspots through

LSPRs, making The plasmonically active tip the most crucial element in a TERS system, through which the information from the sample is obtained. Normally, a metal or metal-coated nanoscale tip controlled by an SPM feedback is used as a TERS probe. There are many factors that dominate the TERS performance of the tip: the plasmonic activity, geometric size, and morphology of the tip dominate the enhancement and the spatial resolution;[116] the stability of the tip determines the reproducibility of TERS measurements; the fabrication difficulty and cost determine the wideness of application.

(1) Plasmonically activity: only limited kinds of metal show plasmonic activity (eg. Ag, Au, Al, Cu), and the enhancement will be strong when the LSPRs wavelength approximately matches the excitation wavelength. The LSPRs peak wavelength could be experimentally obtained from the extinction spectrum and theoretically simulated by the Mie theory,[117-119] derivating from the ideal spherical nanoparticle model, as shown in equation 1-10 below:

$$\sigma = 24\pi r^3 \frac{{\varepsilon_m}^{3/2}}{\lambda} \frac{\varepsilon_2}{(\varepsilon_1 + 2\varepsilon_m)^2 + {\varepsilon_2}^2} \qquad 1-10$$

Where r refers to the radius of the nanoparticle, λ refers to the wavelength of the extinction radiation, ε_m refers to the dielectric constant of the medium, while ε_1 and ε_2 refers to the real and imaginary components respectively of the dielectric function of the metal nanoparticles. Specifically, the real component of the dielectric function dominates the magnitude of polarization of the nanomaterial under an electric field,[120] while the imaginary component dominates the optical losses (both the inter-band and intra-band) through approaches such as plasmon damping.[121] Taking Au and Ag as examples, Fig. 1-22 shows the real and imaginary components,[121] which change along with the extinction wavelength. The real components show a similar trend, while the imaginary components show a significant difference, from which Ag possesses less optical loss and consequently, shows a stronger Raman enhancement effect among noble metal substrates.[122] Different metals show different optimum extinction wavelengths; when it matches the excitation wavelength, strong Raman enhancement could be achieved. Specifically, for excitation under visible spectral regions, Au and Ag are most commonly used, while in the UV and deep UV spectral regions, Al is commonly used as tip material.[123, 124]

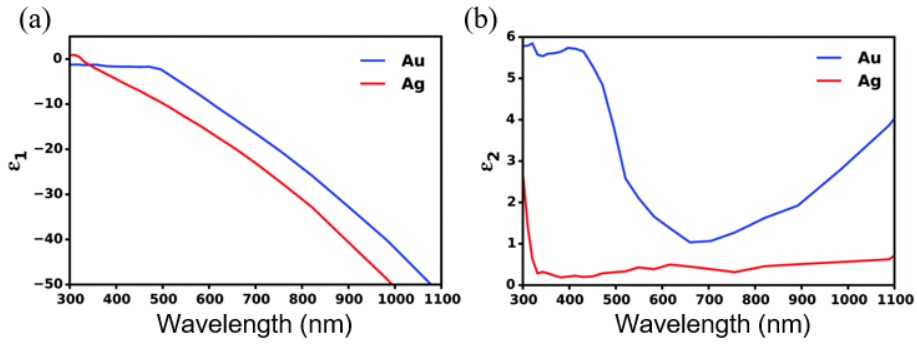

Figure 1-22. (a) The real component and (b) the imaginary component of the dielectric function for Au and Ag. [adapted from[121]]

(2) Geometric size and morphology: the size and morphology of the metal nanostructures dominate the near-field, consequently affecting its Raman enhancement and spatial resolution.[125] When the nanostructures are too small, the electrical conductivity could be extremely low, resulting from the dominating of the surface electronic scattering, leading to poor polarizability and consequently the weak Raman enhancement.[126, 127] With the size increasing, the Raman enhancement increases since the amount of excited electrons increases.[128] While the size is up to the level of the excitation wavelength; the nonradiative modes could be the domination, diminishing the Raman enhancement.[129] On the other hand, the morphology could greatly affect the distribution of the near-field, resulting in area-dependent Raman enhancement. As discussed in section 1.2.3, strong electromagnetic fields emerge at the edge and corners[130] of nanostructures resulting from the lightning rod effect, shown in Fig. 1-23.[131] Noticeably, the morphology could also affect the LSPRs wavelength, which needs to be analyzed case by case.

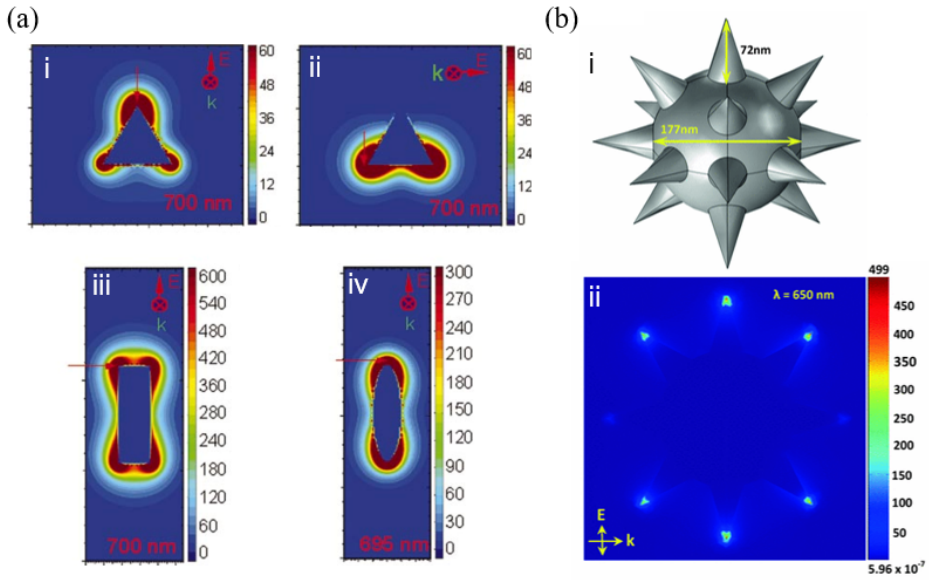

Figure 1-23. (a) Localized electric field enhancement on Ag nanostructures with different morphologies: i and ii are the field contours on a triangular prism polarized along the two different primary symmetry axes, while iii and iv are the field contours on a rod and spheroid polarized along their long axes, in which the arrows show the location of the maximum electric field; [adapted from[131]] (b) i shows the 3D illustration of an Au nanostar (AuNS) with 18 spikes, and ii shows the electric field enhancement on the surface of the AuNS (shown in i) excited by a 650 nm wavelength plane wave, both of which are modeled by COMSOL. [adapted from[132]]

(3) Stability, fabrication difficulty and cost: the stability of the tip determines the reproducibility of TERS measurements. The oxidation issue of Ag, Cu, and Al could dramatically reduce the TERS activity of the tip, which narrows the application of TERS. The fabrication difficulty and cost determine the wideness of the application. The traditional vacuum evaporation tip fabrication method, which will be discussed below, has the disadvantages of low reproducibility and high cost, which also prevents TERS from the wide application. Therefore, fabricating high-enhancement, stable, and low-cost TERS tips is essential to the application and development of the TERS technique.

After discussing the factors affecting the performance of tips, the TERS tips coupling with different SPM, including AFM, STM, and SFM, are introduced below, respectively.

AFM-TERS: for AFM-based TERS, traditionally, tips are fabricated through vacuum evaporation of the plasmonic active metal (Au, Ag, and Al) onto commercial AFM cantilevers

(Si / Si_3N_4), as shown in Fig. 1-24a.[133] The material, evaporation ratio, and annealing temperature dominate the morphology of the deposited metal films or grains.[134-136] Although the vacuum evaporation method is commonly used, it suffers from drawbacks of low reproducibility, high cost, and time-consuming. Besides, the pulsed electrodeposition method could also be used in the fabrication of AFM-TERS tips, as shown in Fig. 1-24b.[137] Furthermore, there are some specialized methods for AFM-TERS tips fabrication, such as bonding Ag nanoparticles to the AFM tip apex by photoreduction, shown as Fig. 1-24c;[138] bonding Au nanoparticle to the AFM tip followed by chemical reduction to form a nanostar as the TERS-active center, shown as Fig. 1-24d;[139] colloidal depositing nanoparticles onto the AFM tip apex, shown as Fig. 1-24e;[140] functionalizing Ag nanowires (AgNWs) to the apex of AFM tip through alternating-current dielectrophoresis (AC-DEP), shown as Fig. 1-24f.[141]

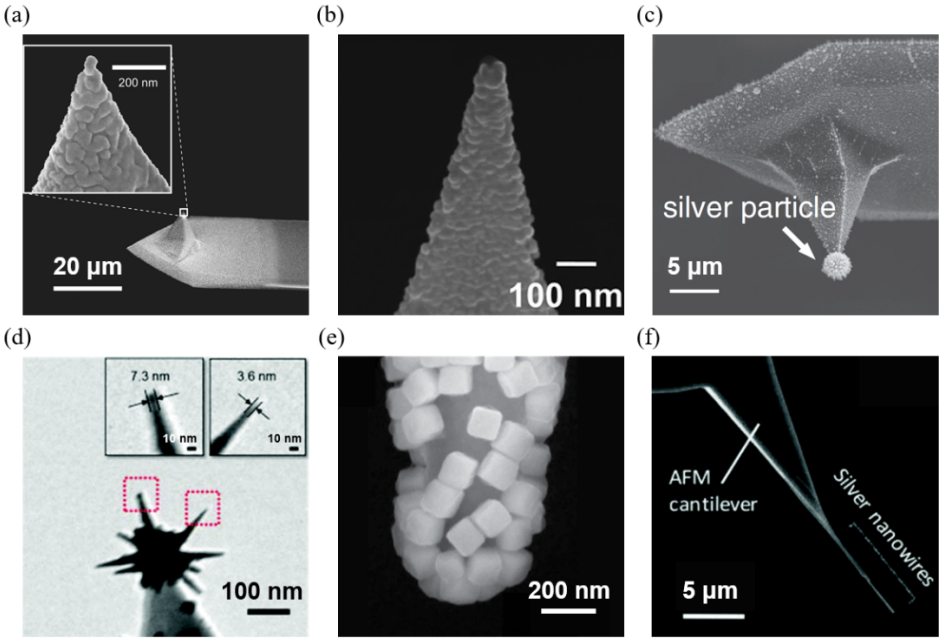

Figure 1-24. (a) SEM image of a TERS probe fabricated by Ag evaporating on an AFM silicon cantilever [adapted from[133]]; (b) SEM image of Au-coated tips prepared by pulsed electrodeposition [adapted from[137]]; (c) SEM image of a TERS probe after photoreduction with a silver nanoparticle selectively fabricated at the tip apex [adapted from[138]]; (d) TEM image of Au nanostar bonded TERS probe [adapted from[139]] (e) SEM image of an Ag nanocube coated TERS probe [adapted from[140]]; (f) SEM image of an AgNW functionalized AFM-TERS probe. [adapted from[141]]

STM-TERS: for the STM-based TERS, commonly the electrochemical (EC) etching method is used in the tip fabrication, during which processes, the metal (Au/Ag) wire acts as a dissolution anode with the etching occurs near the air-liquid interface, forming a neck until it becomes thin enough that cannot support the immersed part, and consequently drops off.[142] Fig. 1-25a shows the typical SEM image of the STM-TERS tip.[143] The morphology of the tip, such as the radius of curvature, shape, size, and geometry, could be controlled by the etching parameters such as the voltage, cut-off current, etchant, temperature, and et al., which strongly dominates the field enhancement and spatial resolution of the tip.[144] Besides, there are some specialized STM-TERS tips fabrication methods, such as the focused-ion-beam (FIB) milling method to fabricate gratings on the tip shaft to excite and propagate the surface plasmon polaritons (SPPs) to the tip apex through the coupling effect of the grating under laser illumination, as shown in Fig. 1-25b.[145]

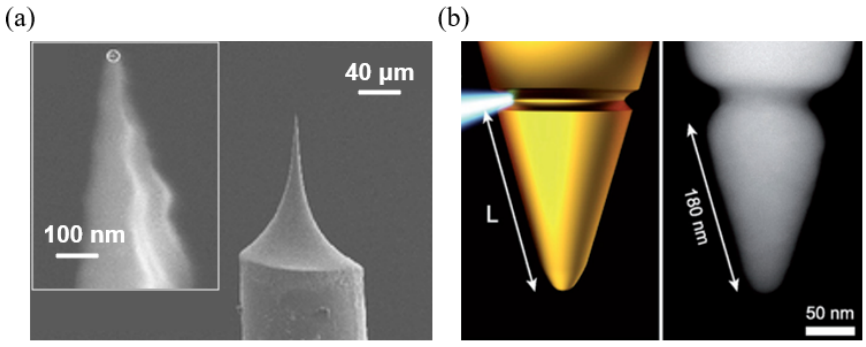

Figure 1-25. (a) SEM images of electrochemically etched Ag probe; [adapted from[143]] (b) Schematic illustration and STEM-HAADF image of a gold tip with a FIB milled groove. [adapted from[145]]

SFM-TERS: for the SFM-based TERS, generally no restriction on the tip, which is attached to the tuning fork for shear force feedback. Consequently, the tip fabrication methods applied in other SPM-TERS techniques could be applied in the SFM-TERS tip fabrication. Commonly, the etched Ag or Au tips[146, 147] and Au/Ag coated etched tungsten (W) tips[148] are glued onto the tuning fork as the SFM-TERS tips, in which cases the weight of the glued tip affects the frequency and quality factor of the tuning fork.

1.3 Problem statement and research objectives

1.3.1 Problem statement

With the advantages of being more stable, faster, and having no intrinsic substrate limitations,[141] as mentioned in section 1.2.4, AFM-TERS is widely used. In a TERS system, the TERS active tip is the most crucial part, and the vacuum-evaporation of noble metal on the AFM cantilever is commonly used in fabricating AFM-TERS probes due to its large-scale fabrications nature.[95, 149] However, it suffers from several issues:

Firstly, for the metal intrinsic issue, Ag/Au/Cu/Al are regarded as TERS active metals, amongst which Ag shows the highest plasmonic activity under the normally used wavelength region, as mentioned in section 1.2.4.3. However, since the high reactivity and low stability of Ag, it can easily react with the compounds consisting of oxygen and sulfur in the ambient to form Ag_2O/Ag_2SO_3/Ag_2SO_4, resulting in the degradation of the surface plasmon resonance, thus, limiting the lifetime of Ag tips to several hours to few days.[150, 151]

Secondly, for the mechanical degradation issue, the coating metal layer on the AFM-TERS tips could be worn out during the scanning, which results from the intrinsic weak adherence between the metal and the AFM cantilever material,[152] and consequently, causes the degradation of the TERS activity.[153]

Thirdly, for the reproductivity issue, since the deposition procedure could be affected by factors such as temperature, pressure and et al., even slight fluctuation could cause the difference of crystal, thus, fabricating completely same morphology of the coated apex is impossible, resulting in the poor reproducibility.

To address the mechanics and reproducibility issues, silver nanowire (AgNW)-based AFM-TERS probes were proposed in our previous work.[141] Thanks to the high homogeneity of the easy bottom-up large-scale AgNW synthesis, a well-controlled apex morphology, and outstanding optical coupling property can be obtained, which give rise to high TERS reproducibility and activity.

However, the use of silver as a plasmonically active material could not avoid the intrinsic chemical degradation issue, limiting the lifetime of AgNW-based TERS probes. Besides, the

AC-dielectrophoresis (AC-DEP)-based AFM-TERS probe fabrication method exhibits very low controllability of the length of the attached AgNW. Indeed, by using AC-DEP, the attachment of AgNW(s) on the AFM cantilever is completely random, generating various lengths between 2 μm and 20 μm. Whereas, less than 5 μm of the protruded length of the attached AgNW is required to maintain stable TERS measurement. Consequently, the attachment of AgNW usually needs to be repeated until a suitable protruded length is achieved. Additionally, the pristine AgNW previously used could reach a reasonably high enhancement factor (EF), up to the order of 10^5, and a spatial resolution of ~10 nm. Nevertheless, higher EF is always desired for sensitive target samples, and a higher spatial resolution would offer a deeper understanding of the samples' nanoscale nature. Moreover, the current TERS technique is mainly realized by the so-called 'gap mode', which requires to use metal substrate. To broaden the application of TERS, developing the 'non-gap mode' is promising. However, realizing the 'non-gap mode' is a technical barrier for most of the common TERS systems.

1.3.2 Research objectives

As the foregoing discussion, the AgNW-based TERS probe could avoid the low mechanical strength, low reproducibility, and high-cost issues but still suffers the short lifetime due to the intrinsic nature of Ag and the uncontrollability of the protruded length due to the mechanism of the AC-DEP fabrication method. Besides, a higher EF is desired in order to broaden the range of the applicable target samples.

In this case, gold (Au) is considered to be induced into the probe fabrication system. Currently, Au nanomaterials have been widely used in various fields such as chemistry, biology, and medicine due to their excellent physicochemical properties, such as their easy modifiability by molecules, high chemical stability, and non-biotoxicity.[154] As mentioned in section 1.2.4.3, Au is also a candidate metal to be applied as Raman enhancing component. Specifically, the LSPRs are also affected by the size and shape, and stronger electric field enhancement is mainly located at the edges,[132] which can be regarded as Raman enhancing hotspot, as shown in Fig. 1-22b, and for the dielectric function, Au possesses high imaginary part in the low wavelength region, as shown in Fig. 1-21, resulting in high optical losses. Therefore, Au nanomaterials are commonly used as Raman-enhancing component under the 633 nm or 785 nm laser excitation. However, the Raman enhancement of Au is commonly regarded as lower than that of Ag,[155] and Au could generate more heat under laser irradiation and enhanced LSPRs in the confined

area, which could also cause probe degradation.[156-158] Consequently, combining Ag with Au is a promising study direction. In the SERS field, previous researches report that coating a thin Au layer to the Ag nanomaterials would achieve high Raman enhancement, excellent chemical stability, and biocompatibility.[159, 160] Therefore, in the TERS field, Au-coated Ag structures could be applied as TERS probe to improve the performance. Here are the two main objectives of the Ph.D. work:

(1) Developing long-lifetime AgNW-based TERS probe

To solve the aforementioned lifetime issue, we would like to introduce Au-coated AgNW (Ag@Au NW) as a highly sensitive, long-life TERS active antenna. The synthesis of Ag@Au NWs is based on Au atoms conformal deposition method[161] on the surface of AgNW synthesized by polyol method.[162, 163] By evaluating the TERS performance of the Ag@Au NWs with different Au/Ag ratios and comparing with the pristine AgNW and Au-etched AgNW in terms of enhancement factor (EF) and lifetime, we aim to figure out the optimum condition to maintain high EF with long lifetime.

(2) Developing advanced TERS probe fabrication method to achieve protruded length-control and high EF

To mainly solve the protruded length controlling issue, we aim to develop a simple fabrication method using electro-cutting of AgNW at air-liquid interface followed by Au-coating is proposed, which provides to achieve (i) great controllability of protruded AgNW length, (ii) an outstanding EF, and (iii) a better spatial resolution.

1.4 References

(1) Bai, C. Nanoscience and Nanotechnology. *Outlook* **1994**, (34), 28-29.

(2) Jia, Y. Nanotechnology will promote the revolution of cutting-edge technology. *Materials China* **2016**, (10), 3.

(3) Mansoori, G. A.; Soelaiman, T. F. *Nanotechnology--An introduction for the standards community*; ASTM International, 2005.

(4) Barber, D. J.; Freestone, I. C. J. A. An investigation of the origin of the colour of the Lycurgus Cup by analytical transmission electron microscopy. **1990**, *32* (1), 33-45.

(5) Freestone, I.; Meeks, N.; Sax, M.; Higgitt, C. J. G. b. The Lycurgus cup—a roman nanotechnology. **2007**, *40* (4), 270-277.

(6) Wagner, F.; Haslbeck, S.; Stievano, L.; Calogero, S.; Pankhurst, Q.; Martinek, K.-P. Before striking gold in gold-ruby glass. *Nature* **2000**, *407* (6805), 691-692.

(7) Museum, T. B. *The Lycurgus Cup*. https://www.britishmuseum.org/collection/object/H_1958-1202-1 (accessed 2022 20th October).

(8) Faraday, M. The Bakerian Lecture: Experimental relations of gold (and other metals) to light. *Philosophical transactions of the Royal Society of London* **1857**, (147), 145-181.

(9) Feynman, R. P. There's Plenty of Room at the Bottom. *Engineering and Science* **1960**, *23* (5), 22-36.

(10) Taniguchi, N. On the basic concept of nanotechnology. In *International Conference on Production Engineering*, Tokyo, 1974; pp 18-23.

(11) Drexler, K. E. *Engines of Creation: The Coming Era of Nanotechnology*; Anchor, 1987.

(12) Ruska, E. The development of the electron microscope and of electron microscopy (Nobel Lecture). *Angewandte Chemie International Edition in English* **1987**, *26* (7), 595-605.

(13) Binnig, G.; Rohrer, H.; Gerber, C.; Weibel, E. Surface Studies by Scanning Tunneling Microscopy. *Physical Review Letters* **1982**, *49* (1), 57-61. DOI: 10.1103/PhysRevLett.49.57.

(14) Binnig, G.; Quate, C. F.; Gerber, C. Atomic Force Microscope. *Physical Review Letters* **1986**, *56* (9), 930-933. DOI: 10.1103/PhysRevLett.56.930.

(15) Tseng, A. A.; Notargiacomo, A.; Chen, T. P. Nanofabrication by scanning probe microscope lithography: A review. *Journal of Vacuum Science & Technology B:*

Microelectronics and Nanometer Structures Processing, Measurement, and Phenomena **2005**, *23* (3), 877-894. DOI: 10.1116/1.1926293 (acccessed 2022/10/20).

(16) Eigler, D. M.; Schweizer, E. K. Positioning single atoms with a scanning tunnelling microscope. *Nature* **1990**, *344* (6266), 524-526. DOI: 10.1038/344524a0.

(17) Bayda, S.; Adeel, M.; Tuccinardi, T.; Cordani, M.; Rizzolio, F. The History of Nanoscience and Nanotechnology: From Chemical–Physical Applications to Nanomedicine. In *Molecules*, 2020; Vol. 25.

(18) Schaller, R. R. Moore's law: past, present and future. *IEEE spectrum* **1997**, *34* (6), 52-59.

(19) Newsroom, S. *Samsung Begins Chip Production Using 3nm Process Technology With GAA Architecture*. 2022. https://news.samsung.com/global/samsung-begins-chip-production-using-3nm-process-technology-with-gaa-architecture (accessed 2022 24th October).

(20) Somwanshi, S. B.; Somvanshi, S. B.; Kharat, P. B. Nanocatalyst: A Brief Review on Synthesis to Applications. *Journal of Physics: Conference Series* **2020**, *1644* (1), 012046. DOI: 10.1088/1742-6596/1644/1/012046.

(21) Ediriwickrema, A.; Saltzman, W. M. Nanotherapy for Cancer: Targeting and Multifunctionality in the Future of Cancer Therapies. *ACS Biomaterials Science & Engineering* **2015**, *1* (2), 64-78. DOI: 10.1021/ab500084g.

(22) Yan, R.; Zhang, Y.; Li, Y.; Xia, L.; Guo, Y.; Zhou, Q. Structural basis for the recognition of SARS-CoV-2 by full-length human ACE2. *Science* **2020**, *367* (6485), 1444-1448. DOI: 10.1126/science.abb2762 (acccessed 2022/10/23).

(23) Wang, Q.; Zhang, Y.; Wu, L.; Niu, S.; Song, C.; Zhang, Z.; Lu, G.; Qiao, C.; Hu, Y.; Yuen, K.-Y.; et al. Structural and Functional Basis of SARS-CoV-2 Entry by Using Human ACE2. *Cell* **2020**, *181* (4), 894-904.e899. DOI: https://doi.org/10.1016/j.cell.2020.03.045.

(24) Suman; Sharma, P.; Goyal, P. Evolution of PV technology from conventional to nano-materials. *Materials Today: Proceedings* **2020**, *28*, 1593-1597. DOI: https://doi.org/10.1016/j.matpr.2020.04.846.

(25) Soliman, A. S.; Zhu, S.; Xu, L.; Dong, J.; Cheng, P. Efficient waste heat recovery system for diesel engines using nano-enhanced phase change materials. *Case Studies in Thermal Engineering* **2021**, *28*, 101390. DOI: https://doi.org/10.1016/j.csite.2021.101390.

(26) Zhao, W.; Choi, W.; Yoon, W.-S. Nanostructured Electrode Materials for Rechargeable Lithium-Ion Batteries. *J. Electrochem. Sci. Technol* **2020**, *11* (3), 195-219. DOI: 10.33961/jecst.2020.00745.

(27) Yunus, I. S.; Harwin; Kurniawan, A.; Adityawarman, D.; Indarto, A. Nanotechnologies in water and air pollution treatment. *Environmental Technology Reviews* **2012**, *1* (1), 136-148. DOI: 10.1080/21622515.2012.733966.

(28) Nagar, A.; Pradeep, T. Clean Water through Nanotechnology: Needs, Gaps, and Fulfillment. *ACS Nano* **2020**, *14* (6), 6420-6435. DOI: 10.1021/acsnano.9b01730.

(29) Cao, J.-j.; Huang, Y.; Zhang, Q. Ambient Air Purification by Nanotechnologies: From Theory to Application. In *Catalysts*, 2021; Vol. 11.

(30) Nakamoto, M.; Moon, J. Stable and environment-hard vacuum nanoelectronic devices for aerospace applications. *IOP Conference Series: Materials Science and Engineering* **2019**, *474* (1), 012005. DOI: 10.1088/1757-899X/474/1/012005.

(31) Arepalli, S.; Moloney, P. Engineered nanomaterials in aerospace. *MRS Bulletin* **2015**, *40* (10), 804-811. DOI: 10.1557/mrs.2015.231 From Cambridge University Press Cambridge Core.

(32) Borodianskiy, K.; Zinigrad, M. Nanomaterials Applications in Modern Metallurgical Processes. *Diffusion Foundations* **2016**, *9*, 30-41. DOI: 10.4028/www.scientific.net/DF.9.30.

(33) Korada, V. S.; Hamid, N. H. B. Engineering Applications of Nanotechnology. Springer: 2017.

(34) Samak, D. H.; El-Sayed, Y. S.; Shaheen, H. M.; El-Far, A. H.; Abd El-Hack, M. E.; Noreldin, A. E.; El-Naggar, K.; Abdelnour, S. A.; Saied, E. M.; El-Seedi, H. R.; et al. Developmental toxicity of carbon nanoparticles during embryogenesis in chicken. *Environmental Science and Pollution Research* **2020**, *27* (16), 19058-19072. DOI: 10.1007/s11356-018-3675-6.

(35) Mohamed, E. F. Nanotechnology: future of environmental air pollution control. *Environmental Management Sustainable Development* **2017**, *6* (2), 429-454.

(36) Region, C. f. F. S. o. T. G. o. t. H. K. S. A. *Nanotechnology and Food Safety*. 2010. https://www.cfs.gov.hk/english/programme/programme_rafs/programme_rafs_ft_01_04_Nanotechnology.html (accessed 2022 24th October).

(37) Kroto, H. W.; Heath, J. R.; O'Brien, S. C.; Curl, R. F.; Smalley, R. E. C60: Buckminsterfullerene. *Nature* **1985**, *318* (6042), 162-163. DOI: 10.1038/318162a0.

(38) Baptista, F. R.; Belhout, S. A.; Giordani, S.; Quinn, S. J. Recent developments in carbon nanomaterial sensors. *Chemical Society Reviews* **2015**, *44* (13), 4433-4453, 10.1039/C4CS00379A. DOI: 10.1039/C4CS00379A.

(39) Iijima, S. Helical microtubules of graphitic carbon. *Nature* **1991**, *354* (6348), 56-58. DOI: 10.1038/354056a0.

(40) Buongiorno Nardelli, M.; Yakobson, B. I.; Bernholc, J. Mechanism of strain release in carbon nanotubes. *Physical Review B* **1998**, *57* (8), R4277-R4280. DOI: 10.1103/PhysRevB.57.R4277.

(41) Cumings, J.; Zettl, A. Low-Friction Nanoscale Linear Bearing Realized from Multiwall Carbon Nanotubes. *Science* **2000**, *289* (5479), 602-604. DOI: 10.1126/science.289.5479.602 (acccessed 2022/10/25).

(42) Ruoff, R. S.; Lorents, D. C. Mechanical and thermal properties of carbon nanotubes. *Carbon* **1995**, *33* (7), 925-930. DOI: https://doi.org/10.1016/0008-6223(95)00021-5.

(43) Biercuk, M. J.; Llaguno, M. C.; Radosavljevic, M.; Hyun, J. K.; Johnson, A. T.; Fischer, J. E. Carbon nanotube composites for thermal management. *Applied Physics Letters* **2002**, *80* (15), 2767-2769. DOI: 10.1063/1.1469696 (acccessed 2022/10/25).

(44) Hone, J.; Llaguno, M. C.; Biercuk, M. J.; Johnson, A. T.; Batlogg, B.; Benes, Z.; Fischer, J. E. Thermal properties of carbon nanotubes and nanotube-based materials. *Applied Physics A* **2002**, *74* (3), 339-343. DOI: 10.1007/s003390201277.

(45) Ebbesen, T. W.; Lezec, H. J.; Hiura, H.; Bennett, J. W.; Ghaemi, H. F.; Thio, T. Electrical conductivity of individual carbon nanotubes. *Nature* **1996**, *382* (6586), 54-56. DOI: 10.1038/382054a0.

(46) Tans, S. J.; Verschueren, A. R. M.; Dekker, C. Room-temperature transistor based on a single carbon nanotube. *Nature* **1998**, *393* (6680), 49-52. DOI: 10.1038/29954.

(47) Sandler, J. K. W.; Kirk, J. E.; Kinloch, I. A.; Shaffer, M. S. P.; Windle, A. H. Ultra-low electrical percolation threshold in carbon-nanotube-epoxy composites. *Polymer* **2003**, *44* (19), 5893-5899. DOI: https://doi.org/10.1016/S0032-3861(03)00539-1.

(48) Gooding, J. J. Nanostructuring electrodes with carbon nanotubes: A review on electrochemistry and applications for sensing. *Electrochimica Acta* **2005**, *50* (15), 3049-3060. DOI: https://doi.org/10.1016/j.electacta.2004.08.052.

(49) Trojanowicz, M. Analytical applications of carbon nanotubes: a review. *TrAC Trends in Analytical Chemistry* **2006**, *25* (5), 480-489. DOI: https://doi.org/10.1016/j.trac.2005.11.008.

(50) Peierls, R. Quelques propriétés typiques des corps solides. *Annales de l'institut Henri Poincaré* **1935**, *5* (3), 177-222.

(51) Landau, L. D. Zur Theorie der phasenumwandlungen II. *Phys. Z. Sowjetunion* **1937**, *11* (545), 26-35.

(52) Novoselov, K. S.; Geim, A. K.; Morozov, S. V.; Jiang, D.; Zhang, Y.; Dubonos, S. V.; Grigorieva, I. V.; Firsov, A. A. Electric Field Effect in Atomically Thin Carbon Films. *Science* **2004**, *306* (5696), 666-669. DOI: 10.1126/science.1102896 (acccessed 2022/10/25).

(53) Novoselov, K. S.; Fal′ko, V. I.; Colombo, L.; Gellert, P. R.; Schwab, M. G.; Kim, K. A roadmap for graphene. *Nature* **2012**, *490* (7419), 192-200. DOI: 10.1038/nature11458.

(54) Geim, A. K. Graphene: Status and Prospects. *Science* **2009**, *324* (5934), 1530-1534. DOI: 10.1126/science.1158877 (acccessed 2022/10/25).

(55) Ferrari, A. C.; Bonaccorso, F.; Fal'ko, V.; Novoselov, K. S.; Roche, S.; Bøggild, P.; Borini, S.; Koppens, F. H. L.; Palermo, V.; Pugno, N.; et al. Science and technology roadmap for graphene, related two-dimensional crystals, and hybrid systems. *Nanoscale* **2015**, *7* (11), 4598-4810, 10.1039/C4NR01600A. DOI: 10.1039/C4NR01600A.

(56) Paul, R.; Vincent, M.; Etacheri, V.; Roy, A. K. Chapter 1 - Carbon nanotubes, graphene, porous carbon, and hybrid carbon-based materials: synthesis, properties, and functionalization for efficient energy storage. In *Carbon Based Nanomaterials for Advanced Thermal and Electrochemical Energy Storage and Conversion*, Paul, R., Etacheri, V., Wang, Y., Lin, C.-T. Eds.; Elsevier, 2019; pp 1-24.

(57) Xu, W.; Mao, N.; Zhang, J. Graphene: A Platform for Surface-Enhanced Raman Spectroscopy. *Small* **2013**, *9* (8), 1206-1224, https://doi.org/10.1002/smll.201203097. DOI: https://doi.org/10.1002/smll.201203097 (acccessed 2022/12/16).

(58) Jorio, A.; Saito, R.; Dresselhaus, G.; Dresselhaus, M. S. Determination of nanotubes properties by Raman spectroscopy. *Philosophical Transactions of the Royal Society of London. Series A: Mathematical, Physical and Engineering Sciences* **2004**, *362* (1824), 2311-2336. DOI: 10.1098/rsta.2004.1443 (acccessed 2022/12/16).

(59) Smekal, A. Zur Quantentheorie der Dispersion. *Die Naturwissenschaften* **1923**, *11* (43), 873-875. DOI: 10.1007/bf01576902.

(60) Raman, C. V.; Krishnan, K. S. A New Type of Secondary Radiation. *Nature* **1928**, *121* (3048), 501-502. DOI: 10.1038/121501c0.

(61) Young, A. T. Rayleigh scattering. *Appl. Opt.* **1981**, *20* (4), 533-535. DOI: 10.1364/AO.20.000533.

(62) Weber, W. H.; Merlin, R. *Raman scattering in materials science*; Springer Science & Business Media, 2000.

(63) Kumar, S.; Kumar, P.; Das, A.; Pathak, C. S. Surface-Enhanced Raman Scattering: Introduction and Applications. In *Recent Advances in Nanophotonics-Fundamentals and Applications*, IntechOpen London, UK, 2020; pp 1-24.

(64) Classical Theory of Rayleigh and Raman Scattering. In *The Raman Effect*, 2002; pp 31-48.

(65) Procházka, M. J. B.; medical physics, b. e. Surface-enhanced raman spectroscopy. **2016**.

(66) Ornstein, L. S.; Rekveld, J.; Utrecht. Intensity Measurements in the Raman Effect and the Distribution Law of Maxwell-Boltzmann. *Physical Review* **1929**, *34* (5), 720-725. DOI: 10.1103/PhysRev.34.720.

(67) Mosca, S.; Conti, C.; Stone, N.; Matousek, P. Spatially offset Raman spectroscopy. *Nature Reviews Methods Primers* **2021**, *1* (1), 21. DOI: 10.1038/s43586-021-00019-0.

(68) Shipp, D. W.; Sinjab, F.; Notingher, I. Raman spectroscopy: techniques and applications in the life sciences. *Adv. Opt. Photon.* **2017**, *9* (2), 315-428. DOI: 10.1364/aop.9.000315.

(69) Hackshaw, K. V.; Miller, J. S.; Aykas, D. P.; Rodriguez-Saona, L. Vibrational Spectroscopy for Identification of Metabolites in Biologic Samples. **2020**, *25* (20), 4725.

(70) Fleischmann, M.; Hendra, P. J.; McQuillan, A. J. Raman spectra of pyridine adsorbed at a silver electrode. *Chemical Physics Letters* **1974**, *26* (2), 163-166. DOI: https://doi.org/10.1016/0009-2614(74)85388-1.

(71) Jeanmaire, D. L.; Van Duyne, R. P. Surface raman spectroelectrochemistry. *Journal of Electroanalytical Chemistry and Interfacial Electrochemistry* **1977**, *84* (1), 1-20. DOI: 10.1016/s0022-0728(77)80224-6.

(72) Albrecht, M. G.; Creighton, J. A. Anomalously intense Raman spectra of pyridine at a silver electrode. *J. Am. Chem. Soc.* **2002**, *99* (15), 5215-5217. DOI: 10.1021/ja00457a071.

(73) Zong, C.; Xu, M.; Xu, L. J.; Wei, T.; Ma, X.; Zheng, X. S.; Hu, R.; Ren, B. Surface-Enhanced Raman Spectroscopy for Bioanalysis: Reliability and Challenges. *Chem. Rev.* **2018**, *118* (10), 4946-4980. DOI: 10.1021/acs.chemrev.7b00668.

(74) Kawata, S.; Shalaev, V. M. *Tip enhancement*; Elsevier, 2011.

(75) Xia, L.; Chen, M.; Zhao, X.; Zhang, Z.; Xia, J.; Xu, H.; Sun, M. Visualized method of chemical enhancement mechanism on SERS and TERS. *Journal of Raman Spectroscopy* **2014**, *45* (7), 533-540, https://doi.org/10.1002/jrs.4504. DOI: https://doi.org/10.1002/jrs.4504 (acccessed 2022/10/26).

(76) Ding, S.-Y.; Zhang, X.-M.; Ren, B.; Tian, Z.-Q. Surface-Enhanced Raman Spectroscopy (SERS): General Introduction. In *Encyclopedia of Analytical Chemistry*, 2014; pp 1-34.

(77) Luo, S.-C.; Sivashanmugan, K.; Liao, J.-D.; Yao, C.-K.; Peng, H.-C. Nanofabricated SERS-active substrates for single-molecule to virus detection in vitro: A review. *Biosensors and Bioelectronics* **2014**, *61*, 232-240. DOI: https://doi.org/10.1016/j.bios.2014.05.013.

(78) Stöckle, R. M.; Suh, Y. D.; Deckert, V.; Zenobi, R. Nanoscale chemical analysis by tip-enhanced Raman spectroscopy. *Chemical Physics Letters* **2000**, *318* (1), 131-136. DOI: https://doi.org/10.1016/S0009-2614(99)01451-7.

(79) Pettinger, B.; Ren, B.; Picardi, G.; Schuster, R.; Ertl, G. Nanoscale Probing of Adsorbed Species by Tip-Enhanced Raman Spectroscopy. *Physical Review Letters* **2004**, *92* (9), 096101. DOI: 10.1103/PhysRevLett.92.096101.

(80) Sun, M.; Fang, Y.; Yang, Z.; Xu, H. Chemical and electromagnetic mechanisms of tip-enhanced Raman scattering. *Physical Chemistry Chemical Physics* **2009**, *11* (41), 9412-9419, 10.1039/B909006A. DOI: 10.1039/B909006A.

(81) Hayazawa, N.; Inouye, Y.; Sekkat, Z.; Kawata, S. Metallized tip amplification of near-field Raman scattering. *Optics Communications* **2000**, *183* (1), 333-336. DOI: https://doi.org/10.1016/S0030-4018(00)00894-4.

(82) Anderson, M. S. Locally enhanced Raman spectroscopy with an atomic force microscope. *Applied Physics Letters* **2000**, *76* (21), 3130-3132. DOI: 10.1063/1.126546 (acccessed 2022/10/27).

(83) Wessel, J. Surface-enhanced optical microscopy. *J. Opt. Soc. Am. B* **1985**, *2* (9), 1538-1541. DOI: 10.1364/JOSAB.2.001538.

(84) Inouye, Y.; Kawata, S. Near-field scanning optical microscope with a metallic probe tip. *Opt. Lett.* **1994**, *19* (3), 159-161. DOI: 10.1364/OL.19.000159.

(85) Zrimsek, A. B.; Chiang, N.; Mattei, M.; Zaleski, S.; McAnally, M. O.; Chapman, C. T.; Henry, A.-I.; Schatz, G. C.; Van Duyne, R. P. Single-Molecule Chemistry with Surface- and Tip-Enhanced Raman Spectroscopy. *Chemical Reviews* **2017**, *117* (11), 7583-7613. DOI: 10.1021/acs.chemrev.6b00552.

(86) Shi, X.; Coca-López, N.; Janik, J.; Hartschuh, A. Advances in Tip-Enhanced Near-Field Raman Microscopy Using Nanoantennas. *Chemical Reviews* **2017**, *117* (7), 4945-4960. DOI: 10.1021/acs.chemrev.6b00640.

(87) Kumar, N.; Weckhuysen, B. M.; Wain, A. J.; Pollard, A. J. Nanoscale chemical imaging using tip-enhanced Raman spectroscopy. *Nature Protocols* **2019**, *14* (4), 1169-1193. DOI: 10.1038/s41596-019-0132-z.

(88) Wei, H.; Xu, H. Hot spots in different metal nanostructures for plasmon-enhanced Raman spectroscopy. *Nanoscale* **2013**, *5* (22), 10794-10805, 10.1039/C3NR02924G. DOI: 10.1039/C3NR02924G.

(89) Cao, E.; Lin, W.; Sun, M.; Liang, W.; Song, Y. Exciton-plasmon coupling interactions: from principle to applications. *Nanophotonics* **2018**, *7* (1), 145-167. DOI: 10.1515/nanoph-2017-0059.

(90) Li, M.; Cushing, S. K.; Wu, N. Plasmon-enhanced optical sensors: a review. *Analyst* **2015**, *140* (2), 386-406, 10.1039/C4AN01079E. DOI: 10.1039/c4an01079e.

(91) Das, G.; Coluccio, M. L.; Alrasheed, S.; Giugni, A.; Allione, M.; Torre, B.; Perozziello, G.; Candeloro, P.; Di Fabrizio, E. Plasmonic nanostructures for the ultrasensitive detection of biomolecules. *La Rivista del Nuovo Cimento* **2016**, *39* (11), 547-586. DOI: 10.1393/ncr/i2016-10129-y.

(92) Jones, M. R.; Osberg, K. D.; Macfarlane, R. J.; Langille, M. R.; Mirkin, C. A. Templated techniques for the synthesis and assembly of plasmonic nanostructures. *Chem. Rev.* **2011**, *111* (6), 3736-3827. DOI: 10.1021/cr1004452.

(93) Petryayeva, E.; Krull, U. J. Localized surface plasmon resonance: nanostructures, bioassays and biosensing--a review. *Anal. Chim. Acta* **2011**, *706* (1), 8-24. DOI: 10.1016/j.aca.2011.08.020.

(94) Willets, K. A.; Van Duyne, R. P. Localized surface plasmon resonance spectroscopy and sensing. *Annu. Rev. Phys. Chem.* **2007**, *58*, 267-297. DOI: 10.1146/annurev.physchem.58.032806.104607.

(95) Asghari-Khiavi, M.; Wood, B. R.; Hojati-Talemi, P.; Downes, A.; McNaughton, D.; Mechler, A. Exploring the origin of tip-enhanced Raman scattering; preparation of efficient TERS probes with high yield. *Journal of Raman Spectroscopy* **2012**, *43* (2), 173-180, https://doi.org/10.1002/jrs.3021. DOI: https://doi.org/10.1002/jrs.3021 (acccessed 2021/06/23).

(96) Zhang, W.; Cui, X.; Martin, O. J. F. Local field enhancement of an infinite conical metal tip illuminated by a focused beam. *Journal of Raman Spectroscopy* **2009**, *40* (10), 1338-1342, https://doi.org/10.1002/jrs.2439. DOI: https://doi.org/10.1002/jrs.2439 (acccessed 2022/11/06).

(97) Hartschuh, A. Tip-Enhanced Near-Field Optical Microscopy. *Angewandte Chemie International Edition* **2008**, *47* (43), 8178-8191, https://doi.org/10.1002/anie.200801605. DOI: https://doi.org/10.1002/anie.200801605 (acccessed 2022/11/06).

(98) Kawata, S.; Ichimura, T.; Taguchi, A.; Kumamoto, Y. Nano-Raman Scattering Microscopy: Resolution and Enhancement. *Chemical Reviews* **2017**, *117* (7), 4983-5001. DOI: 10.1021/acs.chemrev.6b00560.

(99) Taguchi, A. Plasmonic tip for nano Raman microcopy: structures, materials, and enhancement. *Optical Review* **2017**, *24* (3), 462-469. DOI: 10.1007/s10043-017-0317-z.

(100) Pilot, R.; Signorini, R.; Durante, C.; Orian, L.; Bhamidipati, M.; Fabris, L. A Review on Surface-Enhanced Raman Scattering. *Biosensors (Basel)* **2019**, *9* (2). DOI: 10.3390/bios9020057.

(101) Chowdhury, J. How the Charge Transfer (CT) Contributions Influence the SERS Spectra of Molecules? A Retrospective from the View of Albrecht's "A" and Herzberg-Teller Contributions. *Appl. Spectrosc. Rev.* **2014**, *50* (3), 240-260. DOI: 10.1080/05704928.2014.942815.

(102) Lombardi, J. R.; Birke, R. L. A Unified Approach to Surface-Enhanced Raman Spectroscopy. *The Journal of Physical Chemistry C* **2008**, *112* (14), 5605-5617. DOI: 10.1021/jp800167v.

(103) Lombardi, J. R.; Birke, R. L.; Lu, T.; Xu, J. Charge-transfer theory of surface enhanced Raman spectroscopy: Herzberg–Teller contributions. *The Journal of Chemical Physics* **1986**, *84* (8), 4174-4180. DOI: 10.1063/1.450037.

(104) Shao, F.; Zenobi, R. Tip-enhanced Raman spectroscopy: principles, practice, and applications to nanospectroscopic imaging of 2D materials. *Analytical and Bioanalytical Chemistry* **2019**, *411* (1), 37-61. DOI: 10.1007/s00216-018-1392-0.

(105) HORIBA. *What kind of substrates can be probed with TERS?* https://www.horiba.com/gbr/scientific/technologies/afm-raman/what-kind-of-substrates-can-be-probed-with-ters/ (accessed 2022 9th November).

(106) Stadler, J.; Oswald, B.; Schmid, T.; Zenobi, R. Characterizing unusual metal substrates for gap-mode tip-enhanced Raman spectroscopy. *Journal of Raman Spectroscopy* **2013**, *44* (2), 227-233, https://doi.org/10.1002/jrs.4169. DOI: https://doi.org/10.1002/jrs.4169 (acccessed 2022/11/08).

(107) Yang, Z.; Aizpurua, J.; Xu, H. Electromagnetic field enhancement in TERS configurations. *Journal of Raman Spectroscopy* **2009**, *40* (10), 1343-1348, https://doi.org/10.1002/jrs.2429. DOI: https://doi.org/10.1002/jrs.2429 (acccessed 2022/11/08).

(108) Pozzi, E. A.; Goubert, G.; Chiang, N.; Jiang, N.; Chapman, C. T.; McAnally, M. O.; Henry, A.-I.; Seideman, T.; Schatz, G. C.; Hersam, M. C.; et al. Ultrahigh-Vacuum Tip-Enhanced Raman Spectroscopy. *Chemical Reviews* **2017**, *117* (7), 4961-4982. DOI: 10.1021/acs.chemrev.6b00343.

(109) Meyer, R.; Yao, X.; Deckert, V. Latest instrumental developments and bioanalytical applications in tip-enhanced Raman spectroscopy. *TrAC Trends in Analytical Chemistry* **2018**, *102*, 250-258. DOI: https://doi.org/10.1016/j.trac.2018.02.012.

(110) Stadler, J.; Schmid, T.; Zenobi, R. Nanoscale Chemical Imaging Using Top-Illumination Tip-Enhanced Raman Spectroscopy. *Nano Letters* **2010**, *10* (11), 4514-4520. DOI: 10.1021/nl102423m.

(111) Wang, H.; Chu, P. K. Chapter 4 - Surface Characterization of Biomaterials. In *Characterization of Biomaterials*, Bandyopadhyay, A., Bose, S. Eds.; Academic Press, 2013; pp 105-174.

(112) Hölscher, H. AFM, Non-contact Mode. In *Encyclopedia of Nanotechnology*, Bhushan, B. Ed.; Springer Netherlands, 2012; pp 93-99.

(113) Ichimura, T.; Fujii, S.; Verma, P.; Yano, T.; Inouye, Y.; Kawata, S. Subnanometric Near-Field Raman Investigation in the Vicinity of a Metallic Nanostructure. *Physical Review Letters* **2009**, *102* (18), 186101. DOI: 10.1103/PhysRevLett.102.186101.

(114) Yu, J.; Saito, Y.; Ichimura, T.; Kawata, S.; Verma, P. Far-field free tapping-mode tip-enhanced Raman microscopy. *Applied Physics Letters* **2013**, *102* (12), 123110. DOI: 10.1063/1.4799496 (acccessed 2022/11/14).

(115) He, Y.; Chen, S.; Yu, Q. Scanning Tunneling Microscope (STM). In *Encyclopedia of Tribology*, Wang, Q. J., Chung, Y.-W. Eds.; Springer US, 2013; pp 2983-2988.

(116) Huang, T.-X.; Huang, S.-C.; Li, M.-H.; Zeng, Z.-C.; Wang, X.; Ren, B. Tip-enhanced Raman spectroscopy: tip-related issues. *Analytical and Bioanalytical Chemistry* **2015**, *407* (27), 8177-8195. DOI: 10.1007/s00216-015-8968-8.

(117) Kasani, S.; Curtin, K.; Wu, N. A review of 2D and 3D plasmonic nanostructure array patterns: fabrication, light management and sensing applications. *Nanophotonics* **2019**, *8* (12), 2065-2089. DOI: 10.1515/nanoph-2019-0158.

(118) Link, S.; El-Sayed, M. A. Size and Temperature Dependence of the Plasmon Absorption of Colloidal Gold Nanoparticles. *The Journal of Physical Chemistry B* **1999**, *103* (21), 4212-4217. DOI: 10.1021/jp984796o.

(119) Nehl, C. L.; Hafner, J. H. Shape-dependent plasmon resonances of gold nanoparticles. *J. Mater. Chem.* **2008**, *18* (21), 2415-2419, 10.1039/B714950F. DOI: 10.1039/b714950f.

(120) Andrade-Neto, A. J. R. B. d. E. d. F. Dielectric function for free electron gas: comparison between Drude and Lindhard models. **2016**, *39*.

(121) Erwin, W. R.; Zarick, H. F.; Talbert, E. M.; Bardhan, R. Light trapping in mesoporous solar cells with plasmonic nanostructures. *Energy & Environmental Science* **2016**, *9* (5), 1577-1601, 10.1039/C5EE03847B. DOI: 10.1039/c5ee03847b.

(122) Hong, S.; Li, X. Optimal Size of Gold Nanoparticles for Surface-Enhanced Raman Spectroscopy under Different Conditions. *Journal of Nanomaterials* **2013**, *2013*, 1-9. DOI: 10.1155/2013/790323.

(123) Taguchi, A.; Hayazawa, N.; Furusawa, K.; Ishitobi, H.; Kawata, S. Deep-UV tip-enhanced Raman scattering. *Journal of Raman Spectroscopy* **2009**, *40* (9), 1324-1330, https://doi.org/10.1002/jrs.2287. DOI: https://doi.org/10.1002/jrs.2287 (acccessed 2022/11/15).

(124) Yang, Z.; Li, Q.; Fang, Y.; Sun, M. Deep ultraviolet tip-enhanced Raman scattering. *Chemical Communications* **2011**, *47* (32), 9131-9133, 10.1039/C1CC13291A. DOI: 10.1039/C1CC13291A.

(125) Richard-Lacroix, M.; Zhang, Y.; Dong, Z.; Deckert, V. Mastering high resolution tip-enhanced Raman spectroscopy: towards a shift of perception. *Chemical Society Reviews* **2017**, *46* (13), 3922-3944, 10.1039/C7CS00203C. DOI: 10.1039/C7CS00203C.

(126) Ko, H.; Singamaneni, S.; Tsukruk, V. V. Nanostructured Surfaces and Assemblies as SERS Media. *Small* **2008**, *4* (10), 1576-1599. DOI: 10.1002/smll.200800337.

(127) Moskovits, M. Surface-enhanced Raman spectroscopy: a brief retrospective. *J. Raman Spectrosc.* **2005**, *36* (6-7), 485-496. DOI: 10.1002/jrs.1362.

(128) Abalde-Cela, S.; Aldeanueva-Potel, P.; Mateo-Mateo, C.; Rodriguez-Lorenzo, L.; Alvarez-Puebla, R. A.; Liz-Marzan, L. M. Surface-enhanced Raman scattering biomedical applications of plasmonic colloidal particles. *J. R. Soc. Interface* **2010**, *7 Suppl 4* (suppl_4), S435-450. DOI: 10.1098/rsif.2010.0125.focus.

(129) Israelsen, N. D.; Hanson, C.; Vargis, E. Nanoparticle properties and synthesis effects on surface-enhanced Raman scattering enhancement factor: an introduction. *ScientificWorldJournal* **2015**, *2015*, 124582. DOI: 10.1155/2015/124582.

(130) Ouyang, L.; Ren, W.; Zhu, L.; Irudayaraj, J. Prosperity to challenges: recent approaches in SERS substrate fabrication. *Rev. Anal. Chem.* **2017**, *36* (1). DOI: 10.1515/revac-2016-0027.

(131) Hao, E.; Schatz, G. C. Electromagnetic fields around silver nanoparticles and dimers. *J. Chem. Phys.* **2004**, *120* (1), 357-366. DOI: 10.1063/1.1629280.

(132) Chatterjee, S.; Ringane, A. B.; Arya, A.; Das, G. M.; Dantham, V. R.; Laha, R.; Hussian, S. A high-yield, one-step synthesis of surfactant-free gold nanostars and numerical study for single-molecule SERS application. *Journal of Nanoparticle Research* **2016**, *18* (8), 242. DOI: 10.1007/s11051-016-3557-0.

(133) Mino, T.; Saito, Y.; Verma, P. Quantitative Analysis of Polarization-Controlled Tip-Enhanced Raman Imaging through the Evaluation of the Tip Dipole. *ACS Nano* **2014**, *8* (10), 10187-10195. DOI: 10.1021/nn5031803.

(134) Golan, Y.; Margulis, L.; Rubinstein, I. Vacuum-deposited gold films: I. Factors affecting the film morphology. *Surface Science* **1992**, *264* (3), 312-326. DOI: https://doi.org/10.1016/0039-6028(92)90188-C.

(135) Zhang, J.; Matveeva, E.; Gryczynski, I.; Leonenko, Z.; Lakowicz, J. R. Metal-Enhanced Fluoroimmunoassay on a Silver Film by Vapor Deposition. *The Journal of Physical Chemistry B* **2005**, *109* (16), 7969-7975. DOI: 10.1021/jp0456842.

(136) Huang, T.-X.; Li, C.-W.; Yang, L.-K.; Zhu, J.-F.; Yao, X.; Liu, C.; Lin, K.-Q.; Zeng, Z.-C.; Wu, S.-S.; Wang, X.; et al. Rational fabrication of silver-coated AFM TERS tips with a high enhancement and long lifetime. *Nanoscale* **2018**, *10* (9), 4398-4405, 10.1039/C7NR08186C. DOI: 10.1039/C7NR08186C.

(137) Yang, L.-K.; Huang, T.-X.; Zeng, Z.-C.; Li, M.-H.; Wang, X.; Yang, F.-Z.; Ren, B. Rational fabrication of a gold-coated AFM TERS tip by pulsed electrodeposition. *Nanoscale* **2015**, *7* (43), 18225-18231, 10.1039/C5NR04263A. DOI: 10.1039/C5NR04263A.

(138) Umakoshi, T.; Yano, T.-a.; Saito, Y.; Verma, P. Fabrication of Near-Field Plasmonic Tip by Photoreduction for Strong Enhancement in Tip-Enhanced Raman Spectroscopy. *Applied Physics Express* **2012**, *5* (5), 052001. DOI: 10.1143/APEX.5.052001.

(139) Kim, W.; Kim, N.; Park, J. W.; Kim, Z. H. Nanostar probes for tip-enhanced spectroscopy. *Nanoscale* **2016**, *8* (2), 987-994, 10.1039/C5NR06657C. DOI: 10.1039/C5NR06657C.

(140) Dill, T. J.; Rozin, M. J.; Palani, S.; Tao, A. R. Colloidal Nanoantennas for Hyperspectral Chemical Mapping. *ACS Nano* **2016**, *10* (8), 7523-7531. DOI: 10.1021/acsnano.6b02403.

(141) Walke, P.; Fujita, Y.; Peeters, W.; Toyouchi, S.; Frederickx, W.; De Feyter, S.; Uji-i, H. Silver nanowires for highly reproducible cantilever based AFM-TERS microscopy: towards a universal TERS probe. *Nanoscale* **2018**, *10* (16), 7556-7565, 10.1039/C8NR02225A. DOI: 10.1039/C8NR02225A.

(142) Melmed, A. J. The art and science and other aspects of making sharp tips. *Journal of Vacuum Science & Technology B: Microelectronics and Nanometer Structures Processing, Measurement, and Phenomena* **1991**, *9* (2), 601-608. DOI: 10.1116/1.585467 (acccessed 2022/11/17).

(143) Ramanauskaite, L.; Xu, H.; Griskonis, E.; Batiuskaite, D.; Snitka, V. Comparison and Evaluation of Silver Probe Preparation Techniques for Tip-Enhanced Raman Spectroscopy. *Plasmonics* **2018**, *13* (6), 1907-1919. DOI: 10.1007/s11468-018-0705-7.

(144) Kharintsev, S. S.; Hoffmann, G. G.; Fishman, A. I.; Salakhov, M. K. Plasmonic optical antenna design for performing tip-enhanced Raman spectroscopy and microscopy. *Journal of Physics D: Applied Physics* **2013**, *46* (14), 145501. DOI: 10.1088/0022-3727/46/14/145501.

(145) Vasconcelos, T. L.; Archanjo, B. S.; Fragneaud, B.; Oliveira, B. S.; Riikonen, J.; Li, C.; Ribeiro, D. S.; Rabelo, C.; Rodrigues, W. N.; Jorio, A.; et al. Tuning Localized Surface Plasmon Resonance in Scanning Near-Field Optical Microscopy Probes. *ACS Nano* **2015**, *9* (6), 6297-6304. DOI: 10.1021/acsnano.5b01794.

(146) Zhang, D.; Wang, X.; Braun, K.; Egelhaaf, H.-J.; Fleischer, M.; Hennemann, L.; Hintz, H.; Stanciu, C.; Brabec, C. J.; Kern, D. P.; et al. Parabolic mirror-assisted tip-enhanced spectroscopic imaging for non-transparent materials. *Journal of Raman Spectroscopy* **2009**, *40* (10), 1371-1376, https://doi.org/10.1002/jrs.2411. DOI: https://doi.org/10.1002/jrs.2411 (acccessed 2022/11/18).

(147) Neacsu, C. C.; Dreyer, J.; Behr, N.; Raschke, M. B. Scanning-probe Raman spectroscopy with single-molecule sensitivity. *Physical Review B* **2006**, *73* (19), 193406. DOI: 10.1103/PhysRevB.73.193406.

(148) Jia, W.; Xiaobin, W.; Rui, W.; Mingqian, Z. Detection of Carbon Nanotubes using Tip-Enhanced Raman Spectroscopy. In *Electronic Properties of Carbon Nanotubes*, Jose Mauricio, M. Ed.; IntechOpen, 2011; p Ch. 10.

(149) Taguchi, A.; Hayazawa, N.; Saito, Y.; Ishitobi, H.; Tarun, A.; Kawata, S. Controlling the plasmon resonance wavelength in metal-coated probe using refractive index modification. *Opt. Express* **2009**, *17* (8), 6509-6518. DOI: 10.1364/OE.17.006509.

(150) Opilik, L.; Dogan, Ü.; Szczerbiński, J.; Zenobi, R. Degradation of silver near-field optical probes and its electrochemical reversal. *Applied Physics Letters* **2015**, *107* (9), 091109. DOI: 10.1063/1.4929880 (acccessed 2022/11/24).

(151) Barrios, C. A.; Malkovskiy, A. V.; Kisliuk, A. M.; Sokolov, A. P.; Foster, M. D. Highly Stable, Protected Plasmonic Nanostructures for Tip Enhanced Raman Spectroscopy. *The Journal of Physical Chemistry C* **2009**, *113* (19), 8158-8161. DOI: 10.1021/jp8098126.

(152) Agapov, R. L.; Sokolov, A. P.; Foster, M. D. Protecting TERS probes from degradation: extending mechanical and chemical stability. *Journal of Raman Spectroscopy* **2013**, *44* (5), 710-716, https://doi.org/10.1002/jrs.4268. DOI: https://doi.org/10.1002/jrs.4268 (acccessed 2022/11/24).

(153) Yeo, B.-S.; Schmid, T.; Zhang, W.; Zenobi, R. A Strategy to Prevent Signal Losses, Analyte Decomposition, and Fluctuating Carbon Contamination Bands in Surface-Enhanced Raman Spectroscopy. *Applied Spectroscopy* **2008**, *62* (6), 708-713. DOI: 10.1366/000370208784658165 (acccessed 2022/11/24).

(154) Giljohann, D. A.; Seferos, D. S.; Daniel, W. L.; Massich, M. D.; Patel, P. C.; Mirkin, C. A. Gold nanoparticles for biology and medicine. *Angew. Chem. Int. Ed. Engl.* **2010**, *49* (19), 3280-3294. DOI: 10.1002/anie.200904359.

(155) Fleger, Y.; Rosenbluh, M. Surface Plasmons and Surface Enhanced Raman Spectra of Aggregated and Alloyed Gold-Silver Nanoparticles. *Research Letters in Optics* **2009**, *2009*, 1-5. DOI: 10.1155/2009/475941.

(156) Zhang, W.; Schmid, T.; Yeo, B.-S.; Zenobi, R. Near-Field Heating, Annealing, and Signal Loss in Tip-Enhanced Raman Spectroscopy. *The Journal of Physical Chemistry C* **2008**, *112* (6), 2104-2108. DOI: 10.1021/jp077457g.

(157) Stadler, J.; Schmid, T.; Zenobi, R. Developments in and practical guidelines for tip-enhanced Raman spectroscopy. *Nanoscale* **2012**, *4* (6), 1856-1870, 10.1039/C1NR11143D. DOI: 10.1039/C1NR11143D.

(158) Yeo, B.-S.; Stadler, J.; Schmid, T.; Zenobi, R.; Zhang, W. Tip-enhanced Raman Spectroscopy – Its status, challenges and future directions. *Chemical Physics Letters* **2009**, *472* (1), 1-13. DOI: https://doi.org/10.1016/j.cplett.2009.02.023.

(159) Yang, Y.; Liu, J.; Fu, Z. W.; Qin, D. Galvanic replacement-free deposition of Au on Ag for core-shell nanocubes with enhanced chemical stability and SERS activity. *J. Am. Chem. Soc.* **2014**, *136* (23), 8153-8156. DOI: 10.1021/ja502472x.

(160) Fortuni, B.; Inose, T.; Uezono, S.; Toyouchi, S.; Umemoto, K.; Sekine, S.; Fujita, Y.; Ricci, M.; Lu, G.; Masuhara, A.; et al. In situ synthesis of Au-shelled Ag nanoparticles on PDMS for flexible, long-life, and broad spectrum-sensitive SERS substrates. *Chem. Commun. (Camb.)* **2017**, *53* (82), 11298-11301, 10.1039/C7CC05420C. DOI: 10.1039/c7cc05420c.

(161) Yang, M.; Hood, Z. D.; Yang, X.; Chi, M.; Xia, Y. Facile synthesis of Ag@Au core–sheath nanowires with greatly improved stability against oxidation. *Chemical Communications* **2017**, *53* (12), 1965-1968, 10.1039/C6CC09878A. DOI: 10.1039/C6CC09878A.

(162) Rycenga, M.; Cobley, C. M.; Zeng, J.; Li, W.; Moran, C. H.; Zhang, Q.; Qin, D.; Xia, Y. Controlling the Synthesis and Assembly of Silver Nanostructures for Plasmonic Applications. *Chemical Reviews* **2011**, *111* (6), 3669-3712. DOI: 10.1021/cr100275d.

(163) Korte, K. E.; Skrabalak, S. E.; Xia, Y. Rapid synthesis of silver nanowires through a CuCl- or CuCl2-mediated polyol process. *Journal of Materials Chemistry* **2008**, *18* (4), 437-441, 10.1039/B714072J. DOI: 10.1039/B714072J.

Chapter 2 Gold-Coated Silver Nanowires for Long Lifetime AFM-TERS Probes

This chapter is based on the following publication:

Wen, H.; Inose, T.; Hirai, K.; Akashi, T.; Sugioka, S.; Li, J.; Peeters, W.; Fron, E.; Fortuni, B.; Nakata, Y.; et al. Gold-coated silver nanowires for long lifetime AFM-TERS probes. *Nanoscale* **2022**, *14* (14), 5439-5446. DOI: 10.1039/D1NR07833J.

2.1 Abstract

Tip-enhanced Raman scattering (TERS) microscopy is an advanced technique for investigation at the nanoscale because of its excellent properties, such as label-free functionality, non-invasiveness, and the ability to simultaneously provide topographic and chemical information. The probe plays a crucial role in TERS technique performance. Widely used AFM-TERS probes fabricated with metal deposition suffer from relatively low reproductivity as well as their limited mapping and storage lifetime. To solve the reproducibility issue, silver nanowire (AgNW)-based TERS probes were developed, which, thanks to the high homogeneity of the liquid-phase synthesis of AgNW, can achieve high TERS performance with excellent probe reproductivity, but still presenting short lifetime due to probe oxidation. In this work, a simple Au coating method is proposed to overcome the limited lifetime and improve the performance of the AgNW-based TERS probe. For the Au-coating, different [Au]/[Ag] molar ratios were investigated. The TERS performance was evaluated in terms of change in enhancement factor (EF) and signal-to-noise ratio through multiple mappings and the storage lifetime in air. The Au-coated AgNWs exhibited higher EF than pristine AgNW and galvanic-replaced AgNW with no remarkable difference between the two molar ratios tested. However, for longer scanning time and multiple mappings, the probes obtained with low Au concentration showed much longer-term stability with keeping high EF. Furthermore, the Au-coated AgNW probes were found to possess a longer storage lifetime in air, allowing for long and multiple TERS mappings with one single probe.

2.2 Introduction

Tip-enhanced Raman scattering (TERS) microscopy is a powerful technique that enables simultaneous nanoscale characterization of topographic and chemical information with high spatial resolution, overcoming the diffraction limit of light.1 Since its first experimental demonstration in 2000,[1-3] TERS has been widely applied in the study of 1-dimensional (1D) materials,[4-7] 2-dimensional (2D) materials,[8-11] a few molecules,[12-14] nanostructured semiconductors,[15, 16] biomacromolecules,[17, 18] and biochemical identification.[19-21] TERS technique is realized by combining scanning probe microscopies (SPMs) with Raman spectroscopy to obtain detailed surface information by raster-scanning. Briefly, TERS achieves high signal enhancement and nanoscale spatial resolution that rely on the confinement of electromagnetic (EM) field at near-field. Polarized laser light is focused on an apex of a metalized scanning probe, at which the freely propagating far-field light is converted to a nanoconfined near-field EM field through the excitation of the localized surface plasmon resonances (LSPRs).[22] The LSPRs could significantly enhance the Raman scattering from the target sample underneath the apex. Since the spatial resolution of TERS is determined by the confinement size of LSPRs, it depends on the size of the apex that is typically a range of 10 ~ 20 nm or higher.[23, 24]

Atomic force microscope (AFM)-based TERS is widely used as being more stable, faster, and having no intrinsic substrate limitations.[25] While the vacuum-evaporation of noble metal on AFM cantilever has been commonly used to fabricate AFM-based TERS probes due to its large-scale fabrications nature,[26, 27] it suffers from several issues, such as low reproductivity, low mechanical strength, short lifetime, and eventually high costs.[28, 29] To address these issues, silver nanowire (AgNW)-based AFM-TERS probes were proposed as an easy bottom-up fabrication method.[25] Thanks to the high homogeneity of the large-scale AgNW synthesis, a well-controlled apex morphology and outstanding optical coupling property can be obtained, which give rise to high TERS reproducibility and activity. However, the use of silver as a plasmonically active material limits the lifetime of AgNW-based TERS probes, as fast silver oxidation occurs upon air exposure.

Here, based on the bottom-up probe fabrication method, we introduce Au-coated AgNW (Ag@Au NW) as a highly sensitive, long life TERS active antenna. The synthesis of Ag@Au NWs is based on Au atoms conformal deposition method[30] on the surface of AgNW

synthesized by polyol method.[31, 32] The performance of Ag@Au NW with different Au/Ag ratios was evaluated in terms of enhancement factor (EF) and lifetime. This work demonstrates that the Ag@Au NW probes with an Au/Ag ratio of ~10^{-6} show higher EF and a longer lifetime than those with pristine AgNWs and Au-etched AgNW synthesized by galvanic replacement reaction (GRR).

2.3 Experiment section

Materials

Silver nitrate ($AgNO_3$), tetrachloroauric (III) acid ($HAuCl_4$), ethylene glycol (EG, anhydrous, 99.8%), hydrochloric acid (HCl) were obtained from SIGMA-ALDRICH. Copper chloride ($CuCl_2$) and polyvinylpyrrolidone K30 (PVP), L-ascorbic acid (AA), isopropanol (IPA), tetrahydrofuran (THF) and toluene were purchased from FUJIFILM Wako Pure Chemical Corporation. Single wall carbon nanotubes (CNTs) were purchased from SIGMA-ALDRICH. All chemicals were used without further purification.

Silver nanowire synthesis

AgNWs were synthesized according to the polyol method[31, 32] with some modifications. Briefly, 0.3 mM of PVP was dissolved in 9.7 mL of EG and heated at 160°C for one hour under magnetic stirring (600 rpm). Then, 80 µL of $CuCl_2$ solution in EG (4 mM) was added to the solution under higher speed stirring (1,000 rpm) for 10 min, followed by the addition of 100 µL of $AgNO_3$ solution in EG (0.12 M). After the color of the solution turned greenish, 4.9 mL of $AgNO_3$ solution in EG (0.12 M) was added drop-wise at a rate of 100 µL/min. Thereafter, the mixture was maintained at 160°C for 2 hours under stirring (600 rpm). Finally, the mixture was cooled down to room temperature, obtaining high-yield AgNWs. These NWs were then washed three times with IPA. A typical SEM image of the final product is shown in Fig. 2-A1 in the appendix.

Silver nanowire gold etching

The Au etching of AgNWs was performed according to the GRR method[3, 33] with some modifications,[34] which procedure is schematically shown in Fig. 2-1a. 15 mL of Milli-Q water was heated at 80°C for 10 minutes and 900 µL of the AgNWs (~400 µg/mL) solution was then added, followed by adding 1.8 mL of 0.2 mM of HAuCl4 solution. The mixture was kept at 80°C for 15 min. The products were washed three times by centrifugations in IPA at 1200 rpm.

Silver nanowire gold coating

The Au coating of AgNWs was performed according to the Au atoms conformal deposition method with some modifications,[30, 34] which procedure is schematically shown in Fig. 2-1b.

0.1 mL of $HAuCl_4$ (2 mM or 0.2 µM that corresponds to a molar ratio of Au^{3+} over Ag^+ (n_{Au}/n_{Ag}) equal to 0.0386 or 3.86×10^{-6}, respectively) was mixed with 2 mL of NaOH (0.2 M) and 17.9 mL of Milli-Q for one hour under magnetic stirring at 400 rpm. 120 mg PVP, 1.5 mL of AA (100 mM), 1.5 mL NaOH (0.2 M), and 210 µL of AgNW (~400 µg/mL) was added into 3 mL Milli-Q and heated at 80°C under magnetic stirring (400 rpm). Then, 3 mL of prepared $HAuCl_4$ mixture solution was added to the prepared AgNW mixture solution at a rate of 300 µL/min. Then, the Au-coated AgNWs were collected by centrifugations at 1200 rpm (x3) and resuspension in IPA.

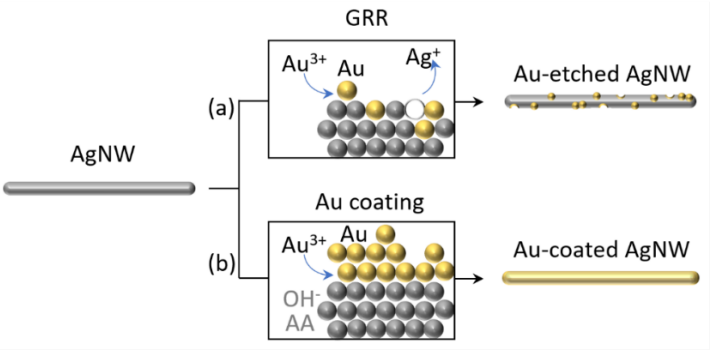

Figure 2-1. Schematic illustration of the synthesis of (a) Au-etched AgNW and (b) Au-coated AgNW.

Fabrication of silver nanowire functionalized AFM tip

The schematic illustration of the probe fabrication setup and the optical transmission images of the probe during the fabrication are shown in Fig. 2-A2a and Fig. 2-A2b to e, respectively. The apex of Micro AFM cantilevers (160AC-NA, OPUS) was dipped into a droplet of AgNWs that typically contains approximately 5 µL of diluted AgNW IPA solution (~40 µg/mL) with 25 µL of Milli-Q water. A 1 MHz square wave with 14 V_{p-p} and 0 V DC offset with 50% duty cycle provided by a function generator (JDS-2900, JUNTEK) was applied for usually 0.5-3 s between the cantilever and the droplet to achieve the nanowire attachment through AC-dielectrophoresis.[33] This procedure was repeated until less than 5 µm of the protruded length of the attached AgNW was achieved for stable TERS operation.[25]

Preparation of CNT on Au (111)

Au (111) substrates purchased from PHASIS (Switzerland) were first rinsed with acetone, ethanol, and Milli-Q and brow dried by N_2. The substrate was then flame annealed with a piezo

gas burner for a few seconds to remove contaminations and then cooled under N_2 atmosphere. ~0.3 mg CNT was dissolved in 5 mL THF at a saturated concentration and dispersed by ultrasonication for several hours. The CNT suspension was diluted 5 times to an almost transparent state (~12 μg/mL) and then dispersed by ultrasonication for several hours again. The dispersed CNT solution was drop-casted onto the prepared substrate followed by rinsing with Milli-Q and brow drying by N_2. This step was repeated by 2-3 times until the coverage of CNTs became sufficient for TERS measurement.

AFM/TERS measurements

AFM/TERS measurements were carried out on an OmegaScope™ (AIST-NT, HORIBA) with a homemade optical platform, as shown in Fig. 2-A3. Laser line from a He-Ne laser (632.8 nm, LASOS) was focused onto the sample/tip by an objective (MITUTOYO, M plan Apo 100×, N.A. 0.7) after being reflected by a dichroic mirror (LPD02-633RU, Semrock). The same objective was used to collect Raman scattering, and the collected scattering was directed through the dichroic mirror, a pinhole (diameter 100 μm), and a long-pass filter (LP02-633RE, Semrock) to a Raman spectrograph (SOLAR TII, MS3501i) equipped with a charge-coupled device (CCD) camera (Andor, Newton 920). Prior to TERS mapping, in order to align the laser on the apex of the TERS probe, Rayleigh scattering mapping was performed by objective scanning without the long-pass filter. All AFM/TERS measurements were performed under ambient conditions at room temperature. All TERS data were calibrated using Raman spectrum of toluene and implemented baseline subtraction by a model-free small window moving average-based baseline estimation method if necessary.[35] Omega software (AIST-NT/HORIBA), home-build routine in MATLAB (MathWorks), Igor Pro (WaveMetrics), and Origin (OriginLab) were used for data analysis.

Characterization of AgNWs

The morphology of pristine AgNWs, Ag@Au NWs, and Au-etched AgNWs was characterized by field-emission scanning electron microscopy (FE-SEM, JEOL JSM-6700FT at 5.0 kV) and scanning transmission electron microscopy (STEM, HITACHI HD-2000 equipped with energy-dispersive X-ray (EDX) spectroscopy with an acceleration voltage of 200 kV). The element amount was characterized by inductively coupled plasma optical emission spectroscopy (ICP-OES, ICPE-9000, SHIMAZU CORPORATION) and nanoscale-secondary ion mass spectroscopy (NanoSIMS 50L, CAMECA).

2.4 Results and discussion

Characterization of Ag@Au NWs

The mechanisms of GRR and Au-coating of AgNWs are schematically illustrated in Fig. 2-1a and 1b, respectively. The replacement of Ag atoms with Au atoms and thus the formation of Au-Ag alloy clusters on NWs are caused by electron transfer from Ag^0 atoms on AgNW surface to Au^{3+} in GRR due to the lower standard reduction potential of Ag than Au. On the other hand, Au layers deposition avoiding GRR can be realized by circumventing the replacement at alkaline reaction conditions (pH ~ 11), which dramatically increases the reducing power of AA and lowers the reduction potential of the Au3+ by converting $AuCl^{4-}$ into $Au(OH)^{4-}$.[36, 37] Two different concentrations of Au^{3+} for Au-coating with n_{Au}/n_{Ag} of 3.85×10^{-2} and 3.85×10^{-6}, were evaluated (denoted as Ag@Au NW-H and Ag@Au NW-L in the following text, respectively).

Pristine AgNWs, Au-etched AgNWs, Ag@Au NW-H and -L were characterized by means of FE-SEM, STEM, and EDX (Fig. 2-2). Pentagon-shaped AgNWs were successfully synthesized with smooth surface morphology for the pristine AgNWs (Fig. 2-2a). After GRR, hollow structures were formed (Fig. 2-2f), and Au was detected by EDX around the hollows (Fig. 2-2g, 2h). In contrast, after the Au-coating, the flat facets remain flat without hollow formations, while the facet boundaries of Ag@Au NW-H became rough (Fig. 2-2i, 2j). Thus, it can be qualitatively concluded that the apex and facet boundary has a higher affinity to the Au atom, which is in accordance with the reported phenomenon that the corners and the edges possess lower energy barriers than the facets, leading to easier nucleation at the apex and boundary.[38] The thickness of Au layers is estimated to be less than 10 nm from the EDX mapping. At the low molar ratio for Ag@Au NW-L, Au was not detected by EDX, which is likely due to the limited amount of Au atoms for the EDX sensitivity (Separated Au and Ag EDX mapping for Au-etched AgNW, Ag@Au NW-H, and Ag@Au NW-L are shown in Fig. 2-A4 to 2-A6.). To confirm the existence of Au atoms on AgNWs, ICP-OES measurements have been conducted for both Ag@Au NW-H and Ag@Au NW-L. The ICP-OES spectra are shown in Fig. 2-A7 and 2-A8, from which clear peaks of Au in both samples are detected for both conditions. To further characterize the spatial distribution of Au on Ag@Au NW-L, NanoSIMS measurement was conducted. Fig. 2-A9 compares the NanoSIMS elemental mappings of Ag@Au NW-L with pristine AgNW, from which Au was detected only in Ag@Au NW-L. This indicates that

Au atoms were successfully deposited and distributed over the nanowire instead of aggregating, even at the low concentration of Au.

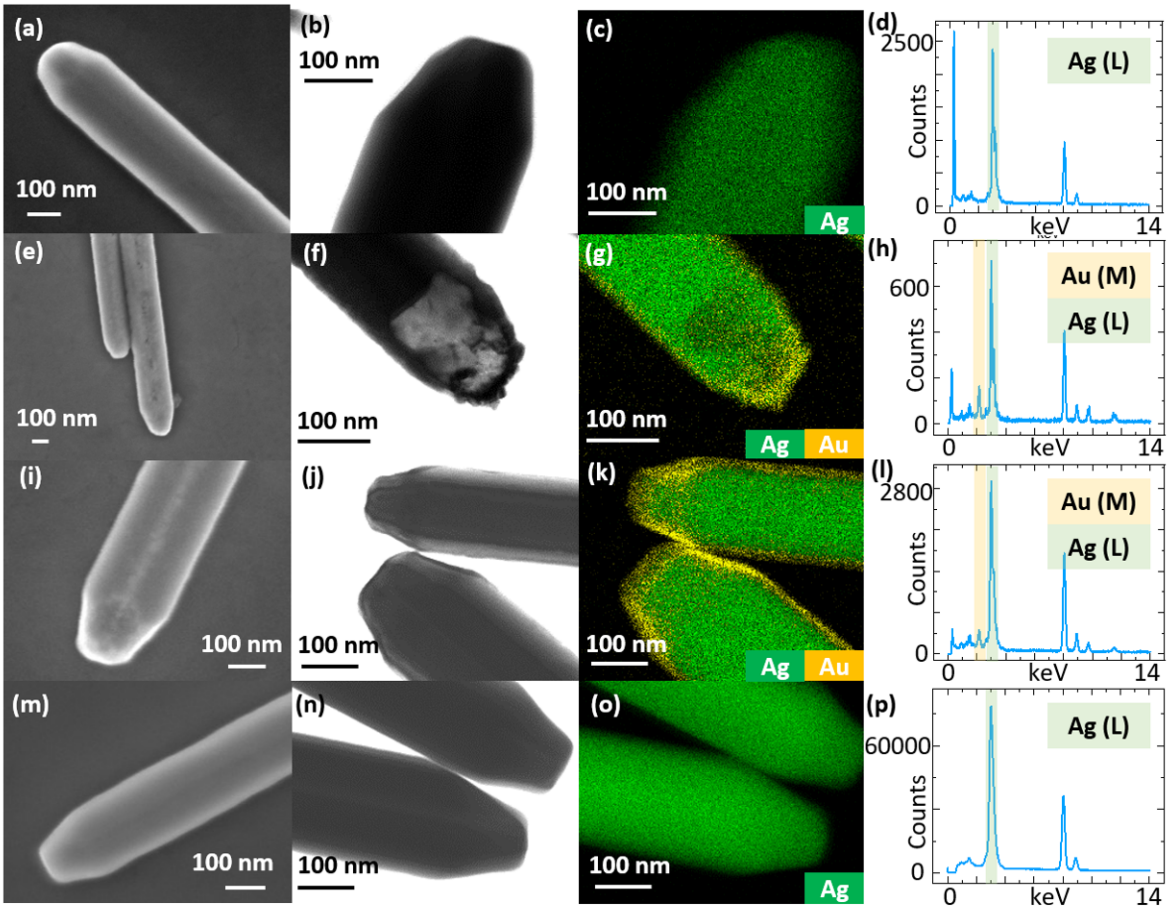

Figure 2-2. Characterization of pristine, Au-etched, Ag@Au NW-H and Ag@Au NW-L: (a), (e), (i), and (m) display SEM images, (b), (f), (j), and (n) are high magnification STEM image, (c), (g), (k), and (o) represent EDX elemental mapping (green; Ag, yellow; Au. Intensity of each element is independently normalized for better visualization). The corresponding EDX spectra accumulated in each imaging area for pristine, Au-etched, Ag@Au NW-H and Ag@Au NW-L are displayed in (d), (h), (I), and (p), respectively

Evaluation of Ag@Au NW TERS probes

Besides spontaneous oxidation of metal probes upon exposure to the air, light-induced oxidation could cause a rather quick reduction of TERS activity. The local heating effect due to Ohmic loss of plasmons could accelerate oxidation and even lead to morphological changes on the probe apex. Therefore, we investigated the durability of TERS activity upon continuous laser irradiation and the storage lifetime in the air at room temperature. CNTs on Au (111)

were chosen as a sample to evaluate the TERS activity of the probes. The G-band intensity at ~1580 cm^{-1} on the TERS spectra obtained from different probes was used for calculating the respective TERS EFs.

Durability test

For the durability test, multiple TERS mappings were repeatedly conducted at the same single CNT under the same measurement conditions, such as integration time and laser power. Fig. 3 shows TERS mapping of CNTs obtained by using a pristine AgNW (Fig. 3a), Au-etched AgNW (Fig. 3b), Ag@Au NW-H (Fig. 3c), and Ag@Au NW-L (Fig. 3d) as TERS probe, respectively. In each panel, i and ii refer to the first and 15th TERS mapping at G-band out of consecutive 15 mappings, respectively, while iii refers to the AFM topographic image, iv to the line profile along the white line in the AFM image, and v to the corresponding TERS spectra at pixel A and B in the corresponding TERS mappings (i and ii), respectively. These TERS mapping images consist of 20 x 20 pixels (10 nm/pixel), in which Raman spectra were taken at every pixel with an integration time of 0.4 s. Thus, TERS probes were continuously exposed to the laser excitation for ~ 160 s during one complete mapping, leading to a total exposure for at least 40 minutes over 15 mappings, excluding the lag time between consecutive mappings. Note that laser focus position on the probe apex was realigned between each consecutive mapping in order to rule out the effect of optical misalignment due to thermal drift of the optics/probe. For this alignment, the laser power was reduced by further 100 times compared to the mapping condition to avoid extra light-induced damages.

At the 1st TERS mapping with freshly prepared TERS probes, Ag@Au NW-H and Ag@Au NW-L show relatively high Raman intensity (1000 ~ 2000 cps at G-band) compared to the pristine and Au-etched NWs (100 ~ 400 cps at G-band). Remarkably, the TERS activity of Au-coated AgNWs remains higher even after 15 times mapping.

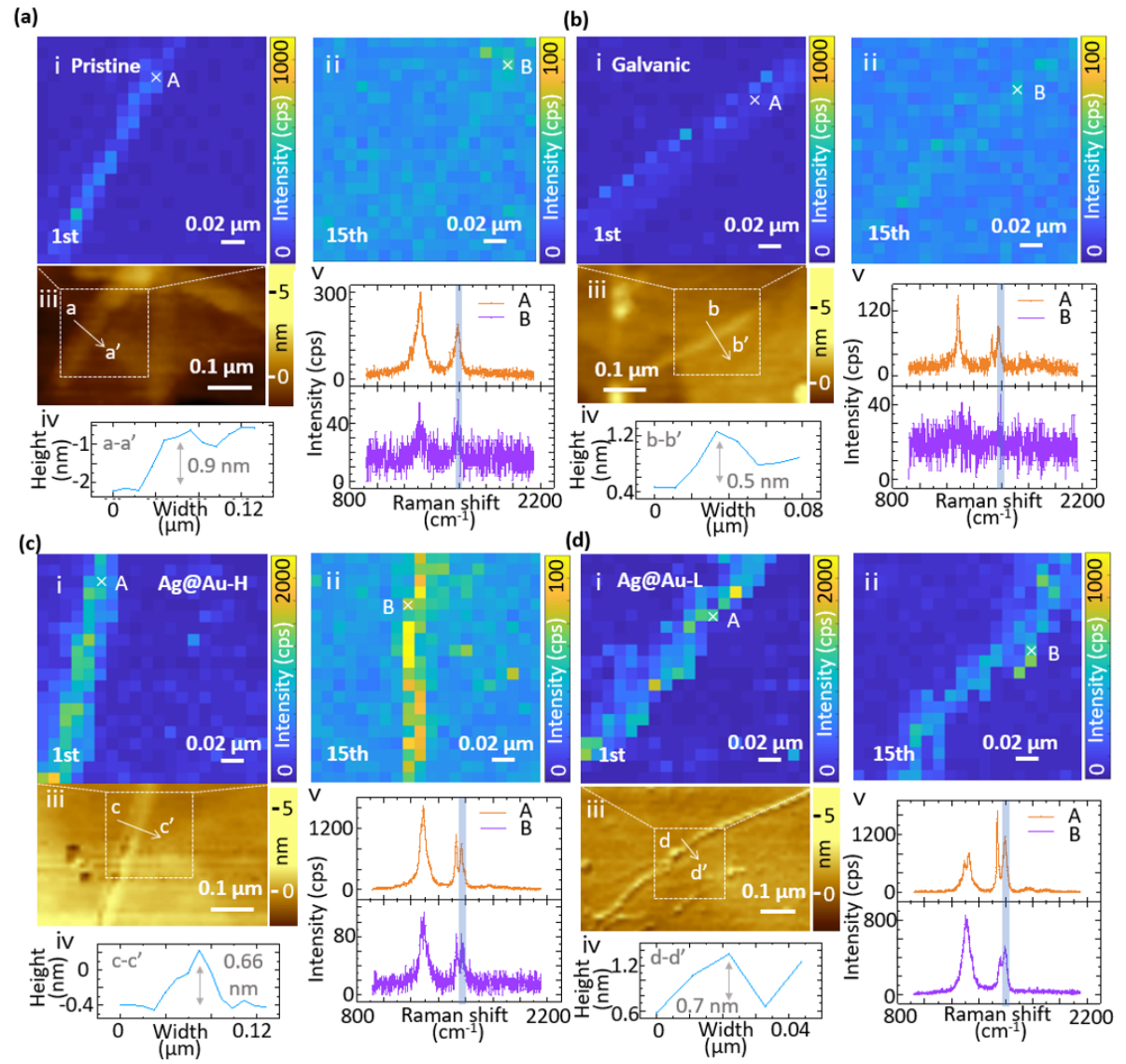

Figure 2-3. TERS with different probes: (a) pristine AgNW; (b) Au-etched AgNW; (c) Ag@Au NW-H; (d) Ag@Au NW-L. In all subfigures, i refers to the first TERS mapping; ii refers to the 15th TERS mapping; iii refers to the AFM image; iv refers to the line profile of the CNT in iii; v refers to the TERS spectra of pixel A in i and pixel B in ii. (Acquisition time was 0.4 s, accumulation once, 20×20 pixels (10 nm/pixel), laser power ~3.66 kW/cm^2, and the Raman intensity of G-band (cps) is selected to evaluate the TERS enhancement.)

To quantitatively evaluate the durability, the EF of each probe was calculated on 15 TERS maps (the detailed calculation method is shown in appendix). For each mapping run, 10 pixels showing CNT Raman spectrum are picked to calculate the averaged EF and its standard deviation (at least 3 different probes were evaluated for each probe condition). Fig. 2-4 displays the EF as a function of the number of mapping runs. The decay curves of pristine AgNWs and

Au-etched AgNWs were well fitted with a single exponential function, while those of Ag@Au NW-H and Ag@Au NW-L were best fitted with a double exponential (see equation 2-A1 to 2-A4 in appendix). The EF decay was observed regardless of the probe types, suggesting that metal oxidation/sulfidation occurs spontaneously for all probes. The fitting parameters are summerized in table 2-1. Note that the error bars of Ag@Au NW-H and Ag@Au NW-L are visually larger than those of the other two probes. To explain this, the EFs are analyzed with histogram (Fig. 2-A10 and 2-A11). The EFs of Au coated samples are higher than others, thus the standard deviation becomes mathematically larger. Besides, with higher EF probes, more detailed signal that does not appear in the TERS mapping with low EF probes can be detected. This also could cause the wide distribution of EFs in the case of Ag@Au NWs.

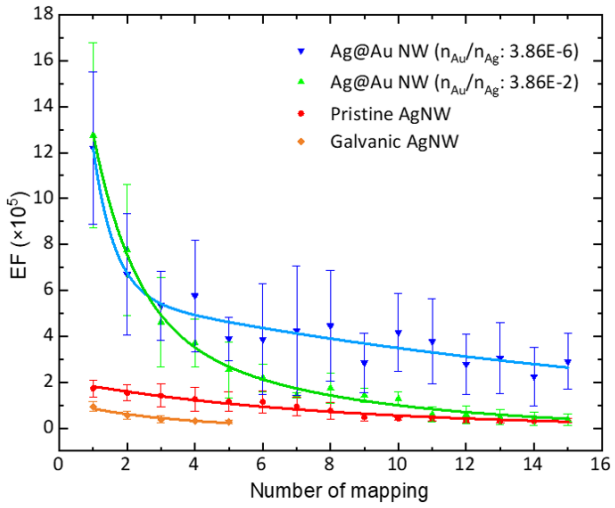

Figure 2-4. EF of 4 kinds of TERS probes, namely pristine AgNW (red), galvanic AgNW (orange), Ag@Au NW-H (green), and Ag@Au NW-L (blue), as a function of the number of mappings.

Table 2-1. The decay constants of the probes shown in Figure 4

	# of mapping run	# of mapping run
Ag NW	7.5 ± 0.51	N.A.
Au-etched AgNW	3.0 ± 0.36	N.A.
Ag@Au NW-H	1.4 ± 0.17	7.4 ± 1.6
Ag@Au NW-L	0.63 ± 0.23	17.9 ± 4.4

Pristine AgNWs showed an EF of ~ 2 x 10^5 at 1st run and allowed for multiple mappings maintaining EFs in the range of 10^5 (with the decay constant of 7.5 maping runs), as previously

reported by our group.[25] While higher EFs as well as longer durability were found on Ag@Au NWs, Au-etched AgNWs showed the lowest EF among probe types, albeit in the presence of gold. The EF decay constant of Au-etched AgNWs was estimated to 3 mapping runs, which is approximately 2 times worse than pristine AgNWs (Fig. 4 and equation 2-A1 to 2-A2 in appendix). This limited TERS performance of Au-etched AgNWs may arise from the increased oxidation of probe metals due to the absence of the protecting layer of PVP, removed during the GRR reaction. Another drawback of Au-etched AgNWs is their hollow structures, which can result in low mechanical strength and possible extra plasmonic damping.

In contrast, Ag@Au NW-H and -L showed the highest EFs in the order of 10^6 at the beginning, that is, 5-10 times higher than that of pristine AgNWs (Fig. 2-4). The improvement of EF is in line with previous reports where $Ag_{core}Au_{shell}$ bimetallic nanoparticles and NWs showed increased Raman enhancement than monometallic Ag nanostructures.[39-41] In terms of the durability, the 2nd decay constants, which can be attributed to the spontaneous oxidation of probe metals, were comparable or even longer than pristine AgNWs (5.7 and 18 mapping runs for Ag@Au NW-H and -L, equation 2-A3 to 2-A4 in appendix, respectively), suggesting a fine protection against metal oxidation through the gold layers. On the other hand, Ag@Au NWs exhibited the additional 1st decay component (1.2 and 0.6 mapping runs for Ag@Au NW-H and -L, respectively), and this could be attributed to slight morphological changes in the nanowire apex, induced by physical contact with the sample surfaces and/or by plasmonic heating of gold. To clarify this, two series of experiments were carried out. Firstly, Ag@Au NW-H was subjected to one TERS mapping under laser irradiation (Fig. 2-A12a ii), followed by six mappings without laser excitation (in the dark) under the same scan parameters (Fig. 2-A12a iii - viii). Then, two additional TERS mappings were taken with laser excitation (Fig. 2-A12a ix and x). EFs at the additional two mappings after the six- scans in dark, which does not affect on EFs of the probe as shown in 2-A12d (the EFs after multiple scans in dark were in the range of 1 - 5 x 10^5 that coincide with those in Fig. 4). This suggests that simple physical contact with sample surfaces does not lead to the EF decay. Secondly, to assess light-induced effects, the shape of the Ag@Au NW-H apex before and after 10 TERS mapping runs was evaluated using FE-SEM. From the SEM images in Fig. 2-A13, slight morphological changes were observed in Ag@Au NW-H after 10 TERS mapping runs, while such changes were not confirmed for Ag@Au NW-L (Fig. 2-A14) and pristine AgNWs. Based on these results, we conclude that the 1st EF decay component in Ag@Au NWs is due to slight changes in apex

metal structures induced by plasmon-heating of gold and importantly, in order to minimize this effect, the gold concentration needs to be as low as Ag@Au NW-L.

Storage Lifetime of Ag@Au NW

Thanks to the long durability of Ag@Au NW-L, TERS measurement can be conducted by using the same probe for long and multiple scans. This means that the probe can be stored to be re-used for individual experiments on different days. However, spontaneous oxidation of the probe upon air exposure could happen during the storage resulting in a reduction of the EF. It is therefore important to evaluate the storage lifetime of the probe. To this end, after a few TERS mappings, the pristine AgNW and the Ag@Au NW-L were stored in the air at room temperature. The mappings obtained after 1 week were compared to the ones on the first day (Fig. 5 and Fig. 2-A15). While about 75% (6 out of 8) of the pristine AgNW probes lost their TERS activity within one week (no Raman signal was detected as shown in Fig. 2-5a (iii) and (iv)), 70 % (9 out of 13) of Ag@Au NW-L probes maintained their activity even after one week (Fig. 5b (iii) and (iv)). To be more quantitative, Fig. 2-6 displays EFs of typical Ag@Au NW-L and pristine AgNWs before and after being stored in air for one week (see also Table 2-A1). Although the reductions of the EF are found also for Ag@Au NW-L most likely due to spontaneous oxidation, the EFs of two of three probes remain in the range of ~2 x 10^5 that is comparable to the freshly prepared AgNW probe. These results prove that the storage lifetime of Ag@Au NW-L probes is significantly improved by the Au coating.

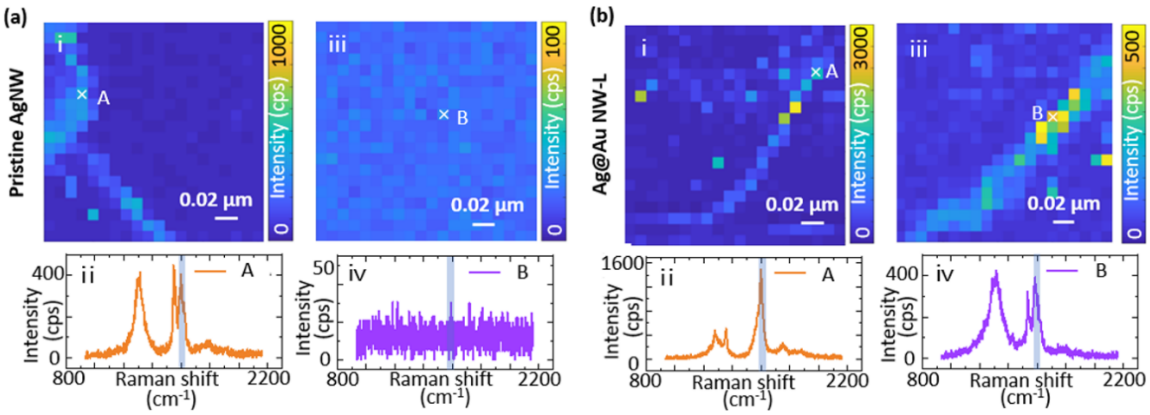

Figure. 2-5 Lifetime study of different TERS probes: (a) pristine AgNW probe; (b) Ag@Au NW-L probe. In both subfigures, i refers to the 1st mapping on first day prepared; ii refers to the TERS spectrum of the chosen pixel in i; iii refers to the 1st mapping after storing the same probe in air for one week; iv refers to the TERS spectrum of the chosen pixel in iii. (Acquisition

time was 0.4 s, accumulation once, 20×20 pixels (10 nm/pixel), laser power ~3.66 kW/cm^2, and the Raman intensity of G-band (cps) is selected to evaluate the TERS enhancement.)

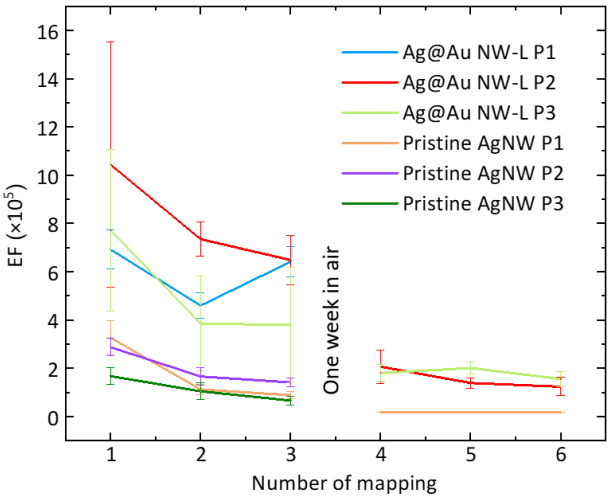

Figure 2-6. EF of 3 Ag@Au NW-L and 3 pristine AgNWs on the first day being prepared (M1~M3) and after being stored in air for one week (M4~M6)

2.5 Conclusion

We demonstrated a noble approach to prolong the lifetime and improve the TERS enhancement of AgNW-based TERS probes by using GRR-suppressed gold atom deposition. The Au coating on AgNW TERS probes was found to be simple and reproducible. To evaluate their performance, pristine AgNW, Au-etched AgNW by GRR, and Au-coated AgNW were compared in terms of TERS EF, durability and storage lifetime. The Au-coated AgNW probes showed more than 5 times higher EF than pristine AgNW probes and were able to be repeatably used for over 15 TERS mappings without a significant decrease of EF. Such exclusive durability allows to investigate the detail of the samples requiring high sensitivity and scanning multiple places on the sample of interest. In contrast, AgNW treated with GRR results in low EF and low stability due to the heterogeneous nature of GRR as well as their hollowed structures. Thanks to the oxidation resistance of the Au-coated AgNW, the probes can be stored even in the presence of oxygen for at least one week. We believe that the advanced Au-coated AgNW-based TERS probe is a promising tool for high-quality nanoscale characterization for example quality control of nanostructured semiconductors, detailed investigation of 2D materials such as chemically modified graphene or transition metal dichalcogenide (TMD), and even biological specimens.

2.6 Appendix

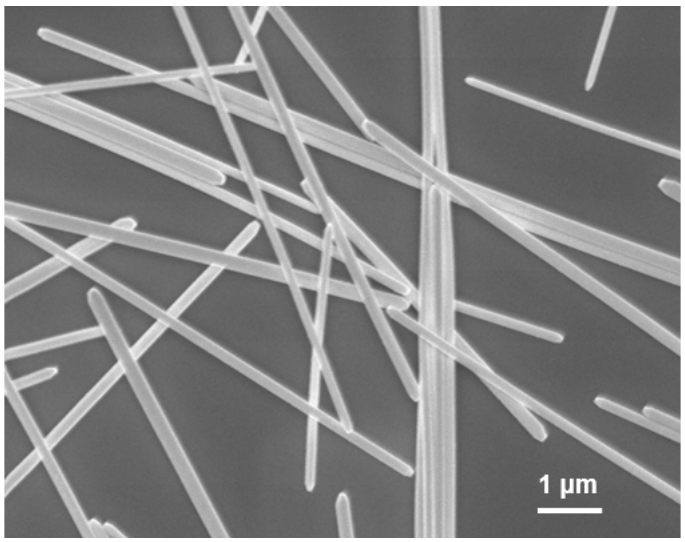

Figure 2-A1. SEM image of pristine AgNW

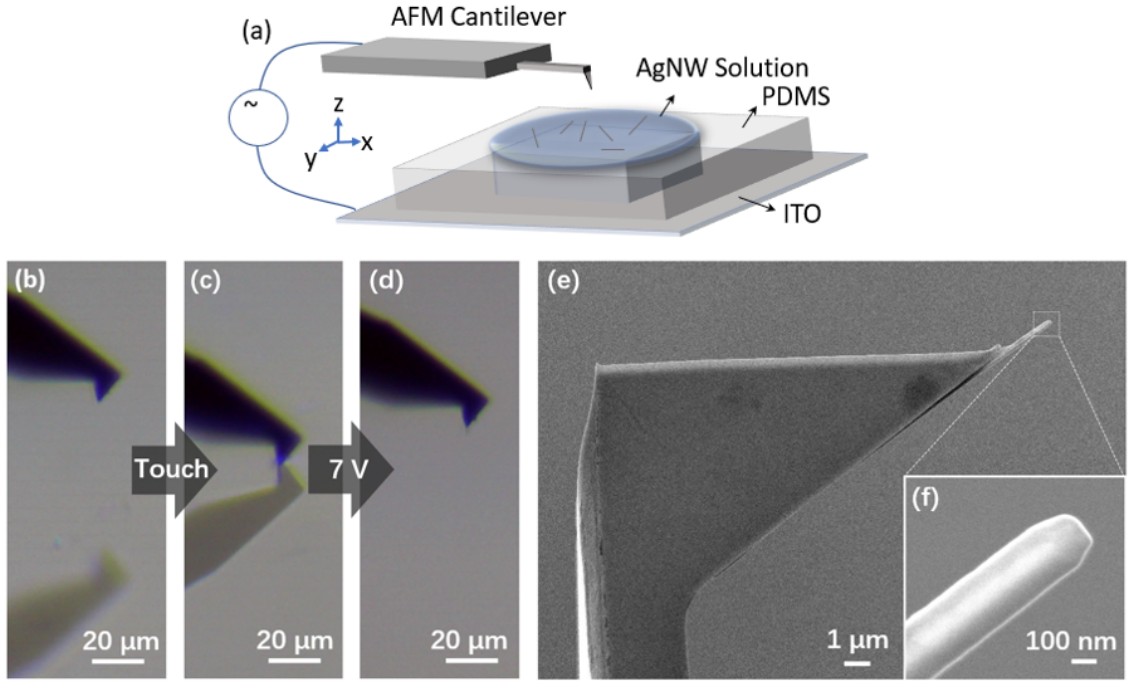

Figure 2-A2 (a) Schematic illustration of TERS probe fabrication; (b-d) optical transmission image of AgNW attachment: (b) before; (c) during; (d) after; (e-f) SEM image of TERS probe (using Ag@Au NW with n_{Au}/n_{Ag} equals to 3.85×10^{-6})

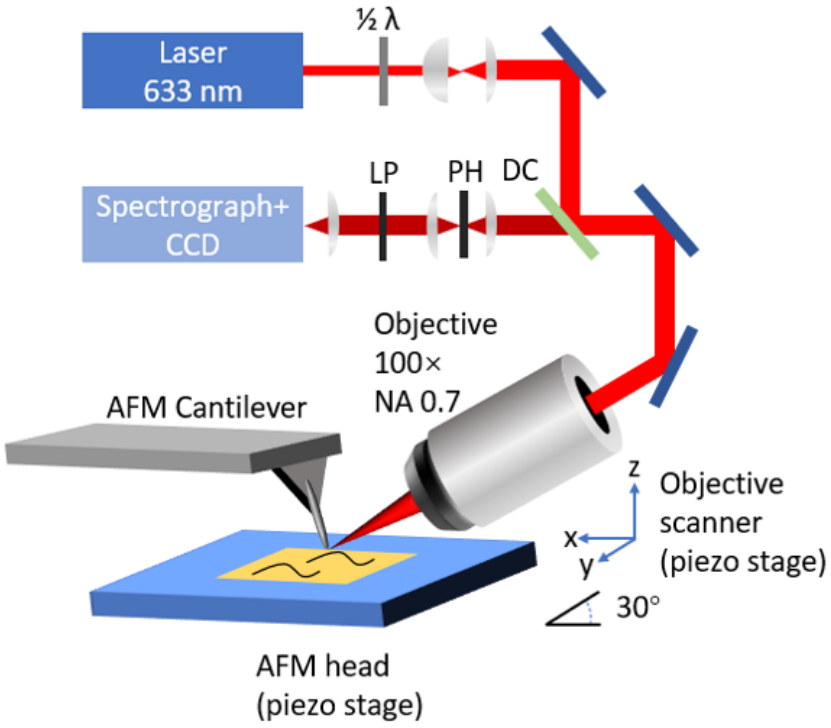

Figure 2-A3. Schematic illustration of AFM-TERS setup. (LP: long-path filter, PH: pin hole, DC: dichroic mirror, l/2: half-wave plate, respectively)

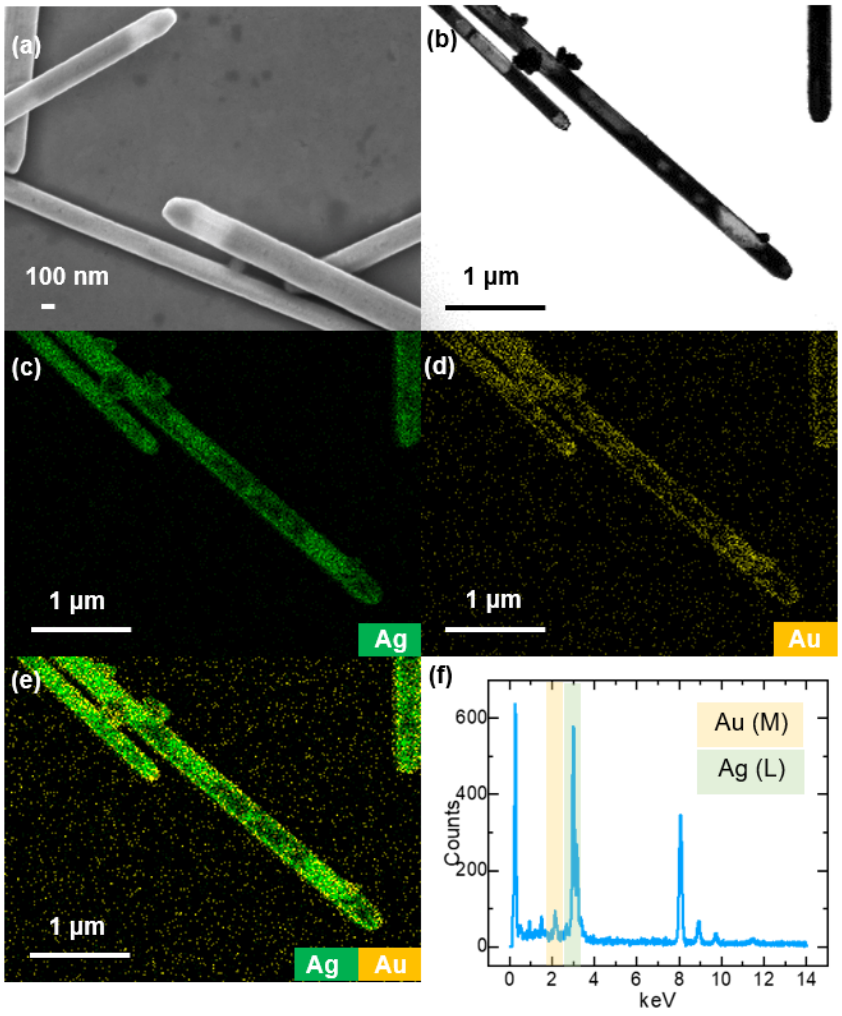

Figure 2-A4. Characterization of galvanic AgNW: (a) Low magnification SEM image; (b) Low magnification STEM image; (c) EDX mapping of Ag(L); (d) EDX mapping of Au (M); (e) EDX mapping of Ag (L) and Au (M); (f) EDX spectrum.

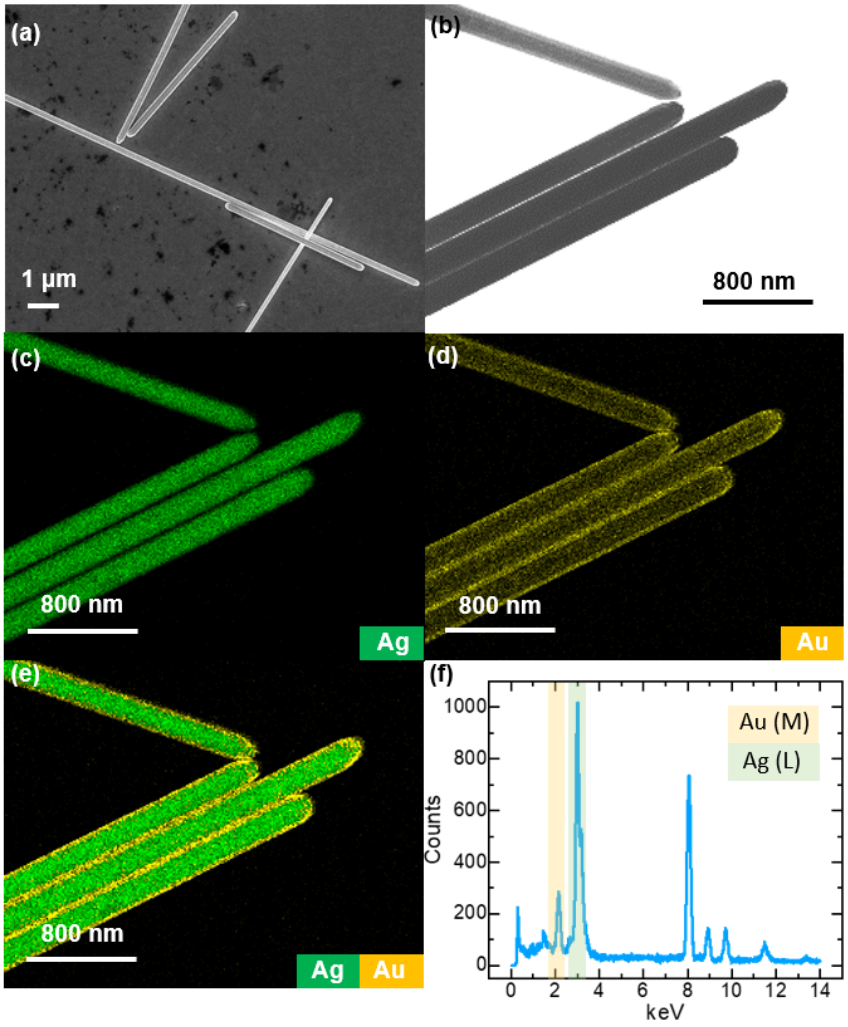

Figure 2-A5. Characterization of Ag@Au NW-H: (a) Low magnification SEM image; (b) Low magnification STEM image; (c) EDX mapping of Ag(L); (d) EDX mapping of Au (M); (e) EDX mapping of Ag (L) and Au (M); (f) EDX spectrum.

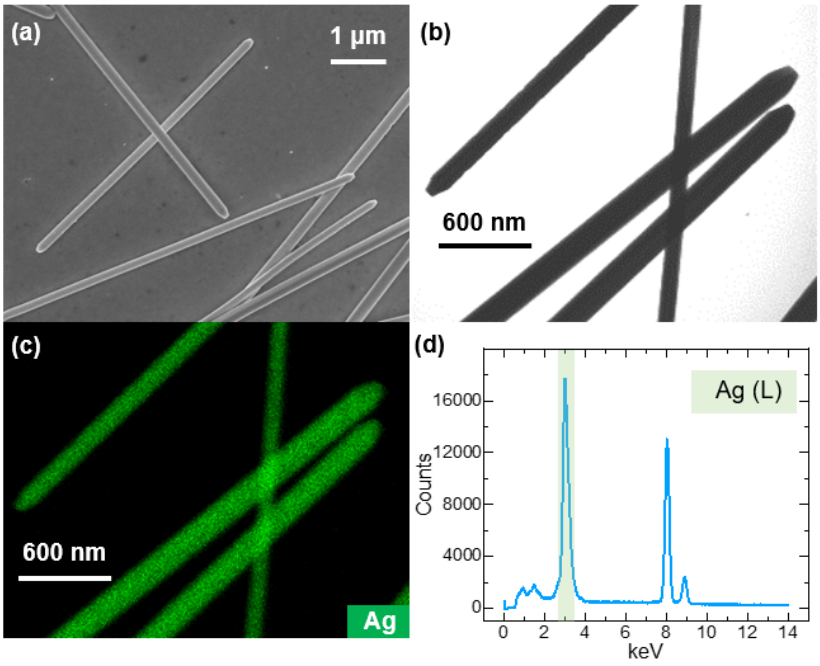

Figure 2-A6. Characterization of Ag@Au NW-L: (a) Low magnification SEM image; (b) Low magnification STEM image; (c) EDX mapping of Ag (L) (d) EDX spectrum.

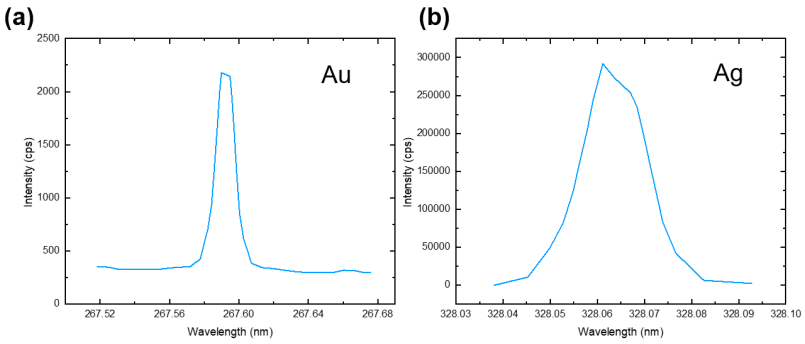

Figure 2-A7. ICP-OES of Ag@Au NW-H of (a): Au; (b): Ag

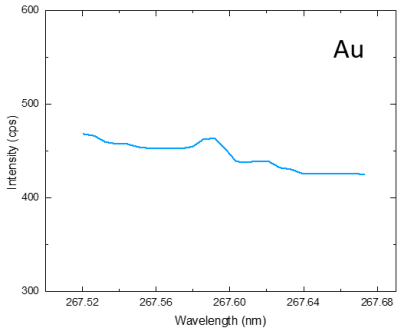

Figure 2-A8. ICP-OES of Ag@Au NW-L (Au)

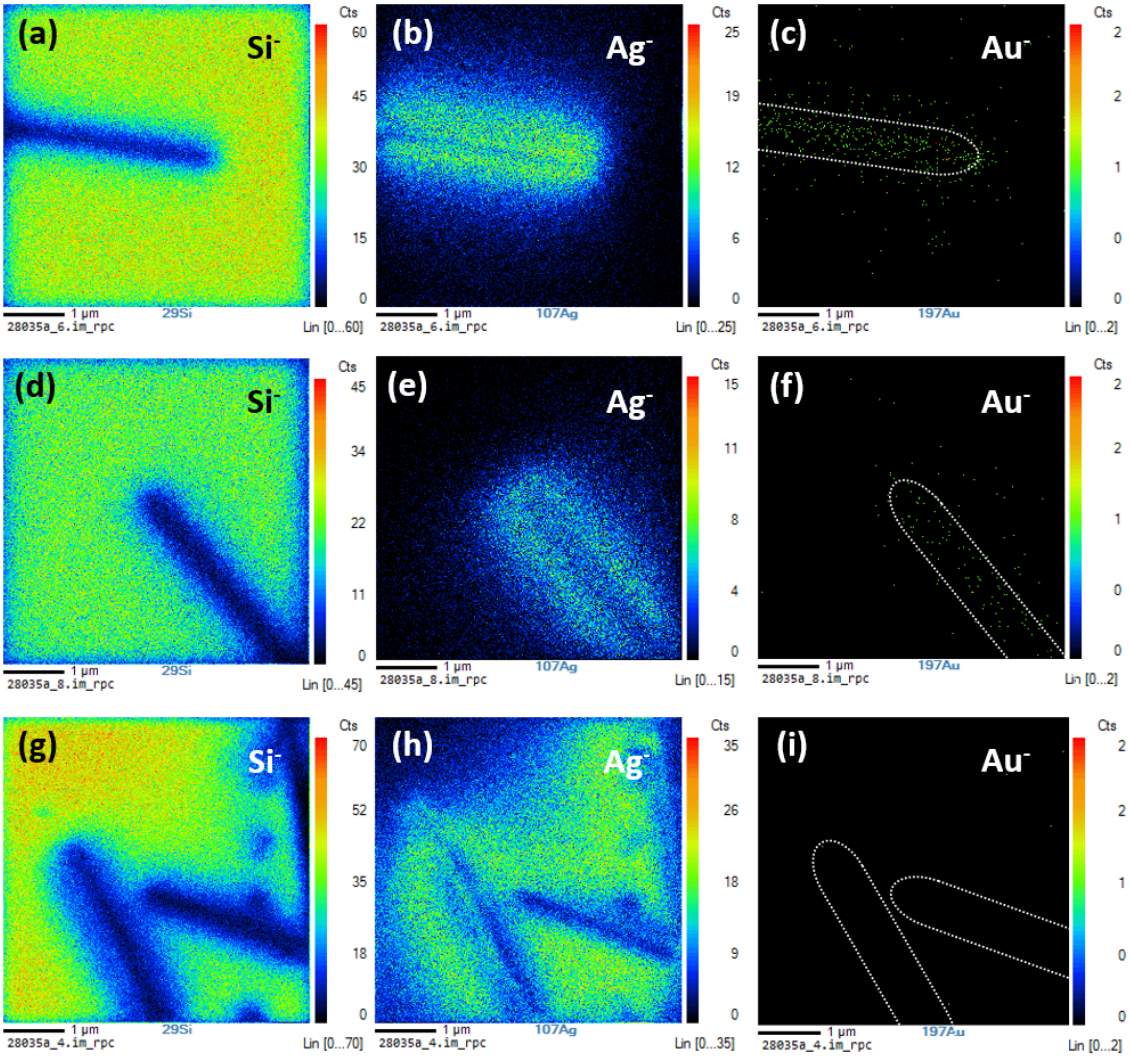

Figure 2-A9. NanoSIMS of Ag@Au NW-L and pristine AgNW: (a-c) NanoSIMS mapping of Si, Ag and Au of Ag@Au NW-L 1; (d-f) NanoSIMS mapping of Si, Ag and Au of Ag@Au NW-L 2; (g-i) NanoSIMS mapping of Si, Ag and Au of two pristine AgNWs.

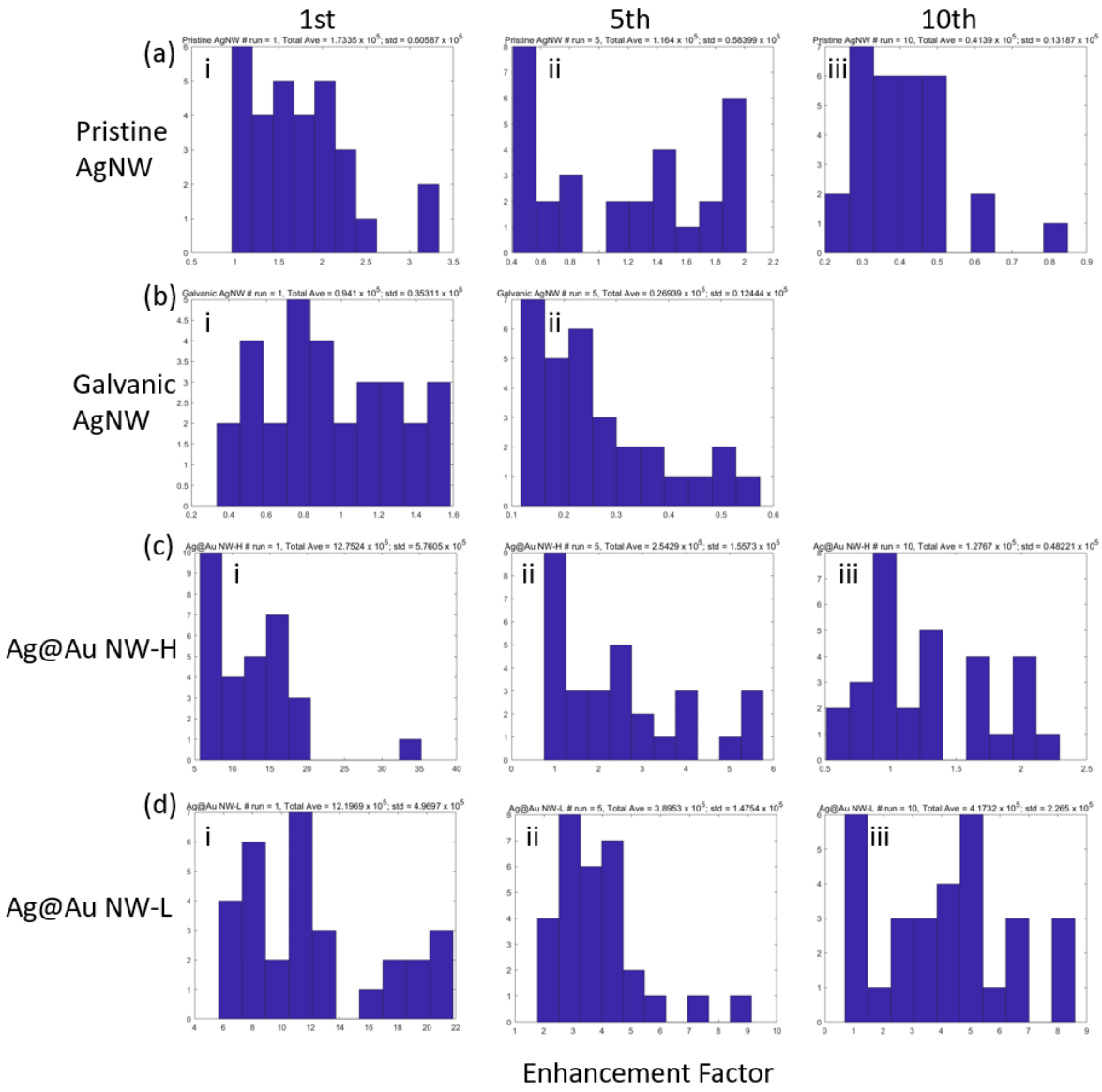

Figure 2-A10. Histogram of EF shown in figure 4: (a) pristine AgNW; (b) Galvanic AgNW; (c) Ag@Au NW-H; (d) Ag@Au NW-L. In each figure: i, ii, and iii: histogram of EF of 1st, 5th and 10th mappings respectively.

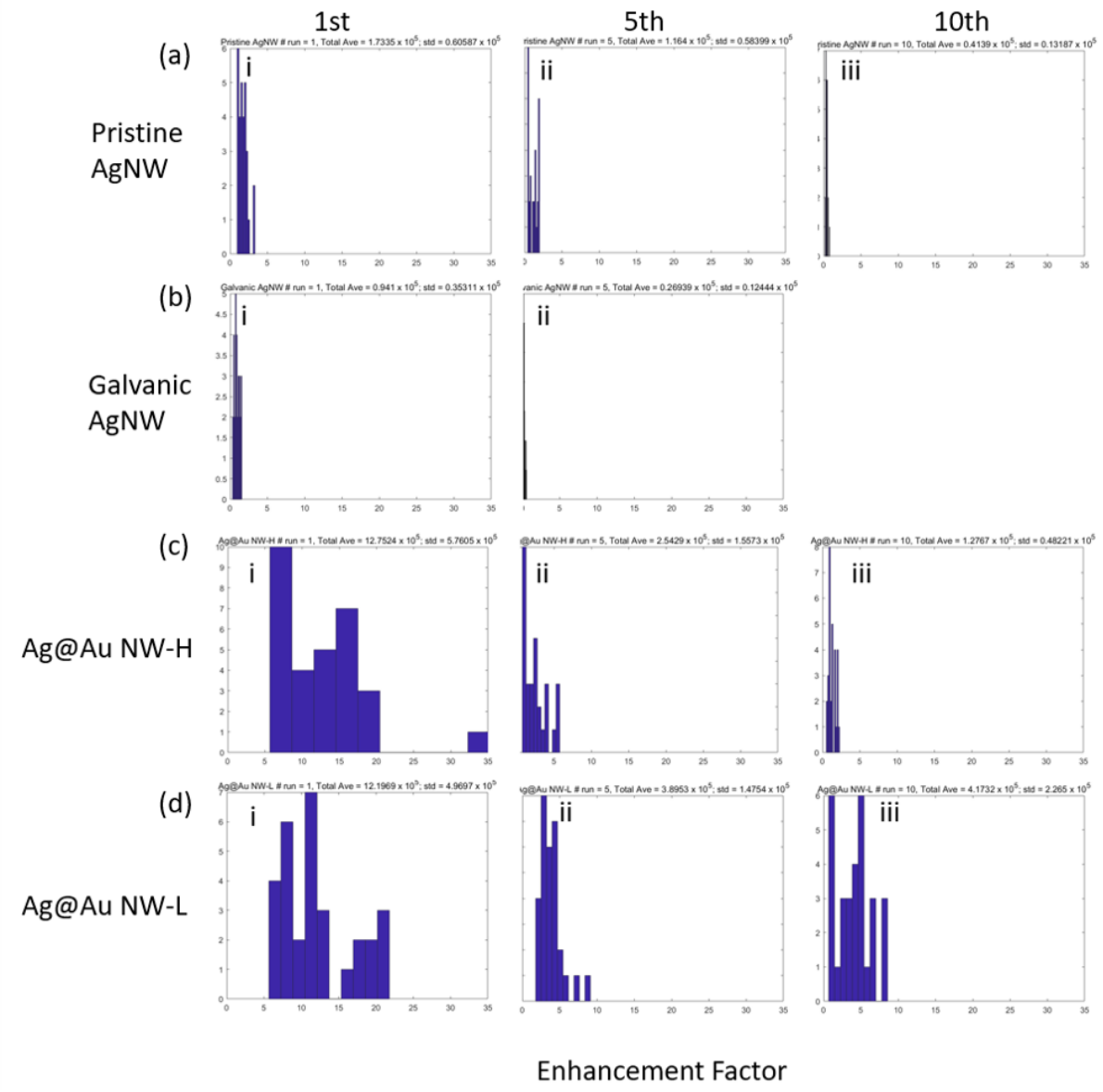

Figure 2-A11. Re-plot of Histogram of EF shown in figure S10 with the same rage of x axis: (a) pristine AgNW; (b) Galvanic AgNW; (c) Ag@Au NW-H; (d) Ag@Au NW-L. In each figure: i, ii, and iii: histogram of EF of 1st, 5th and 10th mappings respectively.

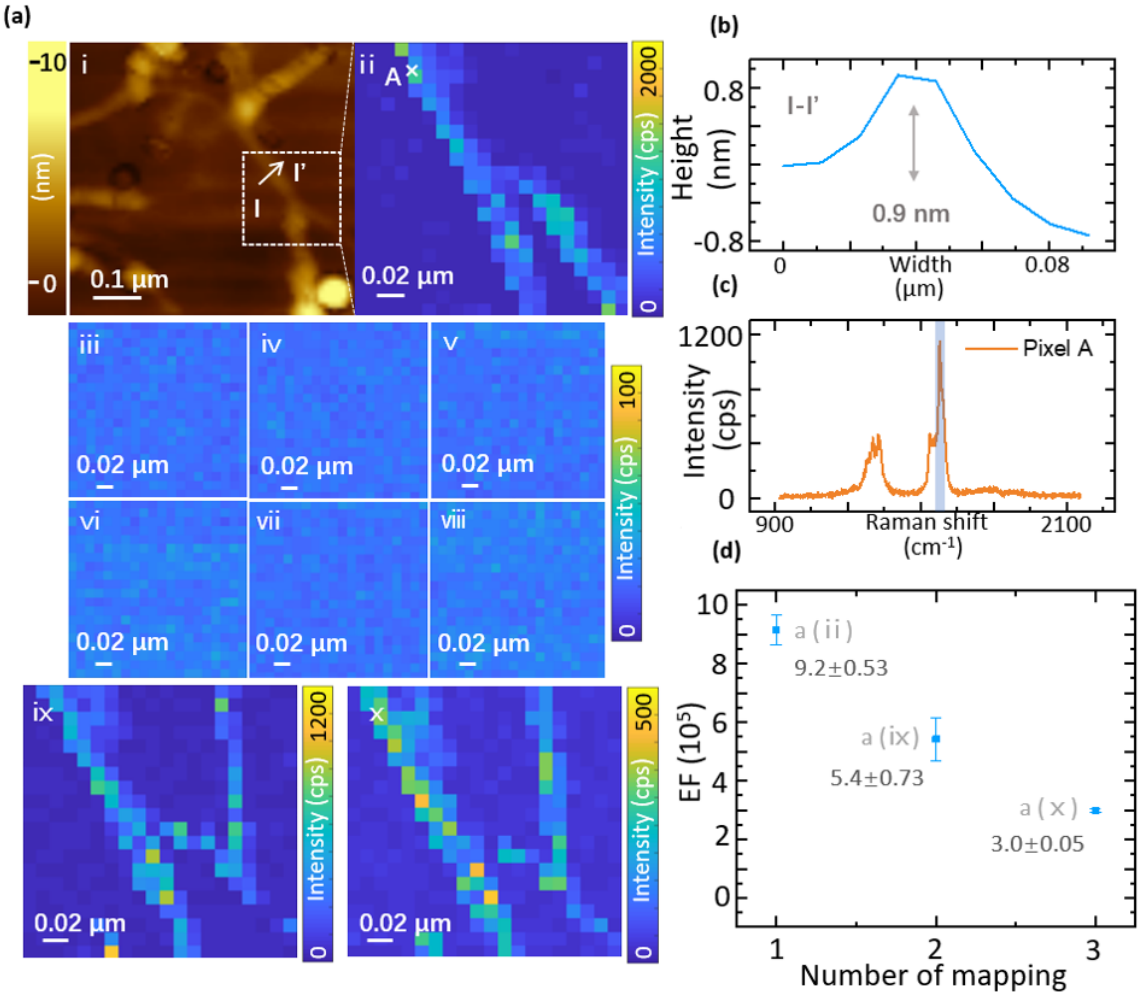

Figure 2-A12. Study of the effect of laser to EF using Ag@Au NW-H: (a) AFM image and TERS mapping: i: AFM image; ii 1st mapping under laser illumination; iii-viii: mappings without laser; ix: 2nd mapping with laser (8th mapping in total); x: 3rd mapping with laser (9th mapping in total); (b) line profile of CNT in (a)-i; (c) Raman spectrum of pixel A in ii; (d) EF of mappings with laser.

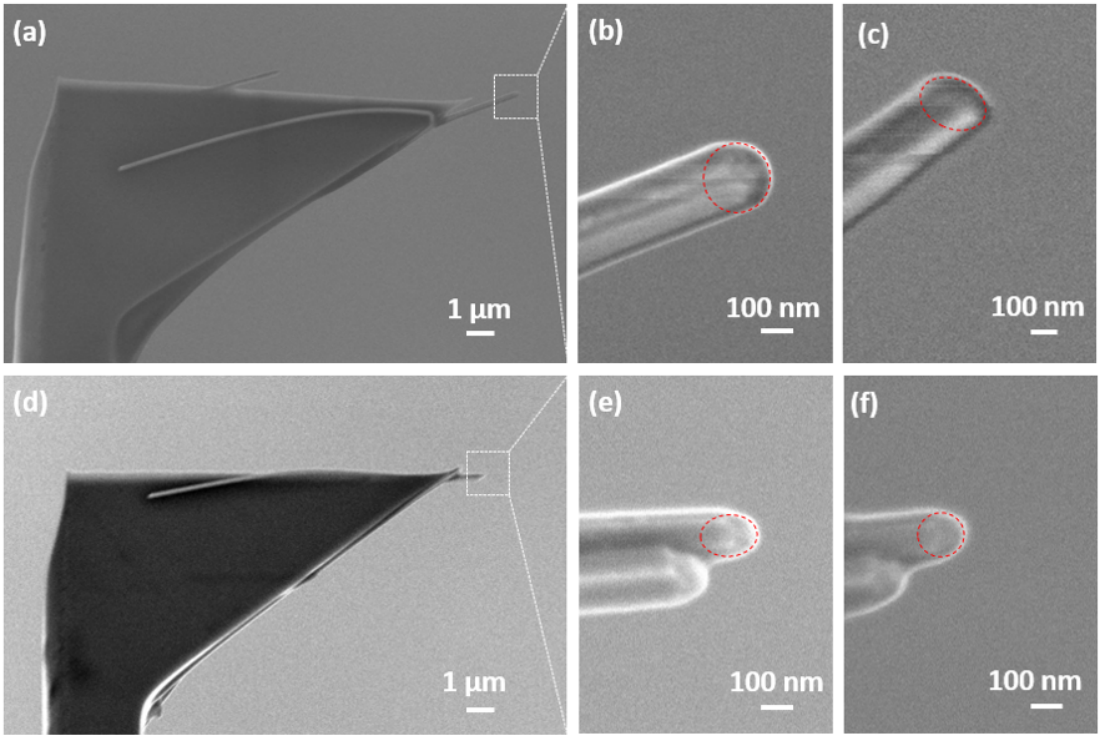

Figure 2-A13. Morphology change of Ag@Au NW-H: (a) Low magnification SEM image of probe 1; (b) high magnification SEM image before TERS measurement of probe 1; (c) high magnification SEM image after 10 mappings of TERS measurement of probe 1; (d) Low magnification SEM image of probe 2; (e) high magnification SEM image before TERS measurement of probe 2; (f) high magnification SEM image after 5 mappings of TERS measurement of probe 2.

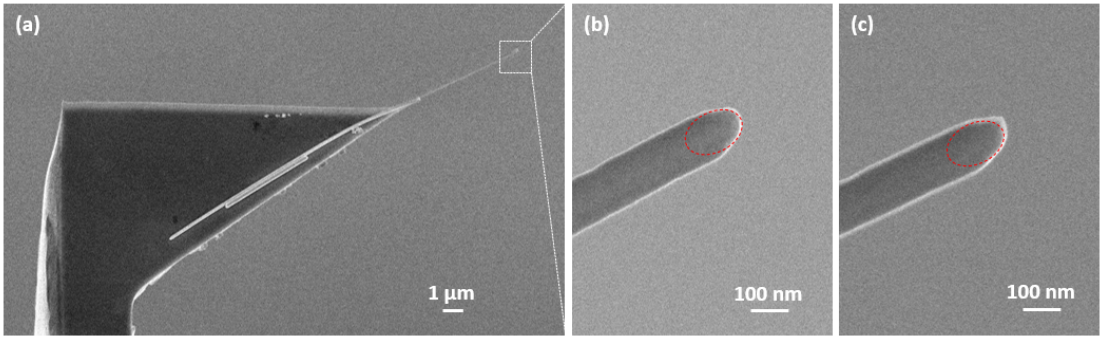

Figure 2-A14. Morphology change of Ag@Au NW-L: (a) Low magnification SEM image of probe; (b) high magnification SEM image before TERS measurement; (c) high magnification SEM image after 10 mappings of TERS.

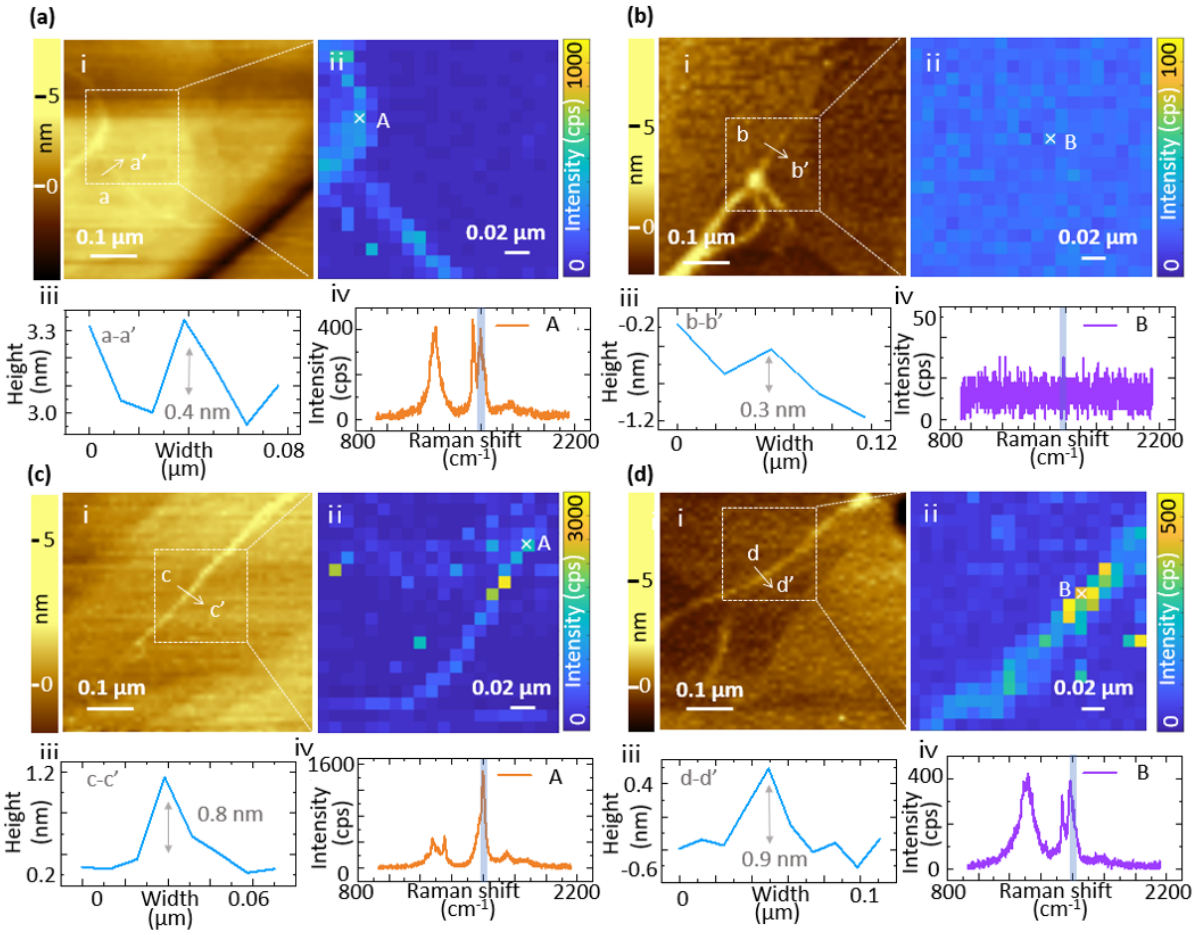

Figure 2-A15. Life time study of different TERS probes: (a) 1st mapping of pristine AgNW probe on the first day being prepared; (b) 1st mapping of the same pristine AgNW probe after one week (4th mapping in total); (c) 1st mapping of Ag@Au NW-L probe on the first day being prepared; (d) 1st mapping of the same Ag@Au NW-L probe after one week (4th mapping in total). In all subfigures,i refers to the AFM image; ii refers to the TERS mapping; iii refers to the line profile of the CNT in i; iv refers to the TERS spectra of the chosen pixel in ii. (Acquisition time was 0.4 s, accumulation once, 20×20 pixels (10 nm / pixel), Nf shift 80, laser power ~3.6 kW/cm^2, and the Raman intensity of G-band (cps) is selected to evaluate the TERS enhancement.

Table 2-A1. EF ($\times 10^5$) of three Ag@Au NW-L and three pristine AgNW probes at the first day (1~3) and after one week in air (4~6).

Mapping number		1st	2nd	3rd	4th	5th	6th
Ag@Au NW-L	P1	6.9	4.6	6.4	0.0	0.0	0.0
	P2	10.4	7.3	6.5	2.1	1.4	1.2
	P3	7.7	3.9	3.8	1.8	2.0	1.6
Pristine AgNW	P'1	3.3	1.1	0.9	0.18	0.18	0.17
	P'2	2.9	1.7	1.4	0.0	0.0	0.0
	P'3	1.7	1.0	0.7	0.0	0.0	0.0

Fitting of fig. 4

Based on equation 2-A0, the equation 2-A1 to 2-A4 show the fitting results for pristine AgNW, Au-etched AgNW, Ag@Au NW-H and Ag@Au NW-L respectively. where EF refers to enhancement factor ($\times 10^5$) and n refers to TERS mapping numbers, m_i to number of maps to reach EF ~ 1/e.

$$EF = \sum_{i=1}^{1\ or\ 2} exp\left(-{}^{n}/_{m_i}\right) \qquad 2-A0$$

$$EF = 2.1 \cdot e^{-\frac{n}{7.5}} \qquad 2-A1$$

$$EF = 1.2 \cdot e^{-\frac{n}{3}} \qquad 2-A2$$

$$EF = 18.9 \cdot e^{-\frac{n}{1.4}} + 4.2 \cdot e^{-\frac{n}{7.4}} \qquad 2-A3$$

$$EF = 31.7 \cdot e^{-\frac{n}{0.63}} + 6.1 \cdot e^{-\frac{n}{17.9}} \qquad 2-A4$$

Calculation of EF

The calculation method is shown in equations 2-A5 and 2-A6. C_{TERS} refers to TERS contrast, in which I_{TERS} and $I_{Far\text{-}Field}$ are the Raman intensity enhanced by near field and the intensity of normal far-field Raman. Here, the Raman intensity of G-band is picked as I_{TERS} since it is relatively stable and not affected by defect spots on the CNT, $I_{Far\text{-}Field}$ was measured under high laser power (~143 kW/cm^2) since it is almost impossible to obtain Raman signal with acceptable signal-to-noise ratio under same low laser power as TERS. Then, as the Raman

signal is proportional to the laser power, the Raman signal is calculated by proportional compensating power difference. In equation 2-A6, $A_{Far\text{-}Field}$ and $A_{Near\text{-}Field}$ refer to the area of far-field and near-field, respectively. The area of far-field can be easily calculated as the area of laser diffraction-limited focal spot by: diameter = 1.22 λ / NA. However, the area of the near-field is hard to estimate, which is commonly calculated by numerical simulation. Nevertheless, the validity of simulation is limited since multiple assumptions are necessary. Here, the enhancing area is estimated by the TERS resolution, which is reported to be below 15 nm[25], and in this experiment, 10 nm is regarded as the TERS resolution.

$$C_{TERS} = \frac{I_{TERS} - I_{Far-Field}}{I_{Far-Field}} \qquad 2-A5$$

$$EF = C_{TERS} \cdot \frac{A_{Far-Field}}{A_{Near-Field}} \qquad 2-A6$$

2.7 References

(1) Stöckle, R. M.; Suh, Y. D.; Deckert, V.; Zenobi, R. Nanoscale chemical analysis by tip-enhanced Raman spectroscopy. *Chemical Physics Letters* **2000**, *318* (1), 131-136. DOI: https://doi.org/10.1016/S0009-2614(99)01451-7.

(2) Anderson, M. S. Locally enhanced Raman spectroscopy with an atomic force microscope. *Applied Physics Letters* **2000**, *76* (21), 3130-3132. DOI: 10.1063/1.126546 (acccessed 2021/06/21).

(3) Hayazawa, N.; Inouye, Y.; Sekkat, Z.; Kawata, S. Metallized tip amplification of near-field Raman scattering. *Optics Communications* **2000**, *183* (1), 333-336. DOI: https://doi.org/10.1016/S0030-4018(00)00894-4.

(4) Kazemi-Zanjani, N.; Kergrene, E.; Liu, L.; Sham, T.-K.; Lagugné-Labarthet, F. Tip-Enhanced Raman Imaging and Nano Spectroscopy of Etched Silicon Nanowires. *Sensors* **2013**, *13* (10). DOI: 10.3390/s131012744.

(5) Marquestaut, N.; Talaga, D.; Servant, L.; Yang, P.; Pauzauskie, P.; Lagugné-Labarthet, F. Imaging of single GaN nanowires by tip-enhanced Raman spectroscopy. *Journal of Raman Spectroscopy* **2009**, *40* (10), 1441-1445, https://doi.org/10.1002/jrs.2404. DOI: https://doi.org/10.1002/jrs.2404 (acccessed 2021/06/21).

(6) Ogawa, Y.; Yuasa, Y.; Minami, F.; Oda, S. Tip-enhanced Raman mapping of a single Ge nanowire. *Applied Physics Letters* **2011**, *99* (5), 053112. DOI: 10.1063/1.3621856 (acccessed 2021/06/21).

(7) Peica, N.; Thomsen, C.; Maultzsch, J. Studying the local character of Raman features of single-walled carbon nanotubes along a bundle using TERS. *Nanoscale Research Letters* **2011**, *6* (1), 174. DOI: 10.1186/1556-276X-6-174.

(8) Park, K.-D.; Khatib, O.; Kravtsov, V.; Clark, G.; Xu, X.; Raschke, M. B. Hybrid Tip-Enhanced Nanospectroscopy and Nanoimaging of Monolayer WSe2 with Local Strain Control. *Nano Letters* **2016**, *16* (4), 2621-2627. DOI: 10.1021/acs.nanolett.6b00238.

(9) Pashaee, F.; Sharifi, F.; Fanchini, G.; Lagugné-Labarthet, F. Tip-enhanced Raman spectroscopy of graphene-like and graphitic platelets on ultraflat gold nanoplates. *Physical Chemistry Chemical Physics* **2015**, *17* (33), 21315-21322, 10.1039/C4CP05252H. DOI: 10.1039/C4CP05252H.

(10) Su, W.; Kumar, N.; Spencer, S. J.; Dai, N.; Roy, D. Transforming bilayer MoS2 into single-layer with strong photoluminescence using UV-ozone oxidation. *Nano Research* **2015**, *8* (12), 3878-3886. DOI: 10.1007/s12274-015-0887-7.

(11) Voronine, D. V.; Lu, G.; Zhu, D.; Krayev, A. Tip-Enhanced Raman Scattering of MoS2. *IEEE Journal of Selected Topics in Quantum Electronics* **2017**, *23* (1), 138-143. DOI: 10.1109/JSTQE.2016.2584784.

(12) Kumar, N.; Stephanidis, B.; Zenobi, R.; Wain, A. J.; Roy, D. Nanoscale mapping of catalytic activity using tip-enhanced Raman spectroscopy. *Nanoscale* **2015**, *7* (16), 7133-7137, 10.1039/C4NR07441F. DOI: 10.1039/C4NR07441F.

(13) Picardi, G.; Królikowska, A.; Yasukuni, R.; Chaigneau, M.; Escude, M.; Mourier, V.; Licitra, C.; Ossikovski, R. Exchange of Methyl- and Azobenzene-Terminated Alkanethiols on Polycrystalline Gold Studied by Tip-Enhanced Raman Mapping. *ChemPhysChem* **2014**, *15* (2), 276-282, https://doi.org/10.1002/cphc.201300918. DOI: https://doi.org/10.1002/cphc.201300918 (acccessed 2021/06/21).

(14) Xue, L.; Li, W.; Hoffmann, G. G.; Goossens, J. G. P.; Loos, J.; de With, G. High-Resolution Chemical Identification of Polymer Blend Thin Films Using Tip-Enhanced Raman Mapping. *Macromolecules* **2011**, *44* (8), 2852-2858. DOI: 10.1021/ma101651r.

(15) Gucciardi, P. G.; Valmalette, J.-C. Different longitudinal optical—transverse optical mode amplification in tip enhanced Raman spectroscopy of GaAs(001). *Applied Physics Letters* **2010**, *97* (26), 263104. DOI: 10.1063/1.3532841 (acccessed 2021/06/21).

(16) Sheremet, E.; Milekhin, A. G.; Rodriguez, R. D.; Weiss, T.; Nesterov, M.; Rodyakina, E. E.; Gordan, O. D.; Sveshnikova, L. L.; Duda, T. A.; Gridchin, V. A.; et al. Surface- and tip-enhanced resonant Raman scattering from CdSe nanocrystals. *Physical Chemistry Chemical Physics* **2015**, *17* (33), 21198-21203, 10.1039/C4CP05087H. DOI: 10.1039/C4CP05087H.

(17) VandenAkker, C. C.; Schleeger, M.; Bruinen, A. L.; Deckert-Gaudig, T.; Velikov, K. P.; Heeren, R. M. A.; Deckert, V.; Bonn, M.; Koenderink, G. H. Multimodal Spectroscopic Study of Amyloid Fibril Polymorphism. *The Journal of Physical Chemistry B* **2016**, *120* (34), 8809-8817. DOI: 10.1021/acs.jpcb.6b05339.

(18) Kurouski, D.; Deckert-Gaudig, T.; Deckert, V.; Lednev, Igor K. Surface Characterization of Insulin Protofilaments and Fibril Polymorphs Using Tip-Enhanced Raman Spectroscopy (TERS). *Biophysical Journal* **2014**, *106* (1), 263-271. DOI: https://doi.org/10.1016/j.bpj.2013.10.040.

(19) Cialla, D.; Deckert-Gaudig, T.; Budich, C.; Laue, M.; Möller, R.; Naumann, D.; Deckert, V.; Popp, J. Raman to the limit: tip-enhanced Raman spectroscopic investigations of a single tobacco mosaic virus. *Journal of Raman Spectroscopy* **2009**, *40* (3), 240-243, https://doi.org/10.1002/jrs.2123. DOI: https://doi.org/10.1002/jrs.2123 (acccessed 2021/06/21).

(20) Neugebauer, U.; Rösch, P.; Schmitt, M.; Popp, J.; Julien, C.; Rasmussen, A.; Budich, C.; Deckert, V. On the Way to Nanometer-Sized Information of the Bacterial Surface by Tip-Enhanced Raman Spectroscopy. *ChemPhysChem* **2006**, *7* (7), 1428-1430,

https://doi.org/10.1002/cphc.200600173. DOI: https://doi.org/10.1002/cphc.200600173 (acccessed 2021/06/21).

(21) Olschewski, K.; Kämmer, E.; Stöckel, S.; Bocklitz, T.; Deckert-Gaudig, T.; Zell, R.; Cialla-May, D.; Weber, K.; Deckert, V.; Popp, J. A manual and an automatic TERS based virus discrimination. *Nanoscale* **2015**, *7* (10), 4545-4552, 10.1039/C4NR07033J. DOI: 10.1039/C4NR07033J.

(22) Walke, P.; Toyouchi, S.; Wolf, M.; Peeters, W.; Prabhu, S. R.; Inose, T.; De Feyter, S.; Fujita, Y.; Uji-i, H. Facilitating Tip-Enhanced Raman Scattering on Dielectric Substrates via Electrical Cutting of Silver Nanowire Probes. *The Journal of Physical Chemistry Letters* **2018**, *9* (24), 7117-7122. DOI: 10.1021/acs.jpclett.8b03189.

(23) Fujita, Y.; Walke, P.; De Feyter, S.; Uji-i, H. Tip-enhanced Raman scattering microscopy: Recent advance in tip production. *Japanese Journal of Applied Physics* **2016**, *55* (8S1), 08NA02. DOI: 10.7567/jjap.55.08na02.

(24) Zhang, R.; Zhang, Y.; Dong, Z. C.; Jiang, S.; Zhang, C.; Chen, L. G.; Zhang, L.; Liao, Y.; Aizpurua, J.; Luo, Y.; et al. Chemical mapping of a single molecule by plasmon-enhanced Raman scattering. *Nature* **2013**, *498* (7452), 82-86. DOI: 10.1038/nature12151.

(25) Walke, P.; Fujita, Y.; Peeters, W.; Toyouchi, S.; Frederickx, W.; De Feyter, S.; Uji-i, H. Silver nanowires for highly reproducible cantilever based AFM-TERS microscopy: towards a universal TERS probe. *Nanoscale* **2018**, *10* (16), 7556-7565, 10.1039/C8NR02225A. DOI: 10.1039/C8NR02225A.

(26) Asghari-Khiavi, M.; Wood, B. R.; Hojati-Talemi, P.; Downes, A.; McNaughton, D.; Mechler, A. Exploring the origin of tip-enhanced Raman scattering; preparation of efficient TERS probes with high yield. *Journal of Raman Spectroscopy* **2012**, *43* (2), 173-180, https://doi.org/10.1002/jrs.3021. DOI: https://doi.org/10.1002/jrs.3021 (acccessed 2021/06/23).

(27) Taguchi, A.; Hayazawa, N.; Saito, Y.; Ishitobi, H.; Tarun, A.; Kawata, S. Controlling the plasmon resonance wavelength in metal-coated probe using refractive index modification. *Opt. Express* **2009**, *17* (8), 6509-6518. DOI: 10.1364/OE.17.006509.

(28) Shi, X.; Coca-López, N.; Janik, J.; Hartschuh, A. Advances in Tip-Enhanced Near-Field Raman Microscopy Using Nanoantennas. *Chemical Reviews* **2017**, *117* (7), 4945-4960. DOI: 10.1021/acs.chemrev.6b00640.

(29) Schmid, T.; Opilik, L.; Blum, C.; Zenobi, R. Nanoscale Chemical Imaging Using Tip-Enhanced Raman Spectroscopy: A Critical Review. *Angewandte Chemie International Edition* **2013**, *52* (23), 5940-5954, https://doi.org/10.1002/anie.201203849. DOI: https://doi.org/10.1002/anie.201203849 (acccessed 2021/06/23).

(30) Yang, M.; Hood, Z. D.; Yang, X.; Chi, M.; Xia, Y. Facile synthesis of Ag@Au core–sheath nanowires with greatly improved stability against oxidation. *Chemical Communications* **2017**, *53* (12), 1965-1968, 10.1039/C6CC09878A. DOI: 10.1039/C6CC09878A.

(31) Rycenga, M.; Cobley, C. M.; Zeng, J.; Li, W.; Moran, C. H.; Zhang, Q.; Qin, D.; Xia, Y. Controlling the Synthesis and Assembly of Silver Nanostructures for Plasmonic Applications. *Chemical Reviews* **2011**, *111* (6), 3669-3712. DOI: 10.1021/cr100275d.

(32) Korte, K. E.; Skrabalak, S. E.; Xia, Y. Rapid synthesis of silver nanowires through a CuCl- or CuCl2-mediated polyol process. *Journal of Materials Chemistry* **2008**, *18* (4), 437-441, 10.1039/B714072J. DOI: 10.1039/B714072J.

(33) Gierhart, B. C.; Howitt, D. G.; Chen, S. J.; Smith, R. L.; Collins, S. D. Frequency Dependence of Gold Nanoparticle Superassembly by Dielectrophoresis. *Langmuir* **2007**, *23* (24), 12450-12456. DOI: 10.1021/la701472y.

(34) Fortuni, B.; Inose, T.; Uezono, S.; Toyouchi, S.; Umemoto, K.; Sekine, S.; Fujita, Y.; Ricci, M.; Lu, G.; Masuhara, A.; et al. In situ synthesis of Au-shelled Ag nanoparticles on PDMS for flexible, long-life, and broad spectrum-sensitive SERS substrates. *Chemical Communications* **2017**, *53* (82), 11298-11301, 10.1039/C7CC05420C. DOI: 10.1039/C7CC05420C.

(35) Schulze, H. G.; Foist, R. B.; Okuda, K.; Ivanov, A.; Turner, R. F. B. A Small-Window Moving Average-Based Fully Automated Baseline Estimation Method for Raman Spectra. *Applied Spectroscopy* **2012**, *66* (7), 757-764. DOI: 10.1366/11-06550 (acccessed 2021/07/04).

(36) Yang, Y.; Liu, J.; Fu, Z.-W.; Qin, D. Galvanic Replacement-Free Deposition of Au on Ag for Core–Shell Nanocubes with Enhanced Chemical Stability and SERS Activity. *Journal of the American Chemical Society* **2014**, *136* (23), 8153-8156. DOI: 10.1021/ja502472x.

(37) Lee, H.; Hong, S.; Lee, J.; Suh, Y. D.; Kwon, J.; Moon, H.; Kim, H.; Yeo, J.; Ko, S. H. Highly Stretchable and Transparent Supercapacitor by Ag–Au Core–Shell Nanowire Network with High Electrochemical Stability. *ACS Applied Materials & Interfaces* **2016**, *8* (24), 15449-15458. DOI: 10.1021/acsami.6b04364.

(38) Li, Y.; Lin, H.; Zhou, W.; Sun, L.; Samanta, D.; Mirkin, C. A. Corner-, edge-, and facet-controlled growth of nanocrystals. *Science Advances* **2021**, *7* (3), eabf1410. DOI: 10.1126/sciadv.abf1410.

(39) Cui, Y.; Ren, B.; Yao, J.-L.; Gu, R.-A.; Tian, Z.-Q. Synthesis of AgcoreAushell Bimetallic Nanoparticles for Immunoassay Based on Surface-Enhanced Raman Spectroscopy. *The Journal of Physical Chemistry B* **2006**, *110* (9), 4002-4006. DOI: 10.1021/jp056203x.

(40) Fan, M.; Lai, F.-J.; Chou, H.-L.; Lu, W.-T.; Hwang, B.-J.; Brolo, A. G. Surface-enhanced Raman scattering (SERS) from Au:Ag bimetallic nanoparticles: the effect of the molecular probe. *Chemical Science* **2013**, *4* (1), 509-515, 10.1039/C2SC21191B. DOI: 10.1039/C2SC21191B.

(41) Ling, L.; Xu, M.-M.; Gu, R.-A.; Yao, J.-L. Preparation of $Ag_{core}Au_{shell}$ Nanowires and Their Surface Enhanced Raman Spectroscopic Studies. *Acta Chimica Sinica* **2007**, *65* (9), 779-784.

Chapter 3 Length-Controllable Gold-coated Silver Nanowire Probes for High AFM-TERS Scattering Activity

The results reported in this chapter are based on the following publication:

Wen, H.; Li, J.; Zhang, Q.; Inose, T.; Peeters, W.; Fortuni, B.; Asakawa, H.; Masuhara, A.; Hirai, K.; Toyouchi, S.; Fujita, Y.; Uji-i, H. Length Controllable Gold-coated Silver Nanowire Probes for High AFM-TERS activity. *Nano Letters* **2022**, *in press*. DOI: 10.1021/acs.nanolett.2c03985.

3.1 Abstract

Tip-enhanced Raman scattering (TERS) microscopy is an advanced technique for investigation at the nanoscale to provide topographic and chemical information simultaneously. The TERS probe plays a crucial role in the microscopic performance. In the recent past, the development of silver nanowire (AgNW)-based TERS probes solved the main tip fabrication issues, such as low mechanical strength and reproductivity. However, this fabrication method still suffers from the low control of the protruded length of AgNW. In this work, a simple water-air interface electro-cutting method is proposed to achieve wide controllability of the length. This water-cut method was combined with the succedent Au coating on AgNW surface after cutting, which achieved up to 100 times higher EF and two times smaller spatial resolution than pristine AgNW. Thanks to this excellent EF, the water-cut Au-coated AgNW probes were found to possess high TERS activity even in non-gap mode, allowing for broader applications.

3.2 Introduction

Tip-enhanced Raman scattering (TERS) microscopy is a powerful nano-optical technique that enables site-specific characterization of both topographic and chemical information with the spatial resolution overstepping the diffraction limit of light.[1, 2] With the continuous development of TERS in these two decades, this highly sensitive, non-invasive, and label-free technique can be performed on diversified fields under various environments.[2-8] In principle, TERS microscopy is the combination of Raman spectroscopy and scanning probe microscopies (SPMs), including scanning tunneling microscope (STM), shear force microscopy (SFM), and atomic force microscope (AFM),[9] among which the AFM-based TERS is more widely used as being more stable, faster, and having no intrinsic substrate limitations.[10]

In a TERS system, the metalized scanning probe is the crucial part, as determining the TERS performance. When the polarized laser light focuses on the apex of the probe, the excitation of the localized surface plasmons (LSPs) generates a nanoconfined near-field electromagnetic (EM) field.[11] Because the Raman scattering can be significantly enhanced at the apex, the spatial resolution is determined by the confinement size of LSPs, which depends on the morphology of the apex. A typical spatial resolution can reach 10 ~ 20 nm,[12, 13] while to study the structural information within 10 nm or even sub-nano scale is desired in many frontier fields, which requires further improvement in the spatial resolution. Commonly, the vacuum-evaporation of noble metal is used as the fabrication method of AFM-based TERS probes due to its large-scale fabrications nature.[14, 15] On the other hand, this approach suffers from low reproductivity and low mechanical strength, leading to short lifetime, and eventually high fabrication costs.[16, 17] To address these issues, silver nanowire (AgNW)-based AFM-TERS probes were proposed as an easy bottom-up fabrication method,[10] which achieves a well-controlled apex morphology, outstanding optical coupling property, and high TERS reproducibility due to the high homogeneity of the chemically synthesized AgNW. However, the AC-dielectrophoresis (AC-DEP)-based AFM-TERS probe fabrication, previously reported by our team, exhibits very low controllability of the length of the attached AgNW. Indeed, by using AC-DEP, the attachment of AgNW(s) on the AFM cantilever is completely random, generating various lengths between 2 μm and 20 μm. Whereas, less than 5 μm of the protruded length of the attached AgNW is required to maintain stable TERS measurement. Consequently, the attachment of AgNW usually needs to be repeated until a suitable protruded length is achieved. Besides the low length controllability, the pristine AgNW previously used could

reach a reasonably high enhancement factor (EF), up to the order of 10^5, and a spatial resolution of ~10 nm. Nevertheless, higher EF is always desired for sensitive target samples and a higher spatial resolution would offer deeper understanding of the samples' nanoscale nature. In addition, current TERS technique mainly realized by the so-called 'gap-mode', which requires to use metal substrate. To broaden the application of TERS, developing 'non-gap mode' is promising. However, realizing 'non-gap mode' is a technical barrier.

In this contribution, a simple fabrication method using electro-cutting of AgNW at air-liquid interface followed by Au-coating is proposed, which provides (i) a great controllability of protruded AgNW length, (ii) an outstanding EF, and (iii) a better spatial resolution. To enable the controllability of the protruded length of AgNW, an AgNW with random length on the AFM cantilever is cut at the air-liquid interface by applying AC electric fields. Thereafter, to improve EF and spatial resolution, the cut AgNW is coated by Au layers by plating them under alkaline conditions. The obtained Au-coated cut AgNW probes exhibit an EF over 10^7 with the spatial resolution as high as 5 nm at the gap mode. Thanks to its desired features, the cut probe possessed high activity even on non-plasmonic substrate such as a silicon substrate (non-gap mode), achieving an EF of 10^5.

3.3 Experiment section

Materials

Silver nitrate ($AgNO_3$), tetrachloroauric (III) acid (HAuCl4), ethylene glycol (EG, anhydrous, 99.8%), and hydrochloric acid (HCl) were obtained from SIGMA–ALDRICH. Copper chloride ($CuCl_2$) and polyvinylpyrrolidone K30 (PVP), sodium hydroxide (NaOH), isopropanol (IPA), tetrahydrofuran (THF) and toluene (TOL) were purchased from FUJIFILM Wako Pure Chemical Corporation. Single wall carbon nanotubes (CNTs) were purchased from SIGMA-ALDRICH. All chemicals were used without further purification.

Silver nanowire synthesis

AgNWs were synthesized according to the polyol method[18, 19] with some modifications. Briefly, 0.07 mg of PVP was dissolved in 9.66 mL of EG and heated at 160 °C for 3 hours under magnetic stirring (600 rpm). Then, 80 µL of $CuCl_2$ solution in EG (4 mM) was added to the solution under higher speed stirring (1,000 rpm) for 10 min, followed by the addition of 150 µL of $AgNO_3$ solution in EG (0.12 M). After the color of the solution turned greenish, 4.85 mL of $AgNO_3$ solution in EG (0.12 M) was added drop-wise at a rate of 150 µL/min. Thereafter, the mixture was maintained at 160°C for 2 hours under stirring (600 rpm). Finally, the mixture was cooled down to room temperature, obtaining high-yield AgNWs. These NWs were then washed three times with IPA. A typical SEM image of the final product is shown in Fig. 3-1.

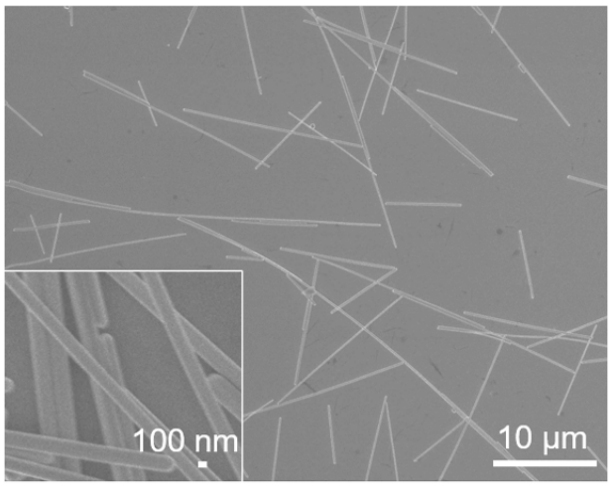

Figure 3-1. SEM image of pristine AgNW

Fabrication of silver nanowire functionalized AFM tip

The probe fabrication follows the reported AC-dielectrophoresis method.[10, 11, 20] The apex of Micro AFM cantilevers (160AC-NA, OPUS) was dipped into a droplet of AgNWs that typically contains approximately 5 µL of diluted AgNW IPA solution (~40 µg/mL) with 25 µL of Milli-Q water. A 1 MHz square wave with 14 V_{p-p} and 0 V DC offset with 50% duty cycle provided by a function generator was applied for usually 0.5-3 s between the cantilever and the droplet to achieve the nanowire attachment.

Cutting of silver nanowire at liquid-air interface

The apex of the AgNW attached on a Micro AFM cantilever was dipped into a droplet of PVP Milli-Q water solution (15 mg/mL) with less than 5 µm of the protruded length outside the liquid surface. A 1 kHz square wave with 20 V_{p-p} and +4 V DC offset to the cantilever with 50% duty cycle provided by a function generator was applied for usually 0.5-2 s between the cantilever and the droplet to achieve the nanowire cutting, as shown in Fig. 3-2a.

Au modification on the cut silver nanowire TERS probe

0.3 mL $HAuCl_4$ (1 µM/ 10 µM/ 100 µM) and 0.125 mL NaOH (10 mM) were added into 0.625 mL MilliQ water, with the final concentration of gold were ~0.3 µM/ 3 µM/ 30 µM respectively. And 0.3 mL $HAuCl_4$ (10 µM) was added to 0.75 mL MilliQ water. Then, the cut TERS probes were dipped into these modification solutions respectively for ~ 1 min, as shown in Fig. 3-2b.

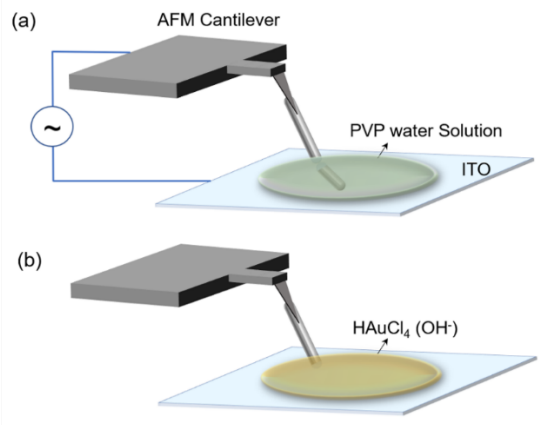

Figure 3-2. Schematic illustration of the fabrication of (a) the water-cut AgNW-based TERS probe; (b) Au modification of the water-cut AgNW-based TERS probe.

Preparation of CNT on au (111)

Au (111) substrates purchased from PHASIS (Switzerland) were first rinsed with acetone, ethanol, and Milli-Q and brow dried by N_2. The substrate was then flame annealed with a piezo gas burner for a few seconds to remove contaminations and then cooled under N_2 atmosphere. CNTs was dispersed in 5 mL THF and treated by ultrasonication for several hours. The CNT suspension was diluted 5 times (~12 μg/mL) and then dispersed by ultrasonication for several hours again. The dispersed CNT solution was drop-casted onto the prepared substrate, followed by rinsing with Milli-Q and brow drying by N_2. This step was repeated by a few times until the coverage of CNTs became sufficient for TERS measurement. Some properties of the single wall carbon nanotubes (CNTs) are shown in Tab. 3-1, and more detailed information such as the typical thermogravimetric analysis, typical chirality distribution, and typical optical absorbance (OA) analysis can be found from SIGMA–ALDRICH.[21]

Table 3-1. Properties of the single walled carbon nanotube.[21]

Average Diameter (NIRF)	0.83 nm
Median Length (AFM)	1 μm
Bulk Density (ASTM D7481)	0.1 g/cm^3
Moisture Content (TGA)	≤ 5 wt%
Specific Surface Area (BET)	≥ 700 m^2/g
G/D Ratio (Raman, 633 nm)	≥ 15

AFM/TERS Measurements

AFM/TERS measurements were carried out on an OmegaScope™ (AIST-NT, HORIBA) with a homemade optical platform, as shown in Fig. 3-3. Laser line from a He-Ne laser (632.8 nm, LASOS) was focused onto the sample/tip by an objective (MITUTOYO, M plan Apo 100×, N.A. 0.7) after passing through a half-wave plate (WPH05M-633, Thorlabs), a glan-laser calcite polarizer (GL5-A, Thorlabs) and being reflected by a dichroic mirror (LPD02-633RU, Semrock). The same objective was used to collect Raman scattering, and the collected scattering was directed through the dichroic mirror, a pinhole (diameter 100 μm), and a long-pass filter (LP02-633RE, Semrock) to a Raman spectrograph (iHR550, Horiba) equipped with a charge-coupled device (CCD) camera (Andor, Newton 920). Prior to TERS mapping, in order

to align the laser on the apex of the TERS probe, Rayleigh scattering mapping from AgNW was performed by objective scanning without the long-pass filter. All AFM/TERS measurements were performed under ambient conditions at room temperature. All TERS data were calibrated using Raman spectrum of toluene and implemented baseline subtraction by a model-free small window moving average-based baseline estimation method if necessary.[22] Omega software (AIST-NT/HORIBA), home-built routines in MATLAB (MathWorks), Igor Pro (WaveMetrics), and Origin (OriginLab) were used for data analysis.

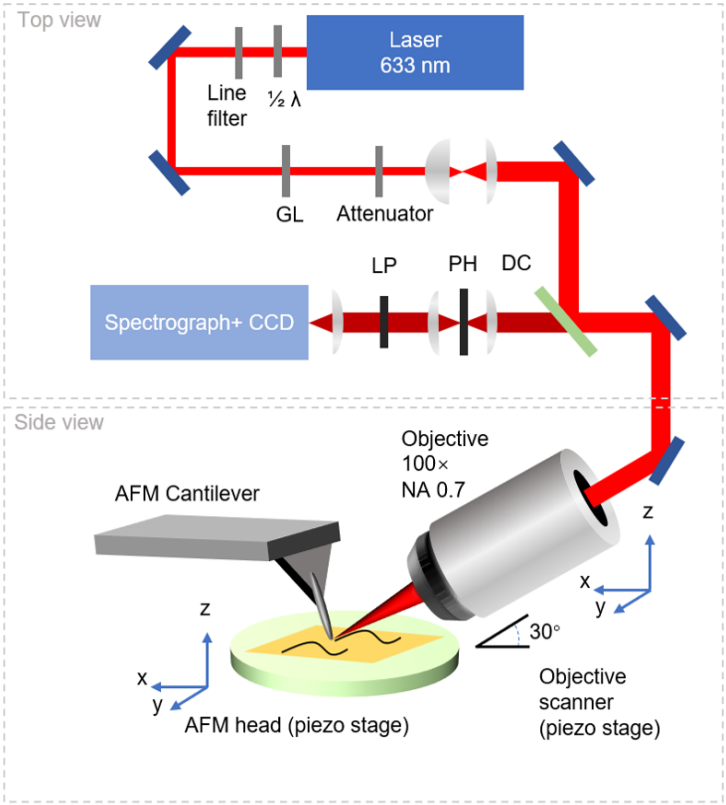

Figure 3-3. Schematic illustration of AFM-TERS setup. (λ/2: half-wave plate, GL: Glan-Laser calcite polarizer, LP: long-path filter, PH: pin hole, DC: dichroic mirror, respectively)

Characterization of AgNWs Functionalized TERS Probe

The morphology of the apex of the TERS probes functionalized by pristine AgNWs, cut AgNW, and Au-modified cut AgNWs was characterized by field-emission scanning electron microscopy (FE-SEM, JEOL JSM-6700FT at 5.0 kV and HITACHI SU8230 at 1.0 kV).

3.4 Result and discussion

Fabrication and characterization of length controllable AgNW based AFM-TERS probe

Scanning electron microscopy (SEM) and optical transmission images of the probe during the cutting are shown in Figure 3-4a to e, respectively. By the AC-DEP, dissociative pentagon-shaped AgNW with smooth surface morphology was functionalized to the apex of AFM cantilever, resulting in random protruded length, which could be even longer than 10 μm as shown in Figure 3-4a. Then, as shown in Figure 3-4b to d, the protruded AgNW was immersed in water containing polyvinylpyrrolidone (PVP) and cut at the air-liquid interface at suitable position by applying AC voltage. The cutting likely occurs due to AC electrothermal effect (ACET)[23], the shear stress induced by AC electric fields[24] and/or combination of these. The PVP introduced in the solution significantly enhances the performance of the cut probe, likely because of protection effect of the cross section of cut AgNW from oxidation. This process allows for the controlling of the length of TERS probe and the forming of cutting cross section as new apex (Fig. 3-4e).

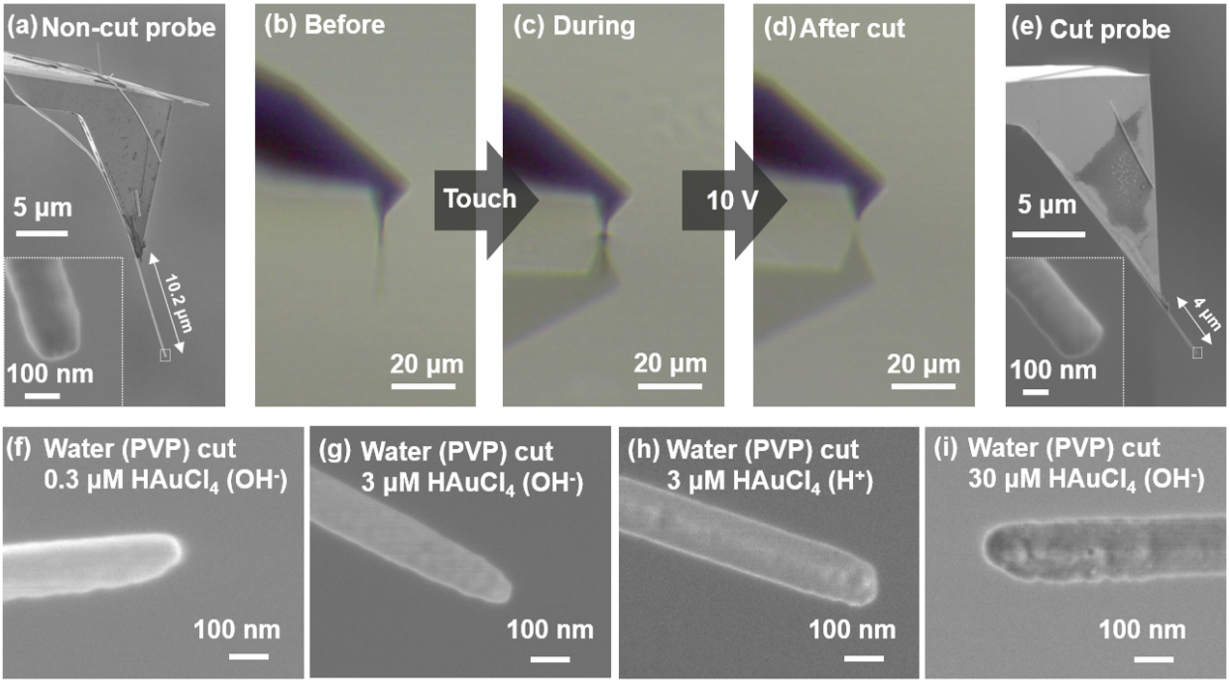

Figure 3-4. (a-e) TERS probe cutting procedure: (a) SEM image of the non-cut TERS probe; (b-d) Optical transmission images of the AgNW cutting procedure: (b) before; (c) during; (d) after; (e) SEM image of the water (PVP) cut TERS probe. For cutting, 1 kHz square wave with 10 V amplitude and 50% duty cycle at +4 V offset to the cantilever was used. (f-i) SEM images

of the apex of water (PVP) cut-Au modified AgNW AFM-TERS probe using 0.3 µM (f), 3 µM (g) and 30 µM (h) of $HAuCl_4$ at high pH, and 3 µM $HAuCl_4$ at low pH (i), respectively.

Simply immersing AgNWs in $HAuCl_4$ aqueous solution spontaneously induces a galvanic replacement reaction (GRR). GRR not only generates gold nanostructures on the AgNWs but also leads to void formation inside AgNWs, which would drastically improve the TERS performance of the probe.[20] In this regard, alkaline reaction conditions can be used to lower the reduction potential of the Au^{3+}, by converting $AuCl_4^-$ into $Au(OH)^{4-}$.[25, 26] In this way, the extent of the GRR can be restrained and the reaction is limited at AgNW surface (impeding void formation). Accordingly, the Au-coating after AgNW cutting was performed at pH 10 and different Au^{3+} concentrations were tested: 0.3, 3, and 30 µM (cut-AgAu-0.3-OH, cut-AgAu-3-OH, cut-AgAu-30-OH). For comparison, an Au coating at pH 5 with 3 µM of Au^{3+} was also accomplished (cut-AgAu-3-H). The SEM images of the obtained probes (Fig. 3-4f to i) did not show a significant difference in morphology at the apex of the cut AgNW for the different experimental conditions tested.

Evaluation of cut-AgNW TERS probes

As mentioned above, the durability, the EF and the spatial resolution are the key aspects to be evaluated when developing TERS probes. The durability is the major issue for AgNWs-based AFM-TERS probes. Indeed, exposing AgNW to the air and/or light is known to cause surface oxidation which quickly reduces TERS activity.[10, 20] In particular, under light irradiation, the local heating effect due to Ohmic loss of plasmons can accelerate surface oxidation and even lead to morphological changes on the probe apex.[20] On the other hand, the EF and the spatial resolution strongly depend on the substrate used for TERS measurements. Noble metal substrates, such as Au (111), generally provide high EF and better spatial resolution due to the excitation of a 'gap-mode' plasmon between the plasmonic probe and substrate. This substrate restriction could be overstepped when obtaining performant TERS probes, which would enable high-quality TERS measurements in dielectric substrates (non-gap mode). Considering this aspect, the performance of the cut Ag-Au probes prepared with different experimental conditions was evaluated both on an Au (111) (gap-mode) and on a silicon substrate (non-gap mode) in terms of durability (lifetime of the probes), spatial resolution and EF.

Gap-mode TERS

For the durability test, multiple TERS mappings were repeatedly conducted at the same single carbon nanotube (CNT) on Au (111) under the same measurement conditions (integration time and laser power). Fig. 3-5 shows gap-mode TERS maps of CNTs obtained by using a pristine AgNW (Fig. 3-5a), AgNW cut in PVP aqueous solution (Fig. 3-5b), cut-AgAu-3-H (Fig. 3-5c), cut-AgAu-0.3-OH (Fig. 3-5d), cut-AgAu-3-OH (Fig. 3-5e), and cut-AgAu-30-OH (Fig. 3-5f), respectively. Fig. 3-A1 shows the corresponding AFM topographic images and line profiles extracted from the TERS maps in Fig. 3-5. In each panel, i and ii refer to the first and 5th (2nd in f) TERS map of G-band out of 5 (2 in f) consecutive mappings, respectively, while iii refers to the TERS spectra at pixel A and B in the corresponding TERS maps, respectively. These TERS maps consist of 15 x 15 pixels (10 nm/pixel), in which Raman spectrum was taken at every pixel with an integration time of 0.2 s. In this way, TERS probes were continuously exposed to the laser excitation for ~ 45 s during one complete mapping, leading to a total exposure for at least 3.75 minutes over 5 mappings, excluding the lag time between consecutive mappings. Note that the laser focus position on the probe apex was realigned between each consecutive mapping in order to rule out the effect of optical misalignment due to thermal drift of the optics / probe. For this alignment, the laser power was reduced by further 100 times compared to the mapping condition to avoid extra light-induced damage.

At the 1st TERS map with freshly prepared TERS probes, water (PVP) cut (b) and cut-AgAu-3-OH (e) probes show relatively high Raman intensity (1000 ~ 8000 cps at G-band) compared to the pristine (a) and cut-AgAu-0.3-OH (d) (100 ~ 350 cps at G-band). For all four kinds of probes in Fig. 3-5a, b, d, e, 5 mappings could be completed, which indicates high durability towards practical applications. As for cut-AgAu-3-H and cut-AgAu-30-OH probes (Fig. 3-5c and f), both show short probe lifetime and poor TERS activity. This limited TERS performance may arise from a greater extent of GRR reactions.[26]

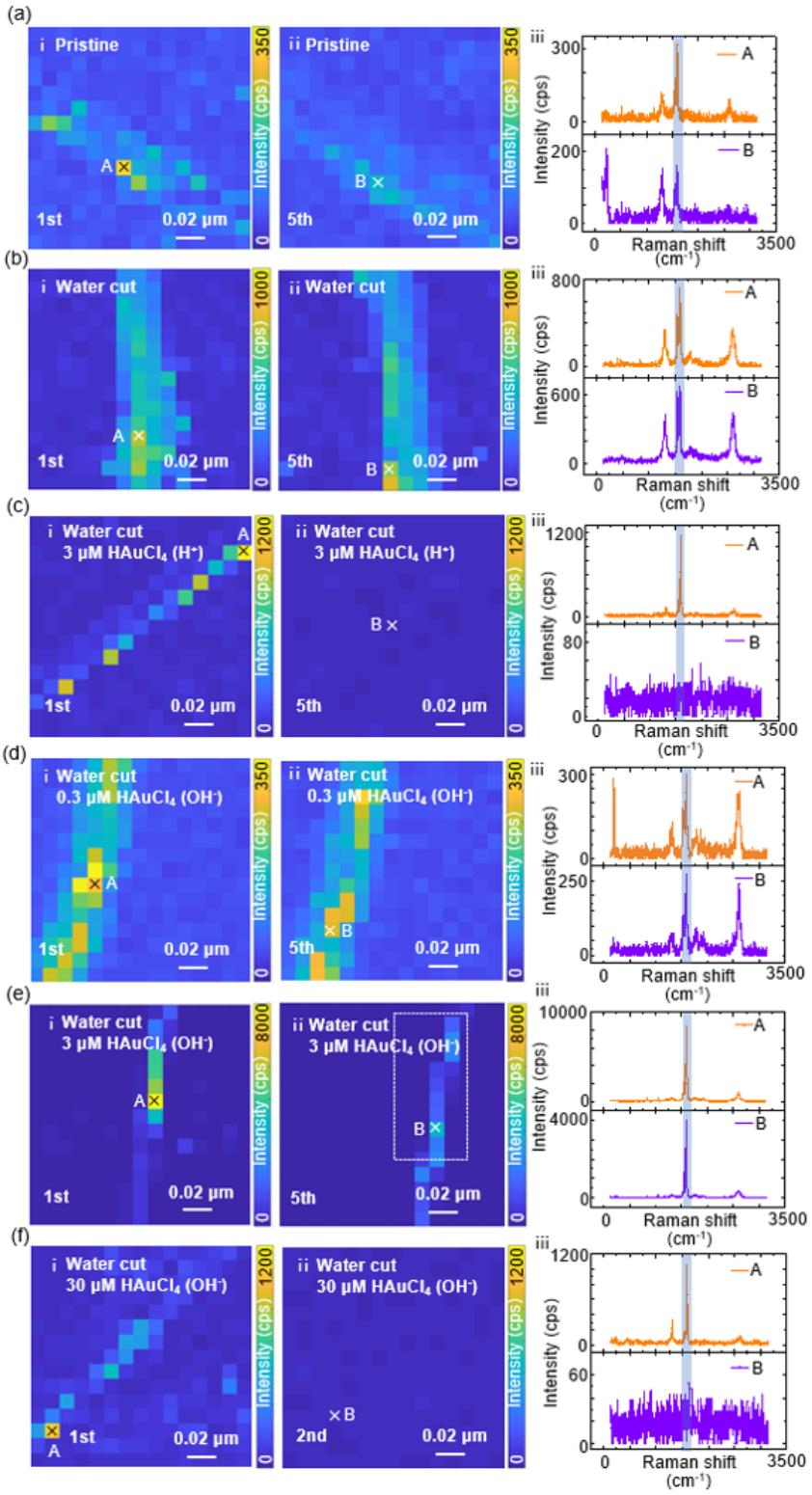

Figure 3-5. Gap-mode TERS on CNTs on Au (111) with different probes: (a) pristine AgNW; (b) water (PVP)-cut AgNW; (c) cut-AgAu-3-H; (d) cut-AgAu-0.3-OH; (e) cut-AgAu-3-OH; (f) cut-AgAu-30-OH. In all subfigures, i refers to the first TERS mapping; ii refers to the 5th (2nd in f) TERS mapping; iii refers to the TERS spectra of pixel A in i and pixel B in ii.

(Acquisition time was 0.2 s, accumulation once, 15×15 pixels (10 nm/pixel), laser power ~1.53 kW/cm^2, and the Raman intensity of G-band (cps) is selected to evaluate the TERS enhancement.)

To quantitatively evaluate the TERS activity, the EF of each probe was calculated using the Raman intensity at G-band on multiple TERS maps (the detailed calculation method is reported in appendix). For each map, 10 pixels showing the CNT Raman spectrum are picked to calculate the averaged EF and its standard deviation. Fig. 3-6 displays the EF as a function of the number of maps, the EFs of the first map of each probe are displayed in Fig. 3-A2.

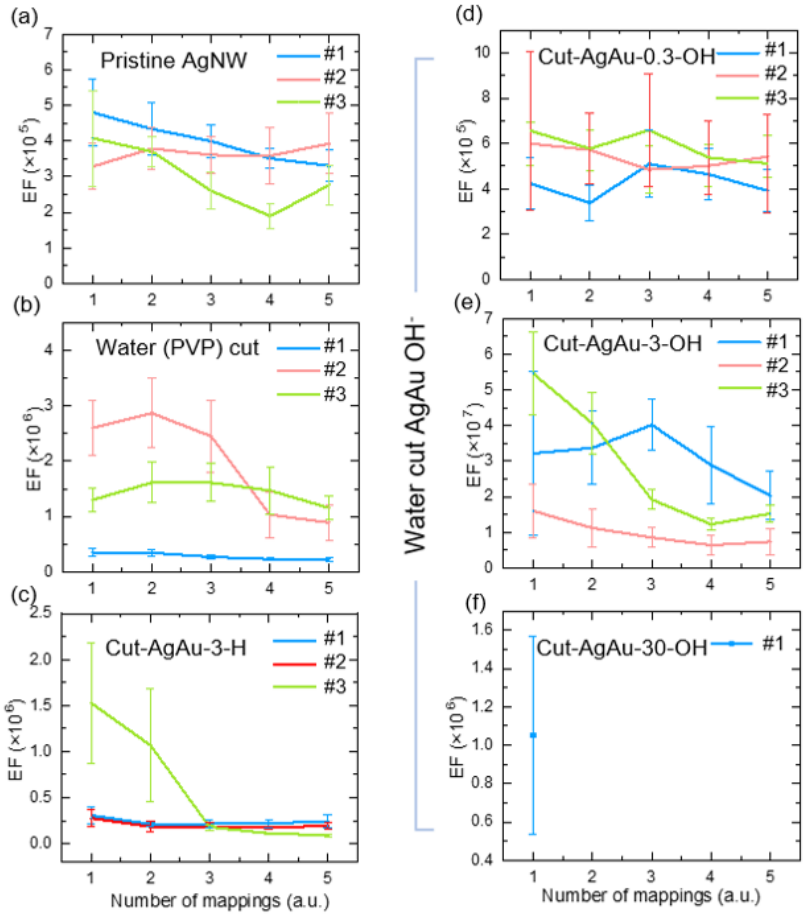

Figure 3-6. EF of the 6 different kinds of TERS probes: (a) pristine AgNW; (b) water (PVP)-cut AgNW; (c) cut-AgAu-3-H; (d) cut-AgAu-0.3-OH; (e) cut-AgAu-3-OH; (f) cut-AgAu-30-OH, as a function of the number of maps. Within each kind, three parallel probes (#1 to #3) were randomly selected from multiple probes and evaluated: probe #1 (blue), #2 (red) and #3 (green), and in (f) only 1 in 3 probe shows TERS activity, while 2 probes in 3 shows no TERS activity.

Pristine AgNWs showed an EF of ~ 10^5 on the first map and allowed for multiple mappings maintaining EFs in the range of 10^5, as previously reported by our group.[10, 20] Differently, the EFs of water (PVP) cut could reach the order of ~10^6 but with higher heterogeneity between probes. The cut-AgAu-0.3-OH probes show better homogeneity than the water (PVP) cut probes but possess lower EFs, which are at the order of ~10^5 while slightly higher than pristine AgNWs. Amongst probe types, the cut-AgAu-3-OH probes show the highest EFs at ~10^7 and could maintain at this level for at least 5 mappings. In terms of EF and durability, the cut-AgAu-3-OH probes obtained with 3 µM of Au^{3+} at pH 10 could be classed as the most performant. The high TERS performance of the Au modified AgNW probes showed here in line with previous reports where AgAu bimetallic nanoparticles and NWs showed increased Raman enhancement than monometallic Ag nanostructures.[20, 27-29]

The reproducibility of all discussed probes was summarized in Tab. 3-A1 and Fig. 3-A3. Except for the cut-AgAu-30-OH probes, which show a low success rate (~33%), other kinds of probes exhibit a relatively high success rate (~67-83%), which demonstrates the efficiency of this probe fabrication method.

By observing the TERS maps in Fig. 3-5, an evidently higher spatial resolution of the cut-AgAu-3-OH could be already noticed. To accurately evaluate this spatial resolution, a more detailed mapping was conducted at the area indicated with the square in Fig. 3-5e (ii), which is shown in Fig. 3-7 with a pixel size of 3.33 nm. The line profile (a-a') was fitted with the Gauss function, on which a resolution of ~5 nm (=FWHM) was estimated. Consequently, with this probe, ones can study the structural information within 10 nm in many frontier fields, which is a significant improvement in TERS technique.

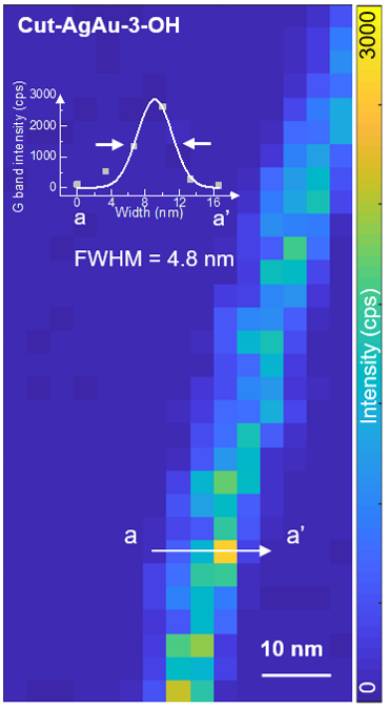

Figure 3-7. High spatial resolution TERS mapping by the cut-AgAu-3-OH probe. (Acquisition time was 0.2 s, accumulation once, 15×30 pixels (3.33 nm/pixel), laser power ~1.53 kW/cm^2)

Non-gap mode TERS

As previously indicated, the EF of the cut-AgAu-3-OH could reach ~10^7 EF under the gap-mode, which is dramatically higher compared to the commonly used TERS probes. To evaluate the performance of this impressive probe under non-gap mode, CNTs on a silicon substrate were chosen as a sample for the evaluation. A successful non-gap TERS map is shown in Fig. 3-8, where i refers to the TERS map at G-band, ii to the AFM topographic image, and iii to the TERS spectra at the position A in i, and iv to the line profile along the white line in the AFM image. We found that, using this probe, the EF under non-gap mode could reach to ~1.3×10^5 and single CNTs dispersed on non-plasmonic silicon substrates were successfully mapped out with c.a. 20 nm spatial resolution. This suggests that the cut-AgAu-3-OH provide an opportunity to achieve non-gap mode TERS activity with a relatively stable successful rate (~ 30 % of the prepared probes), which surpasses the substrate limitation of TERS techniques.

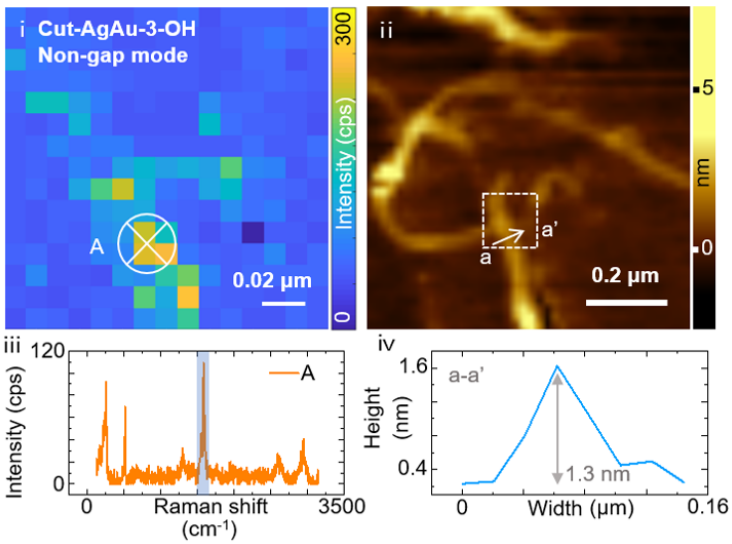

Figure 3-8. Non-gap mode TERS map of CNTs on a silicon substrate by the cut-AgAu-3-OH probe: i refers to the TERS map of the framed area in ii (acquisition time was 0.2 s, accumulation once, 15×15 pixels (10 nm/pixel), laser power ~7.05 kW/cm^2), ii to the AFM topographic image, iii to the point spectrum at the point A (acquisition time: 0.2 s, average: 10 times, laser power: ~7.05 kW/cm^2), and iv refers to the line profile of the CNT along the line a-a' in the topographic image.

3.5 Conclusion

We developed a simple method to control the protruded length of an AgNW-based AFM-TERS probe by employing electro-cut of AgNW at water-air interface. To increase chemical stability, the apex of the cut AgNW was coated with Au thin layers in an alkaline solution of Au^{3+}. Under an appropriated condition, a high spatial resolution (~5 nm) and high EF (~10^7) can be achieved in gap-mode. The Au-modified cut AgNW probes showed up to 100 times higher EF and two times the smaller spatial resolution than pristine AgNW probes. Moreover, one probe can be repeatably used for multiple TERS mapping. Such exclusive EF and spatial resolution pave the way to more accurate TERS-based investigations of samples at the nanoscale. Importantly, thanks to the high EF nature, the probes allow to conduct excellent TERS mapping even in non-gap mode on dielectric substrates, overpassing the substrate limitation of TERS techniques. We believe that the reported Au-modified AgNW TERS probe is promising for high-quality nanoscale characterization in a wide variety of fields, such as quality control of nanostructured semiconductors, detailed investigation of 2D materials, and even biological specimens.

3.6 Appendix

Calculation of EF

The calculation method is shown in equations 3-A1 and 3-A2. C_{TERS} refers to TERS contrast, in which I_{TERS} and $I_{Far\text{-}Field}$ are the Raman intensity enhanced by near field and the intensity of normal far-field Raman. Here, the Raman intensity of G-band is picked as I_{TERS} since it is relatively stable and not affected by defect spots on the CNT, $I_{Far\text{-}Field}$ was measured under high laser power (~143 kW/cm^2) since it is almost impossible to obtain Raman signal with acceptable signal-to-noise ratio under same low laser power as TERS. Then, as the Raman signal is proportional to the laser power, the Raman signal is calculated by proportional compensating power difference. In equation 3-A2, $A_{Far\text{-}Field}$ and $A_{Near\text{-}Field}$ refer to the area of far-field and near-field, respectively. The area of far-field can be easily calculated as the area of laser diffraction-limited focal spot by: diameter = 1.22 λ / NA. However, the area of the near-field is hard to estimate, which is commonly calculated by numerical simulation. Nevertheless, the validity of simulation is limited since multiple assumptions are necessary. Here, the enhancing area is estimated by the TERS resolution, which is reported to be below 15 nm,[10] and in this experiment, 10 nm is regarded as the TERS resolution.

$$C_{TERS} = \frac{\mathrm{I_{TERS}} - \mathrm{I_{Far-Field}}}{\mathrm{I_{Far-Field}}} \qquad 3-A1$$

$$EF = \mathrm{C_{TERS}} \cdot \frac{\mathrm{A_{Far-Field}}}{\mathrm{A_{Near-Field}}} \qquad 3-A2$$

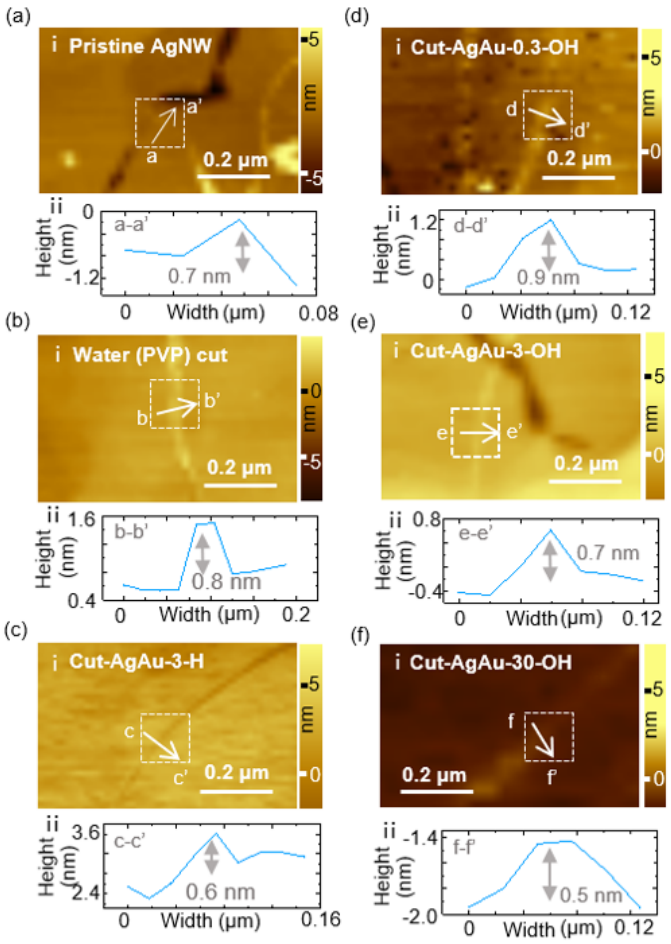

Figure 3-A1. AFM images and line profiles of different probes corresponding to Fig. 3-5: (a) pristine AgNW; (b) water (PVP)-cut AgNW; (c) cut-AgAu-3-H; (d) cut-AgAu-0.3-OH; (e) cut-AgAu-3-OH; (f) cut-AgAu-30-OH. In all subfigures, i refers to the AFM images; ii refers to the line profiles along the white lines in the AFM images.

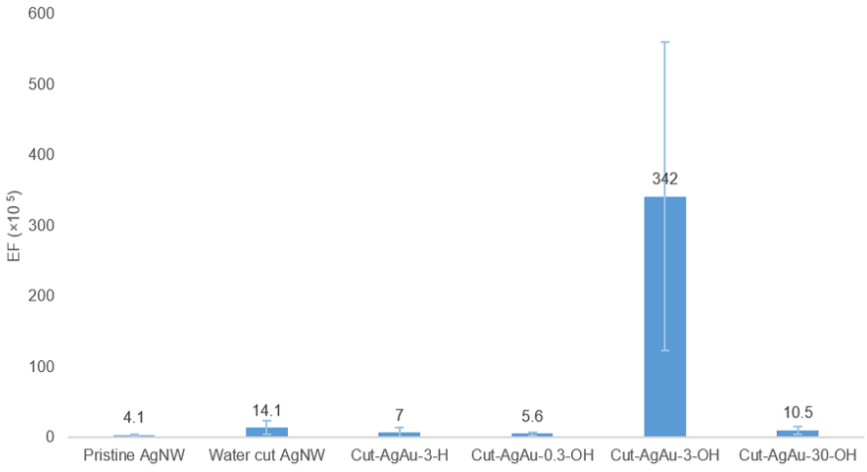

Figure 3-A2. EF of the first mappings of 6 kinds of TERS probes corresponding to Fig. 3-6.

Table 3-A1. TERS reproducibility of different kinds of TERS probes.

	TERS activity	No activity
Pristine AgNW	4	1
Water (PVP) cut AgNW	4	2
Cut-AgAu-3-H	4	2
Cut-AgAu-0.3-OH	5	1
Cut-AgAu-3-OH	4	2
Cut-AgAu-30-OH	2	4

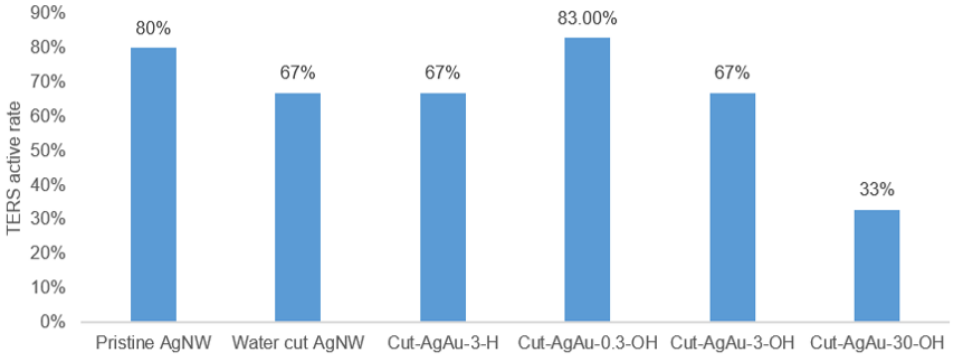

Figure 3-A3. TERS reproducibility of 6 kinds of probes

3.7 References

(1) Stöckle, R. M.; Suh, Y. D.; Deckert, V.; Zenobi, R. Nanoscale chemical analysis by tip-enhanced Raman spectroscopy. *Chemical Physics Letters* **2000**, *318* (1), 131-136. DOI: https://doi.org/10.1016/S0009-2614(99)01451-7.

(2) Pienpinijtham, P.; Kitahama, Y.; Ozaki, Y. Progress of tip-enhanced Raman scattering for the last two decades and its challenges in very recent years. *Nanoscale* **2022**, *14* (14), 5265-5288, 10.1039/D2NR00274D. DOI: 10.1039/D2NR00274D.

(3) Kazemi-Zanjani, N.; Kergrene, E.; Liu, L.; Sham, T.-K.; Lagugné-Labarthet, F. Tip-Enhanced Raman Imaging and Nano Spectroscopy of Etched Silicon Nanowires. *Sensors* **2013**, *13* (10). DOI: 10.3390/s131012744.

(4) Park, K.-D.; Khatib, O.; Kravtsov, V.; Clark, G.; Xu, X.; Raschke, M. B. Hybrid Tip-Enhanced Nanospectroscopy and Nanoimaging of Monolayer WSe2 with Local Strain Control. *Nano Letters* **2016**, *16* (4), 2621-2627. DOI: 10.1021/acs.nanolett.6b00238.

(5) Kumar, N.; Stephanidis, B.; Zenobi, R.; Wain, A. J.; Roy, D. Nanoscale mapping of catalytic activity using tip-enhanced Raman spectroscopy. *Nanoscale* **2015**, *7* (16), 7133-7137, 10.1039/C4NR07441F. DOI: 10.1039/C4NR07441F.

(6) Gucciardi, P. G.; Valmalette, J.-C. Different longitudinal optical—transverse optical mode amplification in tip enhanced Raman spectroscopy of GaAs(001). *Applied Physics Letters* **2010**, *97* (26), 263104. DOI: 10.1063/1.3532841 (acccessed 2021/06/21).

(7) VandenAkker, C. C.; Schleeger, M.; Bruinen, A. L.; Deckert-Gaudig, T.; Velikov, K. P.; Heeren, R. M. A.; Deckert, V.; Bonn, M.; Koenderink, G. H. Multimodal Spectroscopic Study of Amyloid Fibril Polymorphism. *The Journal of Physical Chemistry B* **2016**, *120* (34), 8809-8817. DOI: 10.1021/acs.jpcb.6b05339.

(8) Olschewski, K.; Kämmer, E.; Stöckel, S.; Bocklitz, T.; Deckert-Gaudig, T.; Zell, R.; Cialla-May, D.; Weber, K.; Deckert, V.; Popp, J. A manual and an automatic TERS based virus discrimination. *Nanoscale* **2015**, *7* (10), 4545-4552, 10.1039/C4NR07033J. DOI: 10.1039/C4NR07033J.

(9) Wang, D.; He, P.; Wang, Z.; Li, G.; Majed, N.; Gu, A. Z. Advances in single cell Raman spectroscopy technologies for biological and environmental applications. *Current Opinion in Biotechnology* **2020**, *64*, 218-229. DOI: https://doi.org/10.1016/j.copbio.2020.06.011.

(10) Walke, P.; Fujita, Y.; Peeters, W.; Toyouchi, S.; Frederickx, W.; De Feyter, S.; Uji-i, H. Silver nanowires for highly reproducible cantilever based AFM-TERS microscopy: towards a universal TERS probe. *Nanoscale* **2018**, *10* (16), 7556-7565, 10.1039/C8NR02225A. DOI: 10.1039/C8NR02225A.

(11) Walke, P.; Toyouchi, S.; Wolf, M.; Peeters, W.; Prabhu, S. R.; Inose, T.; De Feyter, S.; Fujita, Y.; Uji-i, H. Facilitating Tip-Enhanced Raman Scattering on Dielectric Substrates via Electrical Cutting of Silver Nanowire Probes. *The Journal of Physical Chemistry Letters* **2018**, *9* (24), 7117-7122. DOI: 10.1021/acs.jpclett.8b03189.

(12) Fujita, Y.; Walke, P.; De Feyter, S.; Uji-i, H. Tip-enhanced Raman scattering microscopy: Recent advance in tip production. *Japanese Journal of Applied Physics* **2016**, *55* (8S1), 08NA02. DOI: 10.7567/jjap.55.08na02.

(13) Zhang, R.; Zhang, Y.; Dong, Z. C.; Jiang, S.; Zhang, C.; Chen, L. G.; Zhang, L.; Liao, Y.; Aizpurua, J.; Luo, Y.; et al. Chemical mapping of a single molecule by plasmon-enhanced Raman scattering. *Nature* **2013**, *498* (7452), 82-86. DOI: 10.1038/nature12151.

(14) Asghari-Khiavi, M.; Wood, B. R.; Hojati-Talemi, P.; Downes, A.; McNaughton, D.; Mechler, A. Exploring the origin of tip-enhanced Raman scattering; preparation of efficient TERS probes with high yield. *Journal of Raman Spectroscopy* **2012**, *43* (2), 173-180, https://doi.org/10.1002/jrs.3021. DOI: https://doi.org/10.1002/jrs.3021 (acccessed 2021/06/23).

(15) Taguchi, A.; Hayazawa, N.; Saito, Y.; Ishitobi, H.; Tarun, A.; Kawata, S. Controlling the plasmon resonance wavelength in metal-coated probe using refractive index modification. *Opt. Express* **2009**, *17* (8), 6509-6518. DOI: 10.1364/OE.17.006509.

(16) Shi, X.; Coca-López, N.; Janik, J.; Hartschuh, A. Advances in Tip-Enhanced Near-Field Raman Microscopy Using Nanoantennas. *Chemical Reviews* **2017**, *117* (7), 4945-4960. DOI: 10.1021/acs.chemrev.6b00640.

(17) Schmid, T.; Opilik, L.; Blum, C.; Zenobi, R. Nanoscale Chemical Imaging Using Tip-Enhanced Raman Spectroscopy: A Critical Review. *Angewandte Chemie International Edition* **2013**, *52* (23), 5940-5954, https://doi.org/10.1002/anie.201203849. DOI: https://doi.org/10.1002/anie.201203849 (acccessed 2021/06/23).

(18) Rycenga, M.; Cobley, C. M.; Zeng, J.; Li, W.; Moran, C. H.; Zhang, Q.; Qin, D.; Xia, Y. Controlling the Synthesis and Assembly of Silver Nanostructures for Plasmonic Applications. *Chemical Reviews* **2011**, *111* (6), 3669-3712. DOI: 10.1021/cr100275d.

(19) Korte, K. E.; Skrabalak, S. E.; Xia, Y. Rapid synthesis of silver nanowires through a CuCl- or CuCl2-mediated polyol process. *Journal of Materials Chemistry* **2008**, *18* (4), 437-441, 10.1039/B714072J. DOI: 10.1039/B714072J.

(20) Wen, H.; Inose, T.; Hirai, K.; Akashi, T.; Sugioka, S.; Li, J.; Peeters, W.; Fron, E.; Fortuni, B.; Nakata, Y.; et al. Gold-coated silver nanowires for long lifetime AFM-TERS probes. *Nanoscale* **2022**, *14* (14), 5439-5446, 10.1039/D1NR07833J. DOI: 10.1039/D1NR07833J.

(21) Sigma-Aldrich. *Carbon nanotube, single-walled*. 2017. https://www.sigmaaldrich.com/JP/en/product/aldrich/704121 (accessed 2022 31st October).

(22) Schulze, H. G.; Foist, R. B.; Okuda, K.; Ivanov, A.; Turner, R. F. B. A Small-Window Moving Average-Based Fully Automated Baseline Estimation Method for Raman Spectra. *Applied Spectroscopy* **2012**, *66* (7), 757-764. DOI: 10.1366/11-06550 (acccessed 2021/07/04).

(23) Salari, A.; Navi, M.; Lijnse, T.; Dalton, C. AC Electrothermal Effect in Microfluidics: A Review. *Micromachines* **2019**, *10* (11). DOI: 10.3390/mi10110762.

(24) Na, Y. H.; Aida, K.; Sakai, R.; Kakuchi, T.; Orihara, H. Response of shear stress to ac electric fields under steady shear flow in a droplet-dispersed phase. *Physical Review E* **2009**, *80* (6), 061803. DOI: 10.1103/PhysRevE.80.061803.

(25) Yang, Y.; Liu, J.; Fu, Z.-W.; Qin, D. Galvanic Replacement-Free Deposition of Au on Ag for Core–Shell Nanocubes with Enhanced Chemical Stability and SERS Activity. *Journal of the American Chemical Society* **2014**, *136* (23), 8153-8156. DOI: 10.1021/ja502472x.

(26) Lee, H.; Hong, S.; Lee, J.; Suh, Y. D.; Kwon, J.; Moon, H.; Kim, H.; Yeo, J.; Ko, S. H. Highly Stretchable and Transparent Supercapacitor by Ag–Au Core–Shell Nanowire Network with High Electrochemical Stability. *ACS Applied Materials & Interfaces* **2016**, *8* (24), 15449-15458. DOI: 10.1021/acsami.6b04364.

(27) Cui, Y.; Ren, B.; Yao, J.-L.; Gu, R.-A.; Tian, Z.-Q. Synthesis of AgcoreAushell Bimetallic Nanoparticles for Immunoassay Based on Surface-Enhanced Raman Spectroscopy. *The Journal of Physical Chemistry B* **2006**, *110* (9), 4002-4006. DOI: 10.1021/jp056203x.

(28) Fan, M.; Lai, F.-J.; Chou, H.-L.; Lu, W.-T.; Hwang, B.-J.; Brolo, A. G. Surface-enhanced Raman scattering (SERS) from Au:Ag bimetallic nanoparticles: the effect of the molecular probe. *Chemical Science* **2013**, *4* (1), 509-515, 10.1039/C2SC21191B. DOI: 10.1039/C2SC21191B.

(29) Ling, L.; Xu, M.-M.; Gu, R.-A.; Yao, J.-L. Preparation of $Ag_{core}Au_{shell}$ Nanowires and Their Surface Enhanced Raman Spectroscopic Studies. *Acta Chimica Sinica* **2007**, *65* (9), 779-784.

Summary and perspective

In summary, in this thesis, based on the previously developed AgNW-based AFM-TERS probe, we focus on further improving the probe fabrication method to solve the short lifetime and the protruded length control issues and further enhance the enhancement.

Firstly, to solve the short-lifetime issue and improve the TERS performance, a simple Au coating method is proposed. Different [Au]/[Ag] molar ratios were investigated for the Au-coating. The TERS performance was evaluated regarding the change in EF and signal-to-noise ratio through multiple mappings and the storage lifetime in the air. The Au-coated AgNWs exhibited higher EF than pristine AgNW and galvanic-replaced AgNW with no remarkable difference between the two molar ratios tested, while for longer scanning time and multiple mappings, the probes obtained with low Au concentration showed much longer-term stability with keeping high EF. Furthermore, the Au-coated AgNW probes were found to possess a longer storage lifetime in air, allowing for long and multiple TERS mappings with one single probe.

Secondly, to achieve wide controllability of the protruded AgNW length and further improve the TERS performance, a simple water-air interface electro-cutting method is proposed, which achieves the protruded length control. Moreover, by combining the cutting method with the succedent Au coating on the AgNW surface, probes with high durability, impressive EF, and excellent spatial resolution were fabricated. The TERS performance was evaluated in terms of change in EF through multiple mappings and spatial resolution. The water-cut Au-coated AgNWs, with appropriated Au concentration and pH, achieved up to 100 times higher EF and two times the smaller spatial resolution than pristine AgNW. Thanks to this excellent EF, the water-cut Au-coated AgNW probes were found to possess high TERS activity even in non-gap mode, allowing for broader applications.

This work solved the durability and length control issues of the AgNW-based AFM-TERS probe and achieved high Raman enhancement even can conduct non-gap mode TERS measurement. After these technical improvements, the AgNW-based TERS probe becomes more mature, which provides academia and the industrial world another powerful option in TERS-related fields.

Publications

Publications related to this dissertation:

(1) **Wen, H.**; Inose, T.; Hirai, K.; Akashi, T.; Sugioka, S.; Li, J.; Peeters, W.; Fron, E.; Fortuni, B.; Nakata, Y.; Rocha, S.; Toyouchi, S.; Fujita, Y.; Ujii, H. Gold-coated silver nanowires for long lifetime AFM-TERS probes. *Nanoscale* **2022**, *14* (14), 5439-5446. DOI: 10.1039/D1NR07833J.

(2) **Wen, H.**; Li, J.; Zhang, Q.; Inose, T.; Peeters, W.; Fortuni, B.; Asakawa, H.; Masuhara, A.; Hirai, K.; Toyouchi, S.; Fujita, Y.; Uji-i, H. Length Controllable Gold-coated Silver Nanowire Probes for High AFM-TERS activity. *Nano Letters*, in press. DOI: 10.1021/acs.nanolett.2c03985.

Other publication:

(3) Zhang, Q.; **Wen, H.**; Watanabe, K.; Kotani, I.; Ricci, M.; Fortuni, B.; Dao, A. T. N.; Masuhara, A.; Hirai, K.; Kasai, H.; et al. Low-Cytotoxic Gold-Coated Silver Nanoflowers for Intracellular pH Sensing. *ACS Applied Nano Materials* **2020**, *3* (8), 7643-7650. DOI: 10.1021/acsanm.0c01278.

(4) Zhang, Q.; Inose, T.; Ricci, M.; Li, J.; Tian, Y.; **Wen, H.**; Toyouchi, S.; Fron, E.; Ngoc Dao, A. T.; Kasai, H.; et al. Gold-Photodeposited Silver Nanowire Endoscopy for Cytosolic and Nuclear pH Sensing. *ACS Applied Nano Materials* **2021**, *4* (9), 9886-9894. DOI: 10.1021/acsanm.1c02363.

Conferences

(1) **Wen, H.**; Inose, T.; Ogawa, T.; Fortuni, B.; Rocha, S.; Hirai, K.; Uji-i, H. Particle tracking of individual nanoparticles using chemical fingerprint. *The 20th RIES-Hokudai International Symposium*, Hokkaido university, Dec 2-3, 2019, poster.

(2) **Wen, H.**; Inose, T.; Ogawa, T.; Fortuni, B.; Rocha, S.; Hirai, K.; Uji-i, H. Particle tracking of individual nanoparticles using chemical fingerprint. *The 20th RIES-NCTU International Symposium*, Hokkaido university, Dec 3-4, 2019, poster.

(3) **Wen, H.**; Inose, T.; Sugioka, S.; Li, J.; Hirai, K.; Uji-i, H. Nanoscale characterisation of carbon nanomaterials using tip-enhanced Raman spectroscopy. *The 21st RIES-Hokudai International Symposium*, Online, Dec 10-11, 2020, poster.

(4) **Wen, H.**; Sugioka, S.; Kanda, N.; Li, J.; Inose, T.; Miyata, Y.; Nakanishi, Y.; Hirai, K.; Fujita, Y.; Uji-i, H. Nanoscale characterisation of carbon nanomaterials using tip-enhanced Raman spectroscopy. *The 68th JSAP Spring Meeting*, Online, Mar 16-19, 2021, Oral.

(5) **Wen, H.**; Inose, T.; Hirai, K.; Akashi, T.; Sugioka, S.; Li, J.; Peeters, W.; Fron, E.; Fortuni, B.; Rocha, S.; Toyouchi, S.; Fujita, Y.; Uji-i, H. Gold coated silver nanowire based high performance AFM-TERS microscopy. *The 4th International Workshop on Symbiosis of Biology and Nanodevices*, Online, Nov 4-5, 2021, poster. **Got Poster Award.**